DECORRELATION TIME ANALYSIS USING DYNAMIC LIGHT SCATTERING

WITH OPTICAL COHERENCE TOMOGRAPHY IN AN IN VIVO MOUSE

TUMOUR MODEL

By

Timothy Wan Hei Luk, B.A.Sc. in Engineering Science

University of Toronto

Toronto, Ontario, Canada, 2009

A thesis presented to Ryerson University

in partial fulfillment of the

requirements for the degree of

Master of Science

in the Program of

Biomedical Physics

Toronto, Ontario, Canada, 2013

Author's Declaration

I hereby declare that I am the sole author of this thesis. This is a true copy of the thesis, including any required final revisions, as accepted by my examiners.

I authorize Ryerson University to lend this thesis to other institutions or individuals for the purpose of scholarly research.

I further authorize Ryerson University to reproduce this thesis by photocopying or by other means, in total or in part, at the request of other institutions or individuals for the purpose of scholarly research.

I understand that my thesis may be made electronically available to the public.

Abstract

Decorrelation Time Analysis Using Dynamic Light Scattering with Optical Coherence

Tomography in an *in vivo* Mouse Tumour Model

Timothy Wan Hei Luk, Master of Science, 2013

Department of Physics, Program of Biomedical Physics

Ryerson University

Optical coherence tomography (OCT) is an imaging modality that uses near infrared light interferometry for non-invasive, near-histological resolution imaging at the micron level. Concepts from dynamic light scattering (DLS) can be adapted to OCT to detect and measure the motions in the target tissue. Tissue dynamics can be observed by measuring the speckle decorrelation time (DT) of the tissue. DT analysis was performed in a preclinical study to demonstrate the repeatability and feasibility of using DLS-OCT to observe mouse tumours undergoing cisplatin treatment over a 48-hour period. Differences in the average DT data were observed for control and cisplatin-injected mice. Image segmentation based on DT values was also performed to subtract the DT contributions of pixels at blood vessel locations, resulting in the improvement of average DT calculations of the tumour tissue. The results presented are a preliminary step to analyzing and monitoring tumour growth and treatment response *in vivo*.

Acknowledgements

Dedication

This research work is dedicated to all my friends and family who have supported me throughout these years.

Table of Contents

List of Tables

List of Figures

Chapter 1: Introduction

Medical imaging is a field of study that encompasses many processes and techniques that are used for disease diagnosis and analysis for clinical and research purposes. In the clinic, medical imaging is vital for the management of patient diseases. In the research field, medical imaging is essential in the study of disease development and monitoring the disease to aid the clinician's work. Minimally invasive imaging techniques have been developed and standardized as three-dimensional imaging modalities in diagnostic medicine. Such imaging techniques include magnetic resonance imaging (MRI), ultrasound (US), X-ray computed tomography (CT), positron emission tomography (PET), single-photon emission computed tomography (SPECT), and other radiography, nuclear medicine, and tomography techniques. A common limitation to these techniques is the low spatial resolution, which typically is in the millimetre range. Another imaging modality (confocal microscopy, CM) can provide micron image resolution, but lacks the penetration depth (less than 1 millimetre) of these medical imaging techniques (millimetres to centimetres) [1].
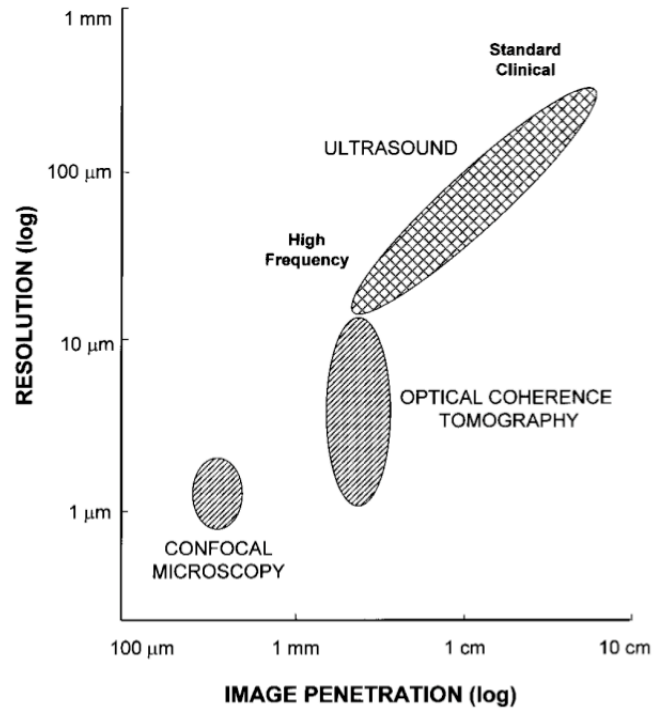
Figure 1-1: Medical imaging techniques (US, CM, and OCT) and their resolution and penetration depths [2].

Optical coherence tomography (OCT) is an imaging technology developed in the 1990s [2]. Using near infrared light interferometry, OCT offers near-histological resolution (ranging from submicron to a few microns) and is a non-invasive (or minimally invasive, depending on the application) imaging modality. Moreover, it provides images that cannot be obtained by other means due to its high resolution imaging while maintaining a depth of field. Figure 1-1 compares the resolution and penetration depths of confocal microscopy, ultrasound, and optical coherence tomography.
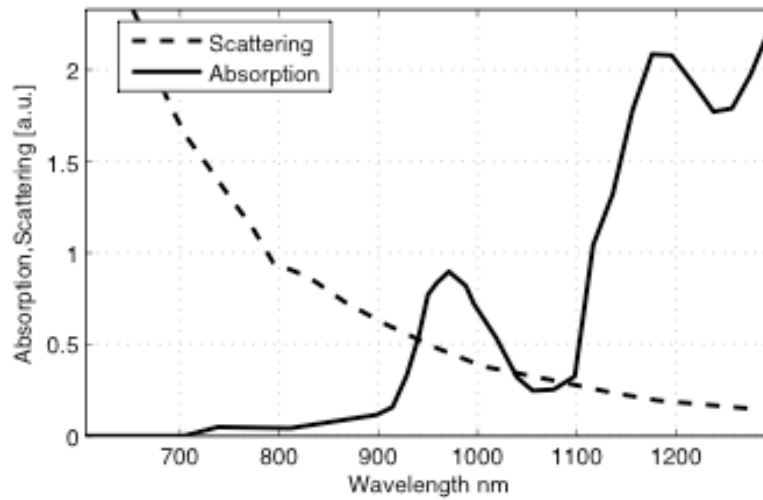
Figure 1-2: Scattering and absorption peaks of water [3].

OCT utilizes near infrared wavelengths of 1310 nm or 800 nm for interferometry purposes due to its increased depth penetration at longer wavelengths. OCT light sources that are centred at 1060 nm wavelengths have also been developed due to the optical properties of water as biological tissues contain large amounts of water. Therefore, the absorption and scattering of light in water is key to understanding and optimizing OCT imaging. The absorption and scattering of broadband light in water is depicted in Figure 1-2. The resulting imaging wavelength chosen must have a maximized scattering peak, a minimized absorption peak, and maximized depth penetration [3-4].

OCT has had a major impact on preclinical and clinical research, transforming ophthalmology, intravascular coronary imaging, and have an impact in other areas of medicine including neurosurgery, oncology, radiology, bronchoscopy, gastrointestinal endoscopy, laparoscopic surgery, urology, gynecology, plastic surgery and dermatology. In ophthalmology, OCT has been used to study retinal pathology [5]. Catheters and probes have been developed for imaging the microvasculature and microstructures [6-8].

Intravascular OCT has also been used in studies of the gastrointestinal tract and *in vivo* vessel imaging [9-10].

There are also applications of OCT (Doppler OCT, speckle variance, phase variance, etc.) that are specifically geared for visualizing microvasculature and other targets to provide additional clinical information. OCT is a powerful imaging technique that can be used for microstructural studies with many clinical benefits. The continuation of OCT research will only develop and enhance the clinical usage of OCT instrumentation in medical imaging.

The goal of this thesis is to develop and implement a method for the analysis of *in vivo* mouse tumour speckle decorrelation time maps obtained from an OCT adaptation of dynamic light scattering (DLS). It was previously shown that the cellular and intracellular motion of cells undergoing apoptosis (a known form of cell death) could be monitored using dynamic light scattering with OCT [11]. After the *in vitro* studies were completed, speckle decorrelation time (DT) maps were generated from the DLS-OCT images *in vivo* [12]. In the preliminary study involving three mice, the authors measured variations in the speckle DT maps between tumour regions and the surrounding non-tumour tissue. In addition, changes in the tissue DT were also observed, in the same tumour regions, as a function of treatment time for mice treated with a chemotherapy drug. The study, however, had several limitations: apart from the small number of animals used, the DT maps had regions of interest (ROI) that included contributions to the DT maps from blood vessels, not just from regions of tumour cells. As the DT maps that enclosed only cells responding to the chemotherapeutic treatment was of interest, a method to confine the analysis to such regions was needed. Therefore, the motivation of this thesis was to:

4

a) establish the repeatability of the previous results with a larger *in vivo* dataset, and b) introduce a segmentation technique to remove any DT contributions from blood flow. Extensions to this thesis include protocol refinements for future *in vivo* experiments for utilizing DT measurements of intracellular motion as an endogenous contrast method for tumour-related studies.

1.1 Thesis Objectives

The first objective of this thesis is to implement a speckle decorrelation time analysis algorithm for an n=10 mouse tumour model study, building upon the previous n=3 feasibility test performed by Farhat et al. [12]. This is done to demonstrate the repeatability of the protocol and to obtain better statistical significance for the comparisons of the DT maps for mice undergoing cisplatin treatment.

The second objective of this thesis is to confine the DT analysis to regions *in vivo* that do not include bulk flow due to blood motions. To achieve this, the microvasculature needs to be segmented and removed from the regions used in the analysis. The previous study contained DT results that took into account the DT contributions from blood vessel locations, which may dominate the OCT DT signals. A method needs to be developed to threshold DT data so that only areas without the bulk flow of blood are used in the DT analysis of the tissues.

1.2 Thesis Hypothesis

Speckle decorrelation time (DT) analysis of mouse tumours can be performed reproducibly *in vivo* and the application of thresholds to segment out DT contributions from blood vessels will allow a more reliable method of detecting cell death *in vivo*.

Chapter 2: Background

2.1 Dynamic Light Scattering

The heterogeneity and dynamicity of cellular tissue are utilized in light scattering tissue imaging. The organelles of living cells provide the dynamic character that can be probed by light scattering techniques. It is thought that the active functions of the cytoskeleton [13-14] and molecular motors [15] that drive the transport systems in the cytosol [16] produce fluctuations in the scattered light detected.

Dynamic light scattering (DLS) is the use of light scattering techniques for detecting and measuring the dynamic character of a target. DLS in tissues can be performed as quasi-elastic light scattering (QELS) when predominantly singly-scattered light is used, whereas diffusing-wave spectroscopy (DWS) or diffusing correlation spectroscopy (DCS) is used for light that is multiply scattered [13-21]. Previous QELS research includes the study of dynamics in the nucleus [17], cytosol [18], and membrane fluctuations [19]. Previous DWS and DCS research includes the study of actin filament networks [20] and imaging dynamic heterogeneities [21]. Speckle contrast of blood flow has also been studied using DLS techniques. This thesis utilizes some of these concepts to observe the tissue dynamics by measuring speckle decorrelation time of the tissue.

2.1.1 Principle

DLS involves the analysis of light intensity fluctuations of the sample refractive index ($\delta n(\mathbf{r}, t)$) recorded from the sample scatters [17]. The sample refractive index is dynamic due to the changing density, concentration, and composition of the tissue light

scattering structures [22]. The scattered light is proportional to the spatial Fourier transform of the sample refractive index: $\delta\hat{n}(\mathbf{q}, t)$. In this equation, $\mathbf{q}$ is the scattering wave vector that defines the characteristic length (l) on which the fluctuations of the refractive index take place ($l = 2\pi/q$; q being the modulus of $\mathbf{q}$). For elastic scattering, the photon energy is conserved and $q = (4\pi n/\lambda) \sin(\theta/2)$, where n = sample refractive index; λ = wavelength; and θ = scattering angle (between the incoming direction and the scattering direction). The fluctuations of the scattered light (related to the sample refractive index) is measured and analyzed to obtain the sample dynamics of the tissue.

2.2 Optical Coherence Tomography

Optical coherence tomography (OCT) is an imaging modality that utilizes photonic devices for near-histological resolution imaging. OCT implements near infrared light interferometry to detect backscattered waves, and have been applied clinically for non-invasive or minimally invasive imaging of tissues. OCT is most often compared to ultrasound (US) due to the analogous concept of sending incident signals and detecting the backscattered response. In US, a sound wave is propagated from a transducer and interrogates the tissue sample. The transducer records the backreflected signals from the sample, and the resulting image is formed. In OCT, the concept is similarly utilized, except light waves are used instead of sound waves, and the respective system components are suited for light imaging. Direct contact between the wave source and the imaged sample is also unnecessary in OCT.

OCT is known for its excellent spatial resolution due to the wavelength of light in the infrared range (~1300 nm), compared to US wavelengths (in the millimetre range for

ultrasound frequencies between 1-5 MHz). The drawback for OCT is the limited penetration depth of 1-3 mm, which differs from US penetration of greater than 10 mm, depending on the ultrasound frequencies used.
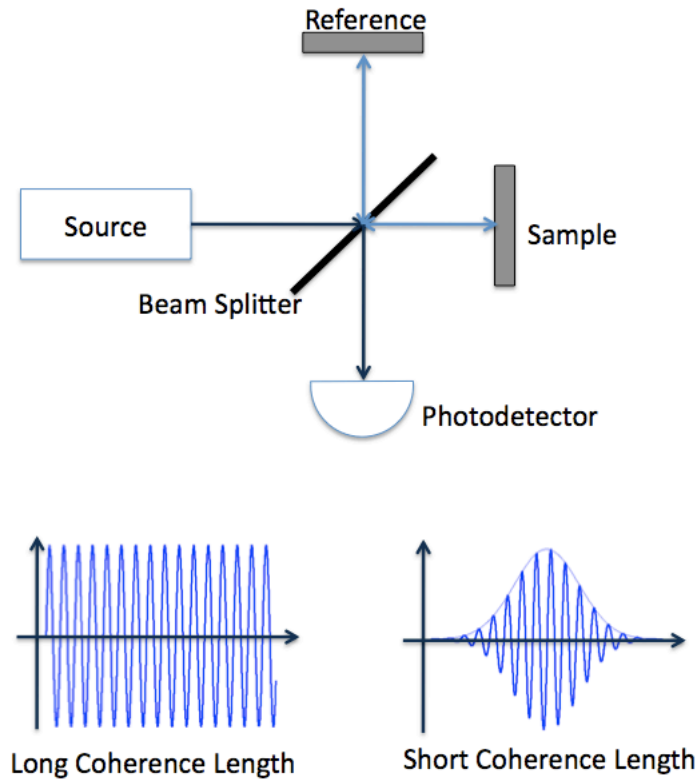
Figure 2-1: (Top) Michelson interferometer; (Bottom) Depiction of long and short coherence lengths [2].

2.2.1 Interferometry

Because OCT uses light that travels at the speed of $\sim 3 \times 10^8$ m/s, existing electronic equipment are not suitable for formulating the resulting image from the time delay of the backscattered light. OCT uses interferometry techniques to gate the data acquisition to produce depth resolved reflectivity profiles of the imaging target.

Figure 2-1 depicts a Michelson interferometer setup, a common configuration for optical interferometry. The light source emits the light towards the beam splitter and is

represented by $E_t(t) = E_i cos(\omega t - kz)$. In this representation, E_t is the electric field at the

position z at time t, k is the wave number given by $2\pi/\lambda$, where λ is the wavelength and ω

is the angular frequency. A beam splitter then divides this beam of light and directs the

two beams to the reference mirror and sample, respectively. These two paths are denoted

by $E_r(t)$ and $E_s(t)$ to represent the reference path and sample path, respectively, where

$E_t(t) = E_r(t) + E_s(t)$. After the two beams reflect off of the reference mirror and sample,

they recombine at the beam splitter. The interferometer output observed at the

photodetector is $\sim E_r(t) + E_s(t)$. The intensity of the output beam is measured by this

detector, and is also proportional to the square of the electric field. The intensity at the

detector is:

$$I_0(t) \sim \frac{1}{4}|E_r|^2 + \frac{1}{4}|E_s|^2 + \frac{1}{2}E_r E_s \cos\left(2\frac{2\pi}{\lambda}\Delta l\right) \qquad\qquad \textbf{Eq.2-1}$$

where Δl is the path difference between the reference arm length and the sample arm

length (l_r and l_s respectively).

It can be seen from Eq.2-1 that if the path difference Δl varies, the output intensity

$I_o(t)$ will vary. This is depicted in the lower two graphs in Figure 2-1, comparing long and

short coherence lengths of the light source. A long coherence length refers to a

monochromatic light source; a light source with a short coherence length is broadband.

The coherence length is inversely proportional to the bandwidth, and thus, for low

coherence light sources, interference can only be observed when the path difference

between the reference and sample lengths is less than the coherence length [23].
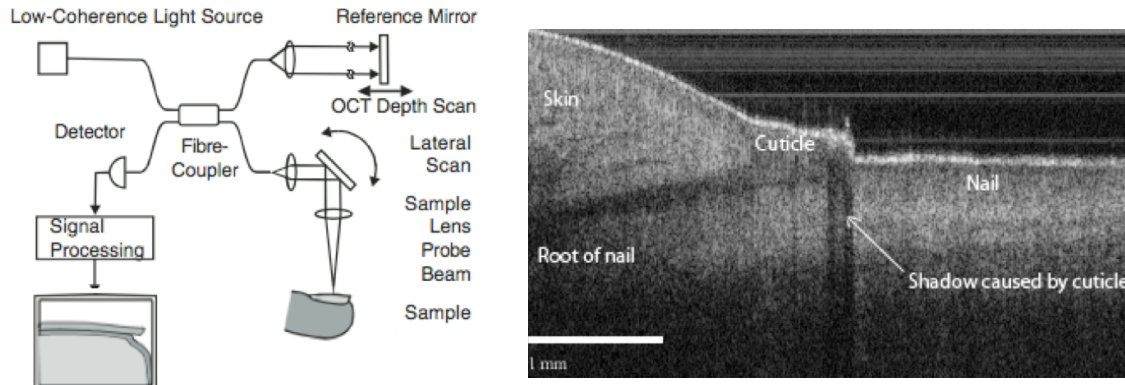
Figure 2-2: (Left) Time-domain OCT (TD-OCT) setup [24]; (Right) OCT image of a fingernail [25].

Figure 2-2 shows the Michelson interferometer as part of a time-domain OCT (TD-OCT) system. The differences here include a fibre coupler in place of the free space beam splitter, a translatable reference mirror for depth adjusted scanning, and additional scanning mirror and focusing lens for raster scanning of the sample. Other OCT enhancements for current OCT system setups will be described later in this chapter.

2.2.2 Resolution

The resolution of an imaging system refers to its capabilities for resolving the details of a target. The resolution specifications are vital to the quality of the image. For OCT imaging, the axial and transverse (lateral) resolutions are independent of each other, which differ from confocal microscopy.

The transverse (lateral) resolution of an OCT system is dependent on the imaging optics that forms the sample arm. For example, the focusing lens of the sample arm will have a specific focal length that affects the transverse resolution of the system. Also, the

beam spot size and wavelength used affects the overall minimum spot size (transverse resolution). Eq.2-2 depicts the equation to calculate this minimum spot size:

$$\Delta x = \frac{4\lambda}{\pi}\left(\frac{f}{d}\right)$$ **Eq.2-2**

where λ and d are the wavelength and spot size of the incident beam, respectively, and f is the lens focal length. Note that the ratio (f/d) is also referred to as the numerical aperture (NA) of the optical system. Eq.2-2 shows that in order to obtain high transverse resolution, a high NA is required by focusing the incident beam to a small spot size. This, however, will reduce the depth of focus (b), which is proportional to the transverse resolution Δx [2]. Eq.2-3 describes the relation between the depth of focus and the transverse resolution. Figure 2-3 depicts the difference between a low NA and high NA setup, demonstrating the trade-off for transverse resolution and depth of focus. The depth of focus is given by:

$$b = \frac{\pi \Delta x^2}{2\lambda}$$ **Eq.2-3**
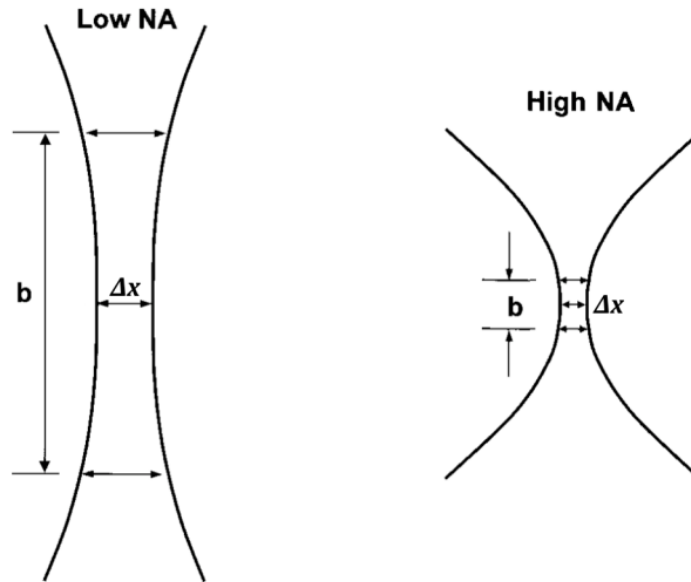
Figure 2-3: The difference between using a low NA and high NA lens, due to the trade-off between the depth of focus (b) and the transverse resolution (Δx) [2].

Therefore, careful selection of the imaging optics is important to obtain the desired depth of focus and transverse resolution. The focusing lens comes in varying NAs that should be chosen based on the intended imaging target. Typically for microvasculature imaging, a lens with higher NA is desired for better transverse resolution when imaging target vessels in the micron range.

The coherence length of the OCT light source used determines the axial resolution of the imaging system. Because there is no reliance on the sample arm focusing optics, the axial resolution is independent of the transverse resolution. The coherence length (Δz) is shown in Eq.2-4.

$$\Delta z = 2 \ln(2) \frac{\lambda_c^2}{\pi \Delta \lambda}$$
   Eq.2-4

where λ_c is the centre wavelength of the broadband light source and $\Delta\lambda$ is the bandwidth of the light source at full-width half-maximum (FWHM). Therefore, the axial resolution can be improved by using a shorter centre wavelength and a wider bandwidth [1].

2.2.3 Fourier-Domain OCT

The previous description of the Michelson interferometer in Section 2.2.1 involves a time-domain OCT setup. In TD-OCT, a beam splitter evenly divides half of the light from a light source towards the sample, and half to a reference mirror. The light reflected from both the sample and reference mirror are combined to the beam splitter before reaching the detector [26]. Cross-sectional information across the axial line through the sample is called an A-scan and is acquired by scanning the reference arm position axially. In Fourier-domain OCT (FD-OCT), the reference mirror does not move,

but is instead replaced by either a charged coupled device (CCD) for spectral-domain OCT (SD-OCT) or a wavelength tuning light source for swept-source OCT (SS-OCT). Rather, the desired depth information is encoded in the spectrum of the processed interferogram. Performing a Fourier transform to this spectrum will provide a backreflection profile as a function of depth. Because FD-OCT does not require a translating reference mirror, the image acquisition speed is significantly increased.

The method for resolving depth without the need for a translating reference mirror is described. Eq.2-5 describes the backscattered light U at depth z.

$$U(z) = U_0 e^{-ik_0 nz}$$

$$U_z = U_0 e^{-ik_0 nz} \hspace{4cm} \textbf{Eq.2-5}$$

where U_0 is the amplitude, $k_0 = 2\pi/\lambda_0$ is the wave number, λ_0 is the wavelength, and n is the index of refraction. For a monochromatic light source, the interference at the photodetector can be represented by $I_{\Delta z}(k_0)$ and is described in Eq.2-6.

$$I_{\Delta z}(k_0) = |U_r + U_s|^2$$

$$I_{\Delta z}(k_0) = \left|U_0(e^{-ik_0 nz} + e^{-ik_0 n(z+2\Delta z)})\right|^2$$

$$I_{\Delta z}(k_0) = U_0{}^2(e^{-ik_0 nz} + e^{-ik_0 n(z+2\Delta z)})(e^{ik_0 nz} + e^{ik_0 n(z+2\Delta z)}) \hspace{2cm} \textbf{Eq.2-6}$$

$$I_{\Delta z}(k_0) = U_0{}^2(2 + e^{ik_0 n2\Delta z} + e^{-ik_0 n2\Delta z})$$

$$I_{\Delta z}(k_0) = U_0{}^2(1 + \cos(k_0 2\Delta z))$$

where U_r and U_s are the reference arm and sample arm light, respectively. They are both equal in magnitude. Note that within the cosine, the $2\Delta z$ represents the path difference between the reference and sample arms. Due to the depth dependency of the reflectivity profile, $a(z)$ can represent the reflectivity at any z position, and therefore, U_r can be

substituted with $U_0a(z)$. The intensity of the interference is now represented in Eq.2-7 and Eq.2-8 for a monochromatic and broadband light source, respectively.

$$I(k_0) = 2I_0(1 + \int_0^\infty a(z)\cos(2k_0nz)\,dz) \hspace{3cm} \textbf{Eq.2-7}$$

$$I(k) = 2I_0(1 + \int_0^\infty a(z)\cos(2knz)\,dz) \hspace{3.2cm} \textbf{Eq.2-8}$$

Here, the depth information of the OCT signal is encoded in the cosine argument. Using the Fourier transform, the intensity profile can be resolved based on depth as shown in Eq.2-9.

$$I(z) = FT\{2I_0(1 + \int_0^\infty a(z)\cos(2k_0nz)\,dz)\} \hspace{2.5cm} \textbf{Eq.2-9}$$

2.2.3.1 Spectral-Domain OCT

SD-OCT is a form of FD-OCT that uses a wide bandwidth super-luminescent diode (SLD) for its light source. SD-OCT obtains spectral information by separating the wavelengths onto a detector stripe to determine the interference spectrum, such as a high-speed CCD detector array, via a grating [26]. The information for the full depth scan can be acquired after performing a Fourier transform, but the low dynamic range of each stripe detector (compared to a single detector) negates the overall signal-to-noise ratio (SNR) advantage of FD-OCT over TD-OCT. Another drawback to SD-OCT is the dispersive elements do not separate the light evenly in wavelength on the detector, requiring signal resampling before processing, thus reducing image quality. Also, the discharge time of an individual CCD detector limits the overall imaging speed of the system.

2.2.3.2 Swept-Source OCT

The spectral components of the signal for SS-OCT are not encoded by spatial separation, but encoded in time [26]. SS-OCT utilizes a laser source of small filtered linewidths swept linearly in wavelength over time, and uses a high-speed photodetector instead of the CCD in SD-OCT. These two components of SS-OCT in combination create a time resolved spectrometer. Because the photodetector recognizes photons regardless of the wavelength, data acquisition time is minimized in comparison to the discharge time for the CCD in SD-OCT. Each wavelength sweep through the entire sweep range (spectral bandwidth) corresponds to a single axial scan. A Fourier transformation of the resulting signal is performed to reconstruct the signal information. The advantages of using SS-OCT are keeping the high SNR detection and achieving small linewidths at high frequencies to produce quality OCT images.

2.2.4 OCT Research Applications

There are many applications of OCT in the health and biomedical fields due to its advantage in detection sensitivity and fast imaging speed [27]. Even though OCT is limited to millimetre penetration depth, OCT has become an established imaging modality for beneath skin imaging.

2.2.4.1 OCT in Ophthalmology

Retinal OCT has been a mainstay in OCT applications due to the high transmission and low scattering regions of the eye – effective conditions for OCT imaging. OCT can provide high depth resolution at a low NA for larger depth of focus, which is ideal for retinal imaging. The development of ultrabroad-bandwidth light

sources has enabled ultrahigh-resolution (UHR) OCT techniques for studies such as the direct correlation of photoreceptor loss with retinal function in Stargardt's dystrophy [28] and therapy monitoring for eye disease pathogenesis [29-31].

2D retinal imaging of multiple B-scans have also advanced into 3D retinal imaging to provide improved volumetric structural information for disease assessment, especially for *in vivo* imaging. FD-OCT techniques provide the high-speed requirement vital for 3D *in vivo* imaging in virtual biopsy and surgery. The rotation of the 3D volume has also enabled "fly through" features to obtain further position and orientation data for diagnostic needs [32]. Examples of 3D retinal imaging studies include 3D volume optic nerve and skin imaging constructed from 2D images at different depths [33], as well as 3D UHR OCT images with SD-OCT A-scans [34].

High definition 3D images of the normal retina and optic nerve head have been obtained by an ultrahigh speed SS-OCT retinal imaging system at 249,000 A-scan per second at 1060 nm wavelength [35]. This imaging system allowed increased light penetration to view the choroid, lamina cribrosa, and sclera. *En face* images were also acquired to visualize the nerve fibre layer, photoreceptors, and even capillaries of the retina. The high resolution and speed capabilities of SS-OCT are clear advantages that are maximized with this imaging modality for specific ophthalmologic studies.

2.2.4.2 Intravascular OCT

Non-invasive imaging techniques for cardiovascular studies have been challenging due to the small diameter and tortuosity of microvasculature [27]. The use of

optical probes and catheters has enabled OCT intravascular imaging of blood vessels for various cardiovascular studies, overcoming those challenges.
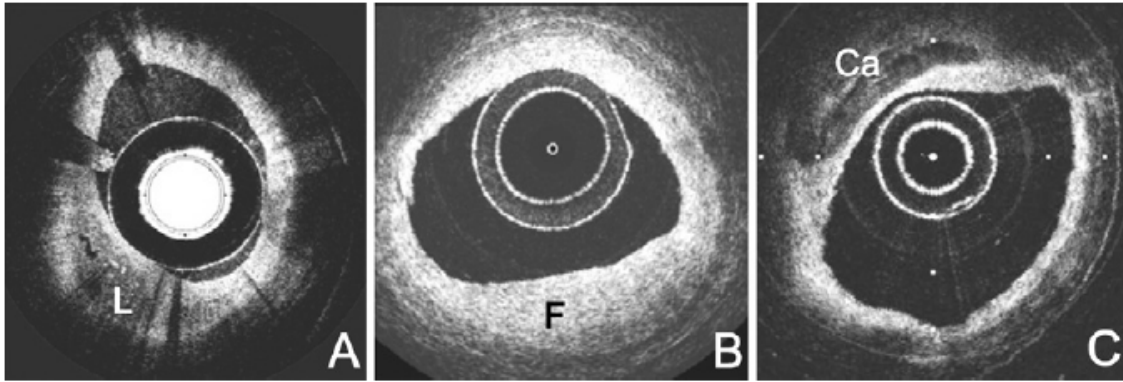
Figure 2-4: TD-OCT images at λ=1300 nm of lipid-rich (A), fibrous (B), and calcific (C) coronary atherosclerotic plaque types. Lipid-rich (L) and calcific (Ca) regions appear as a signal-poor region within the vessel wall. The OCT signal of fibrous plaque (F) is observed to be strong and homogeneous [27].

Fibre optics using low coherence interferometry has been utilized for atherosclerosis imaging. *In vivo* images of atherosclerotic plaque types (Figure 2-4) have been obtained and are comparable in features to *ex vivo* gold standard atherosclerosis plaque characterizing studies. The *in vivo* results were also consistent with results from intravascular ultrasound (IVUS) – the benchmark for intracoronary imaging [36-38]. Intravascular OCT is also used for detecting atherosclerotic lesions, including features such as vessel wall appearance, subintimal area reflectivity, and internal elastic membrane discontinuation [39]. Plaque rupture has also been studied and OCT images showed the morphology for the ruptured plaque analyzed [40].

Statin research and stent implantation are two other research areas where intravascular OCT has provided great adaptations to previous approaches. Intravascular OCT has aided statin therapy, a process to lower lipid concentration, by providing images

of the fibrous cap thickness. This measure is vital to the assessment of statin levels for patients that require lipid concentration monitoring [41]. Stent implantation is used to avoid arterial reocclusion. OCT has already been used to image *in vivo* to help prototype the appropriate stent strut for the vessel wall. IVUS cannot detect neointimal layers for the sirolimus eluting stents, thus OCT is a suitable choice for visualization thin neointima of each stent strut. [42]

2.2.4.3 OCT in Oncology

Early detection and assessment of malignant neoplasm is vital to the clinician in providing the appropriate patient treatment and care. OCT is an imaging modality that can provide optical biopsies at high resolutions comparable to histopathology without the need for tissue removal. This capability will allow clinicians to better identify malignancies at curable stages. OCT is also involved in aiding surgical resection, radiation therapy, and analyzing tumour death and tissue pathology [26].

OCT presents its greatest potential in the imaging of epithelial cancers due to the high quality imaging of epithelial structures for identifying cancers at an early stage. OCT is able to differentiate the tissue layering and assess cancer growth by observing surface specialization (cilia or keratin), cell shape and layers. Additional OCT techniques such as speckle variance analysis, polarization sensitivity, and elastography are also applied to better analyze these factors in OCT imaging due to the lack of contrast in identifying these factors [26].

The study of cancers via OCT imaging has provided clinicians with valuable information in disease analysis. OCT has been used to image tissues with esophageal,

bladder, lung, breast, colon, skin, and many other cancers. OCT can adequately detect the presence and absence of markers such as calcium deposits and also differentiate glandular structures and tissue boundaries, basement membranes, and cell morphologies. These markers are determined after comparing the processed OCT images (taken in real time) with the corresponding histology [26].

2.3 Detecting Apoptosis

The detection of apoptosis will allow better analysis of tissue development and tumour responses to anticancer drugs. Real-time non-invasive apoptosis measurements have been performed to observe the kinetics and methods for inducing apoptosis. These apoptotic tissue regions produce increased ultrasound backscatter that can be detected and differentiated from non-apoptotic regions. The monitoring of these tissues has led to studies of tissue response to treatments for indications of *ex vivo* and *in vivo* programmed cell death [43]. Figure 2-5 depicts the result of ultrasound imaging of apoptotic cells and shows the change in scattering as a function of exposure time (which is related to the number of cells responding to the treatment).
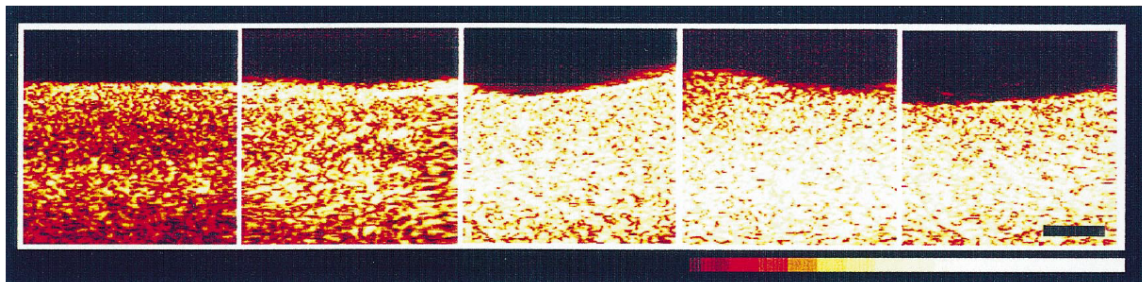
Figure 2-5: Results of 40 MHz ultrasound imaging of centrifuged apoptotic cells. Each panel refers to a representative ultrasound scan of a pellet of acute myeloid leukemia (AML) cells. From left to right, panels correspond to cells treated with cisplatinum for 0, 6, 12, 24 and 48 h to induce varying degrees of apoptosis. The scale bar indicates 1 mm [43].

2.3.1 Principle

In OCT, speckle intensity measurements are a tool for assessing different tissue types [11]. The speckle can change due to the size, number, and optical properties of the scatterers in the medium imaged. The speckle occurs in living tissues due to the fluctuations of subresolution scatterers, including those caused by the intracellular motion from mitosis, organelles movements, and other cellular morphological changes in connection with apoptosis. Apoptosis involves the programmable structural and biokinetic changes that ultimately results in cell death [44]. An apoptotic cell exhibits shrinking, nuclear fragmentation, membrane blebbing, and organelle disintegration. These responses are of interest in cancer therapies where the chemotherapeutic drug will induce cancer cells to undergo apoptosis in order eradicate the tumour [11].

2.3.2 Apoptosis Detection Using OCT

Dynamic light scattering has been adapted for OCT to measure intracellular motion (IM) for detecting and differentiating between viable and apoptotic cells due to changes in the rate of IM, in an *in vitro* setting [11]. The decorrelation rate of speckle for these cisplatin-treated acute myeloid leukemia (AML) cells undergoing apoptosis was measured from multiple consecutive SS-OCT images. This technique incorporated the "heterodyne approach" in removing contributions from static scattering components [45], to produce an average decorrelation time (DT) used as the overall measurement of IM. The DT is measured by the half width of the intermediate scattering function (calculated from the intensity autocorrelation function) at half its maximum value and describes how

21

quickly the speckle intensity changes. Alternatively, the time it takes for the intermediate

scattering function to fall below 1/e can also be used as the measure of the DT. The cell

morphologies over time, assessed by H&E histology, indicated membrane blebbing and

fragmentation, which, in combination with the decreasing DT, was used to explain the

decrease in DT (thus increase in IM) caused by the cell structural changes during

apoptotic cell death [11]. Figure 2-6 depicts the histology and signal intensity curves of a

single pixel in the OCT image of cisplatin treated cells over time. Figure 2-7 shows the

decrease of DT over time.
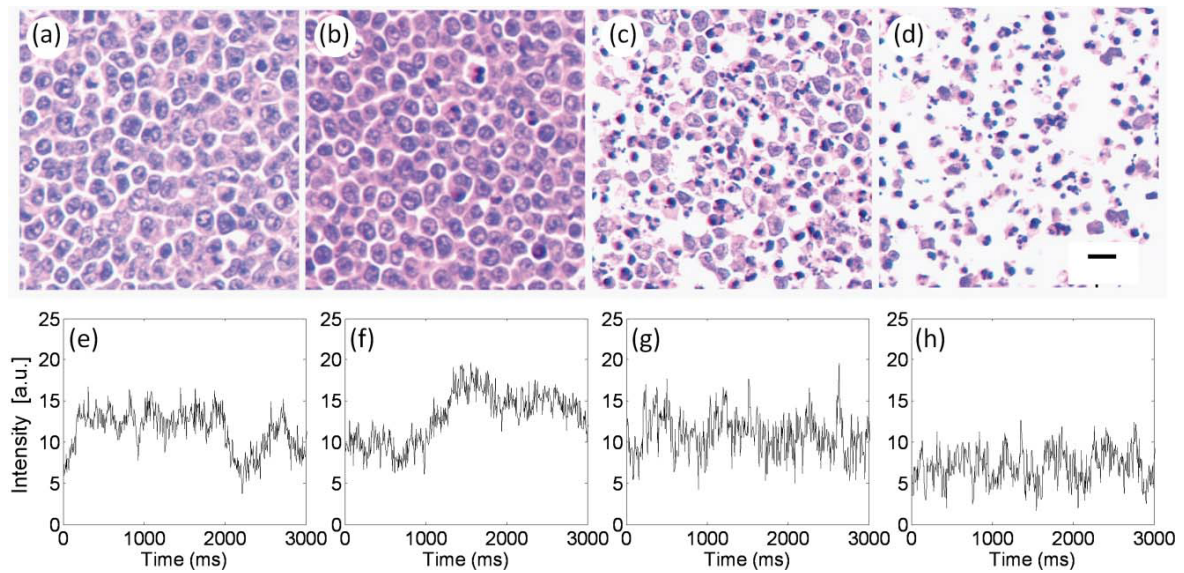
Figure 2-6: Hematoxylin and eosin (H&E) stained sections obtained from cisplatin treated cells after (a) 0 h, (b) 12 h, (c) 24 h, and (d) 48 h of treatment. The scale bar represents 10 μm. Representative signal intensity curves from a single pixel at (e) 0 h, (f) 12 h, (g) 24 h, and (h) 48 h [11].
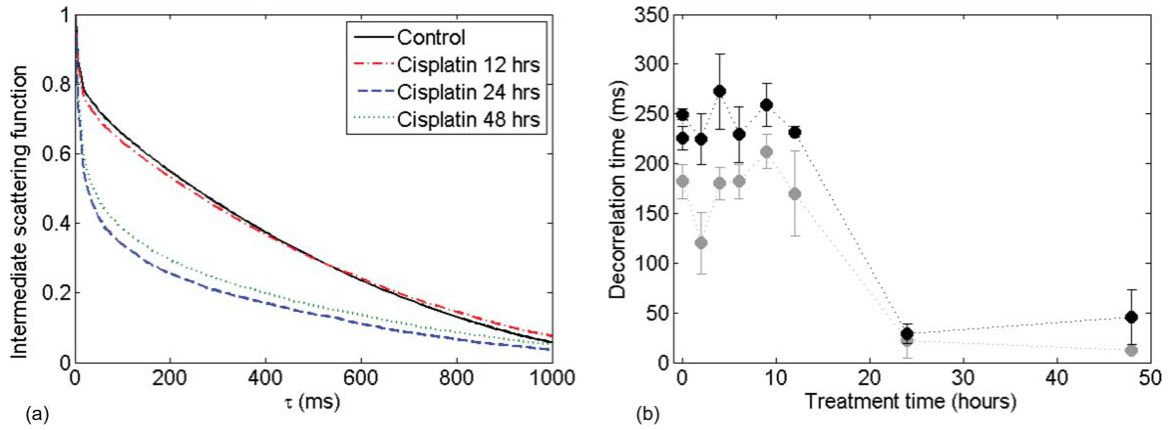
Figure 2-7: (a) Average intermediate scattering functions computed from a selected ROI in AML cell pellets. (b) Decorrelation time computed from AML cell samples treated with cisplatin over a 48 h period. Each curve corresponds to a separate experiment. Error bars represent the standard deviation of 10 separate measurements from each sample [11].

This *in vitro* test has shown the technique's sensitivity to IM variations, which is correlated to cell death. The DLS technique applied to OCT utilizes signal fluctuations in the DT calculations instead of absolute value of signal intensity, thus minimizing the effects of signal attenuation and scattering angle on the measured signal, which makes this technique advantageous over other methods that measure OCT backscatter strength or attenuation to detect cell death [46]. The drawback for this method is the increased sensitivity to rapid bulk tissue motion and *in vivo* blood flow. Therefore, an image processing technique for vascular segmentation is required to correct the DT maps produced in the *in vivo* setting.

The DLS-OCT technique has been implemented *in vivo* for cell death detection in a mouse tumour model for feasibility testing [12]. Human bladder carcinoma tumours were grown on three nude mice and imaged with OCT. DT maps were generated for tumour and skin regions of the mice before and after chemotherapy treatment. Figure 2-8

23

shows the tumour and skin regions on the OCT image, with the respective DT map and autocorrelation curves.
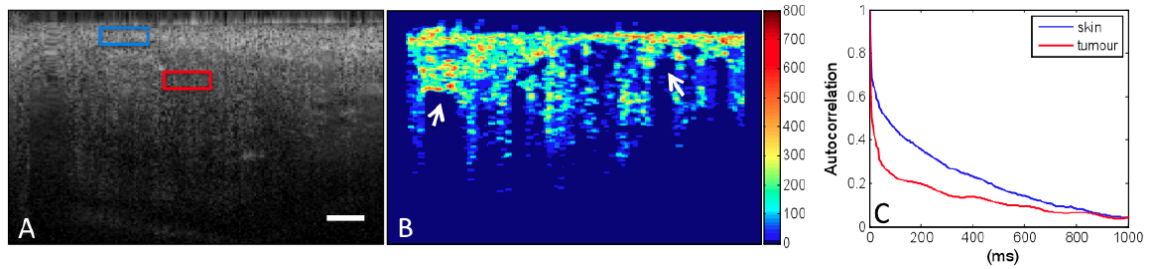
Figure 2-8: Comparing decorrelation in skin versus tumour tissue. OCT b-mode image (A), decorrelation map (B) and average autocorrelation functions obtained from regions of skin and tumour highlighted in A (C). White arrows point to regions of blood flow represented by very short DT. Scale bar in the OCT image is 300 μm and the decorrelation times in ms are indicated by the colour bar [12].

DT differences were observed over time, including the DT increase at 24 and 48 hours for the *in vivo* mouse tumours [12], which differed from the *in vitro* data where DT decreased over time [11]. These preliminary results showed the feasibility of DLS-OCT for IM measurements, but required further experimental analysis to confirm the previous *in vivo* results with stronger statistical significance. This thesis provided further analysis in a larger n=10 mice study that built on this initial *in vivo* feasibility test [12].

Chapter 3: Experimental Methods

The experimental methods for this thesis include the setup of: (a) the imaging system and (b) the design and implementation of the animal experiment. A swept-source optical coherence tomography (SS-OCT) system was used for the *in vivo* mouse tumour imaging. The animal experimental setup involved the preparation of the tumour cell line, nude mice, window chamber surgeries and chemotherapy drug. Methods were also developed for the data acquisition and analysis, as well as the histology staining. Figure 3-1 is an example set of histology images, OCT b-mode images and decorrelation time maps for a previous DLS-OCT study with a similar methodology to this thesis [12].
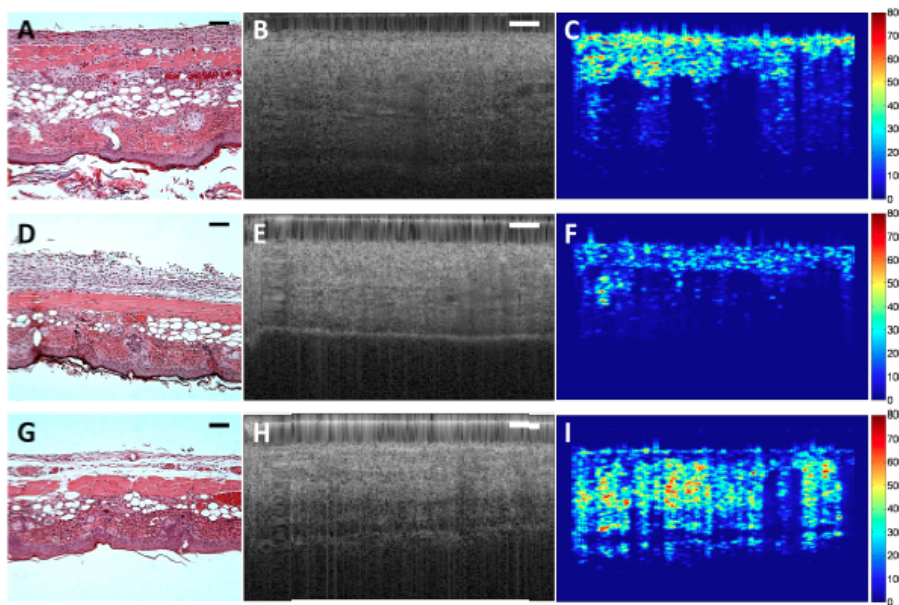
Figure 3-1: Variations in skin structure. The left column shows H&E stained sections of three mice. The middle column shows the corresponding OCT b-mode images. The right column shows decorrelation time maps processed from the OCT b-mode images. Scale bars are 50 μm (histology) and 300 μm (OCT and decorrelation time maps). Decorrelation times are in milliseconds [12].

3.1 Imaging System Setup

A SS-OCT system was used for all of the *in vivo* experiments for this thesis. This system was designed and housed at the Princess Margaret Hospital on the 7th floor Wilson Lab. The members of the Biophotonics and Bioengineering Lab at Ryerson University and the Vitkin and Wilson Labs at Ontario Cancer Institute (University Health Network) and University of Toronto constructed this system based on the design of the Harvard Medical School and Wellman Laboratories for Photomedicine at Massachusetts General Hospital in Boston, Massachusetts, USA [47].

3.1.1 Imaging System Rationale

A dynamic light scattering-optical coherence tomography (DLS-OCT) imaging system was designed to measure subtle differences in motion related to cell viability. A SS-OCT setup was used due to its high speed and SNR. A DLS-OCT setup had been used previously to measure *in vitro* changes in intracellular motion caused by apoptosis in acute myeloid leukemia cells treated with cisplatin [11]. The SS-OCT system had been used in previous *in vivo* mouse studies involving the imaging of tumour network microvasculature [48].

3.1.2 Imaging System Specifications
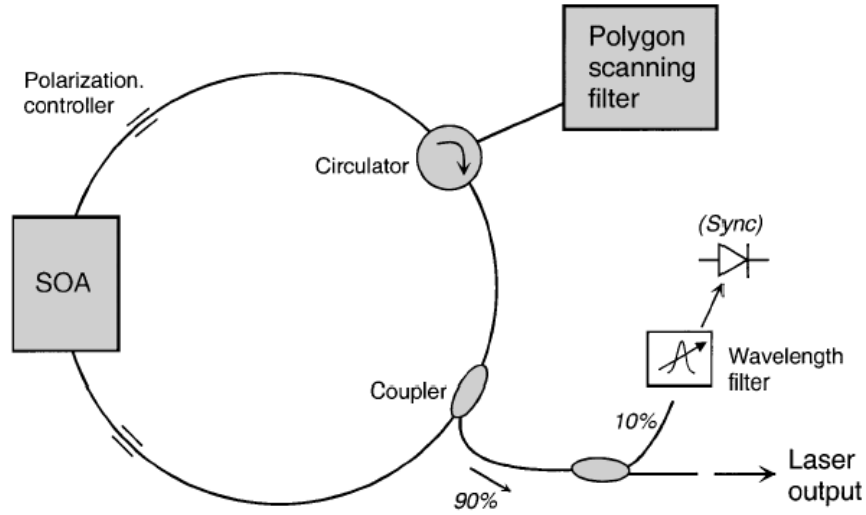
Figure 3-2: Schematic for the high-speed wavelength-swept semiconductor laser with a polygon filter [47].

The laser for the SS-OCT system was a high-speed wavelength-swept semiconductor laser with a polygon wavelength filter [47]. A unidirectional fibre optic ring, a semiconductor optical amplifier as the gain medium, and a novel polygon-scanning filter were used. Centred at a 1310 nm wavelength with a bandwidth of ~110 nm and scan rate of 36 kHz, this laser was built with components that provided optimized power and tuning speed. Figure 3-2 has a schematic of this laser setup.

Raw OCT signals were continuously acquired by the ATS460 (AlazarTech) data acquisition card, and transferred to the memory of the video graphics card GeForce 9800 GT (NVIDIA). To manipulate and reconstruct the OCT images, custom-written kernels with the built-in CUDA libraries were utilized for massive parallel data processing. CUDA libraries and a specific DAQ card were used to enhance data throughput, while freeing up CPU resources. Direct data processing on the graphics card allowed the reconstructed OCT image to be displayed without the use of additional memory

transactions, thus allowing real-time image acquisition, processing, and display to be only limited by the A-scan rate of the laser.

3.2 Animal Experimental Setup

The preparations for the animal experiment included the setup of the Animal Use Protocol (AUP 1280.8) at the University Health Network (Ontario Cancer Institute) at Princess Margaret Hospital in downtown Toronto, ordering the nude mice for the experiment, acquiring and growing the tumour cell line for tumour implantation, setting up and performing the dorsal skin window chamber surgeries, and acquiring the drug for chemotherapy treatment. Refer to Appendix A for an excerpt of the Animal Use Protocol used for this mice experiment.

3.2.1 Animal Protocol Design

A functional extension of optical coherence tomography capable of detecting cell death *in vitro* led to an initial n=3 tumour mouse model study to test the feasibility of this imaging technique *in vivo* [12]. In this thesis, this same technique was performed in an n=10 mice study to further evaluate the technique's effectiveness in cell death detection and obtain stronger statistical significance. Photodynamic therapy had been previously used to induce tumour cell kill [48], but due to its significant vascular damage, a human bladder carcinoma cell line in conjunction with a single dose of cisplatin was used in this feasibility test to evaluate the efficacy of this functional imaging technique.

The dorsal skin-fold window chamber, used previously in PDT and OCT microvasculature studies [11, 12, 48], was mounted on ten female nude mice (NCRNU-F,

Taconic), providing a suitable optical window for imaging and treatment of the microvasculature. The tumours were implanted into the fascia of the subcutaneous layer on the skin opposite of the window. A total volume of 10 µl of HT-1376 (ATCC) human bladder carcinoma cells, suspended in growth medium, was injected at a concentration of 1.3×10^7 cells/mL. This cell line was grown at the Advanced Biomedical Ultrasound Imaging and Therapy Lab at Ryerson University. During this process, the mice were placed under ketamine/xylazine (10/80 mg/kg) anesthesia and kept warm on a heated pad. The mice were allowed to recover and were assessed on a daily basis during a two-week period of tumour growth until approximately 1-2 mm in diameter.

Table 3-1: Mice experiment chart detailing the mice and the performed treatments and sacrifice date.

Mice	Window Chamber	Tumor Implantation	Cisplatin Injection	Day 0 Imaging	Day 1 Imaging	Day 2 Imaging	Day to Sacrifice
#1	✓	✓		✓			0
#2	✓	✓		✓	✓		1
#3	✓	✓		✓	✓	✓	2
#4	✓	✓	✓	✓	✓		1
#5	✓	✓	✓	✓	✓		1
#6	✓	✓	✓	✓	✓		1
#7	✓	✓	✓	✓	✓	✓	2
#8	✓	✓	✓	✓	✓	✓	2
#9	✓	✓	✓	✓	✓	✓	2
#10	✓	✓	✓	✓	✓	✓	2

Table 3-1 depicts the treatments performed and sacrifice date of each of the ten mice in this *in vivo* tumour study. All ten mice were treated with a 100 mg/m^2 dose of chemotherapy drug cisplatin via tail vein injection after DLS-OCT imaging on Day 0. The imaging data was obtained again on Day 1 and Day 2 (time points 24 hours and 48 hours after cisplatin injection). In total, there were three control mice, three mice for the "Day 1" datapoint (24 hours after cisplatin exposure), and four mice for the "Day 2"

datapoint (48 hours after cisplatin exposure). All procedures including surgeries, cisplatin injection, and imaging were conducted under ketamine-xylazine anesthesia (10/80 kg/mg) administered intraperitoneally.

The original treatment regimens of several mice in certain designated groups (as outlined in Table 3-1) were modified due to premature mouse deaths. It is important to outline these modifications so that the results from the thesis match with the original data sets taken during the experiment. An example of these survival changes was a mouse that was previously planned to be sacrifice on Day 2 (Mouse 3). Because it showed signs of weakened health, it was sacrificed on Day 0 instead. The initially planned mouse for Day 0 sacrifice (Mouse 1) was sacrificed on Day 1, and the initially planned mouse for Day 1 sacrifice (Mouse 2) was sacrificed on Day 2. The new mice experiment chart is shown in Table 3-2.

Table 3-2: Revised mice experiment chart detailing the mice and the performed treatments and sacrifice date.

Mice	Window Chamber	Tumor Implantation	Cisplatin Injection	Day 0 Imaging	Day 1 Imaging	Day 2 Imaging	Day to Sacrifice
#3	✓	✓		✓			0
#1	✓	✓		✓	✓		1
#2	✓	✓		✓	✓	✓	2
#4	✓	✓	✓	✓	✓		1
#7	✓	✓	✓	✓	✓		1
#9	✓	✓	✓	✓	✓		1
#5	✓	✓	✓	✓	✓	✓	2
#6	✓	✓	✓	✓	✓	✓	2
#8	✓	✓	✓	✓	✓	✓	2
#10	✓	✓	✓	✓	✓	✓	2

3.3 Data Acquisition and Analysis

For each mouse imaged, a total of twenty-six imaging planes of two-dimensional frames of OCT data were acquired continuously for 1000 frames, and spanned over the whole tumour area of the window chamber. The time required for imaging the 1000 frames was 10 seconds. Therefore, the frame rate for imaging the two-dimensional planes was 100 frames per second. The imaging planes were spaced approximately 25 μm apart and covered the tumour and non-tumour skin regions. The frame acquisition rate was 200 frames per second. For each frame, 360 A-scans covered the entire 3 mm lateral distance. Figure 3-3 has a schematic of this experimental setup. Refer to Appendix B for more images of the experimental setup.
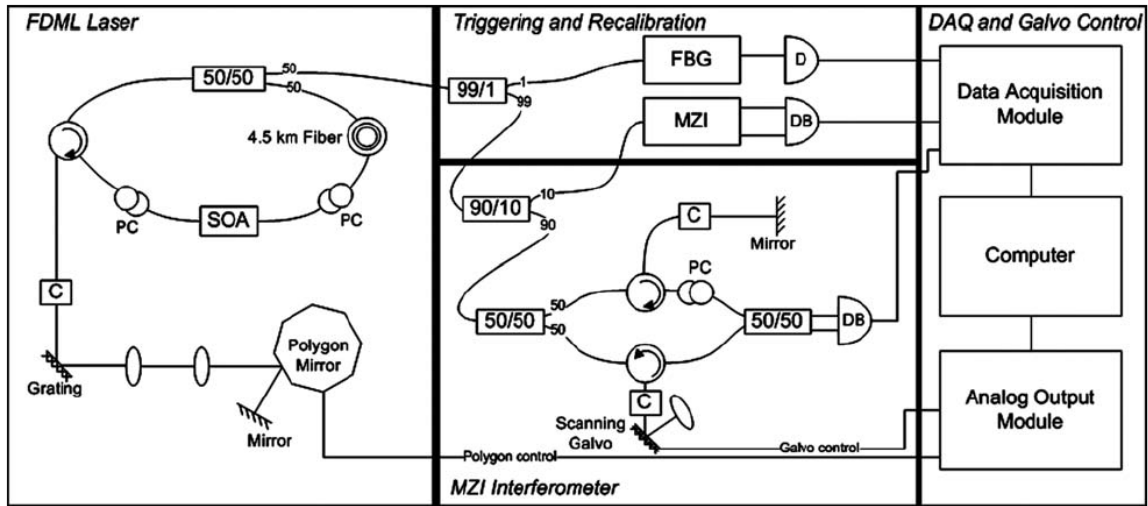
Figure 3-3: Schematic for the SS-OCT system. SOA, semiconductor optical amplifier; PC, polarization controller; C, collimator; FBG, fibre Bragg grating; MZI, Mach-Zehnder interferometer; D, detector; DB, dual balanced detector [48].

The multiple two-dimensional frames for each imaging plane were used to generate decorrelation time (DT) maps. The methods established by Farhat et al. were used for the analysis of the OCT data [12]. The DT for each pixel of each imaging plane was determined by calculating the autocorrelation function of the fluctuating signal by

taking the inverse Fourier transform of the power spectrum [11]. The autocorrelation function and the signal's power spectrum are Fourier transform pairs. Vital to the calculation of the autocorrelation function was the static scattering component of the tissue. The tumour tissue samples were assumed to be a nonergodic medium, thus required the removal of the static scattering component from the fluctuating signal. This was done by the "heterodyne approach" [45] that removed the static scattering contribution of the 7 by 7 pixel region centred at the specific pixel from the intensity autocorrelation function to produce the heterodyne intermediate scattering function (ISF). The 1/e value of the heterodyne ISF was then used to calculate the DT that was displayed in the final DT map in conjunction with 3 by 3 spatial averaging. Refer to Appendix C for the MATLAB code that was used to generate the DT maps, and Appendix D for further explanation on the equations used in the "heterodyne approach".

The averages of the DT values within a selected region of interest were analyzed to observe tumour changes due to intracellular and extracellular motion. Thresholding was applied to the DT maps to remove the contribution from rapid bulk motion and blood flow (the results from the thresholding are presented in Section 4.2). The DT values that were less than the threshold value were reassigned to a value of zero. A modified "jet" colour bar setting in MATLAB was used for the post-threshold DT maps, with black coloured pixels indicating an assigned DT value of zero. Statistical analysis via the Student's t-test was performed to compare the means of the average DT values of the control and cisplatin mice.

3.4 Histology

The ten mice in this *in vivo* tumour study were sacrificed according to Table 3-2. For each mouse, the tumour was excised and fixed in 10% buffered formalin for 24 to 48 hours before submission to the University Health Network Pathology Research Program. The tissue samples were processed for hematoxylin and eosin (H&E) staining. The subsequent slides were scanned using a Leica DC 200 digital imaging system (Leica Microsystems GmbH, Germany) at 4x and 10x objective lens magnification.

Chapter 4: Results

The results include the collection of two types of OCT images (OCT b-mode images and decorrelation time maps) from the dynamic light scattering optical coherence tomography (DLS-OCT) experiment and the corresponding tissue histology. OCT b-mode images provide information on the structure and optical scattering properties of the sample. Decorrelation time maps provide information on the motion in sample tumour tissue. The histology images from hematoxylin and eosin (H&E) staining provide a means for visualizing the different cellular structures of the sample.

4.1 Images Acquired

To perform DLS-OCT imaging, the swept source OCT imaging system was used to obtain the data that formed the b-mode images. Post-processing techniques were used to obtain the decorrelation time maps from the b-mode images using MATLAB software as described in Section 3.3. The histology images were prepared as described in Section 3.4.

Representative images from the Mouse 6 and Mouse 10 tumours are presented in this chapter (even though all the data were collected according to Table 3-2). Mouse 6 and 10 were chosen primarily because: 1) both of these mice had data for the full three-day duration of the experiment enabling tumour analysis over time; and 2) both mice had images (b-mode, DT, and histology) that had full grown tumours of 1-2 mm in diameter.

4.1.1 OCT B-mode images
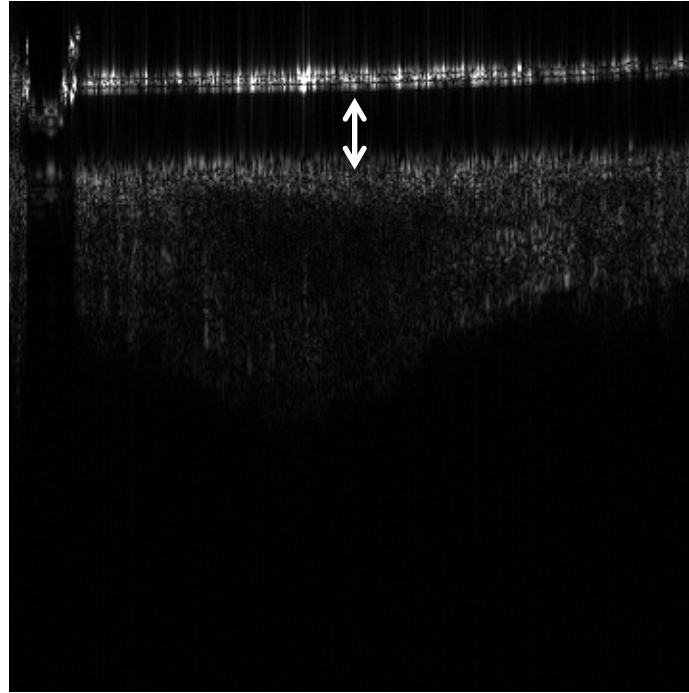
(a)
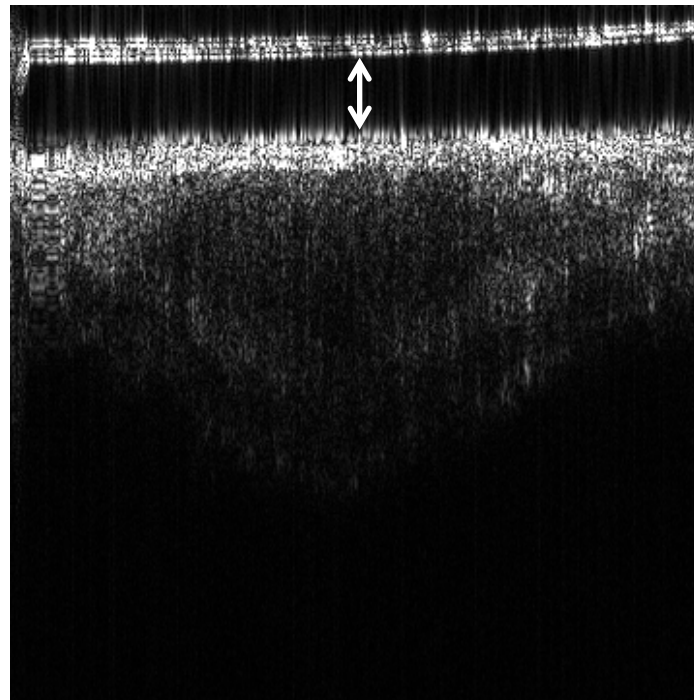
(b)

Figure 4-1: A cross-sectional (b-mode) image of the tumour for (a) Mouse 6 on Day 1 and (b) Mouse 10 on Day 2. The white arrows represent the 0.25 mm thickness of the glass coverslip. The image height and image width are both 3 mm.

Figures 4-1a and 4-1b are examples of cross-sectional (b-mode) OCT images taken at the location of a tumour implanted onto the dorsal skin of Mouse 6 and 10, respectively. These b-mode images were formed from depth profiles (A-scans) taken across a 3 mm lateral distance. The brightness of the pixels within these images indicates the intensity of the backscattered light received by the OCT detector. The b-mode images provide structural information of the sample based on the backscattering. In this example, the glass coverslip for the window chamber is defined by the dark area between the bright lines that lies above the highly scattering tumour sample. The tumour is confined to the area of reduced scattering in the image. A collection of b-mode images were subsequently used to formulate the respective decorrelation time map using post-processing techniques.

4.1.2 Decorrelation Time Maps

DT Map (no threshold) M6, Day 1, Plane 7; DT in ms

(a)

DT Map (no threshold) M10, Day 2, Plane 12; DT in ms

(b)
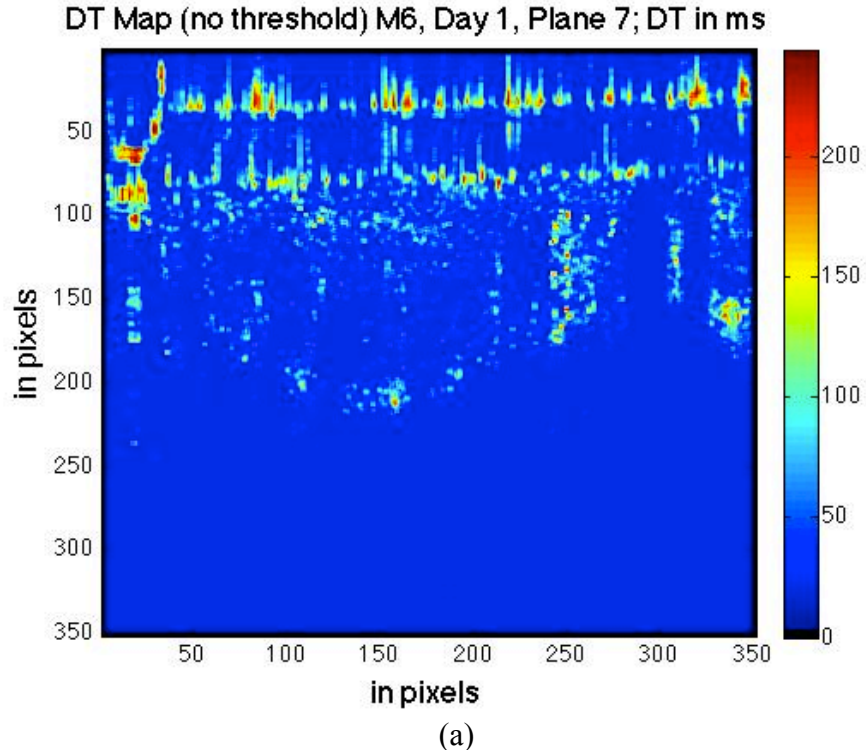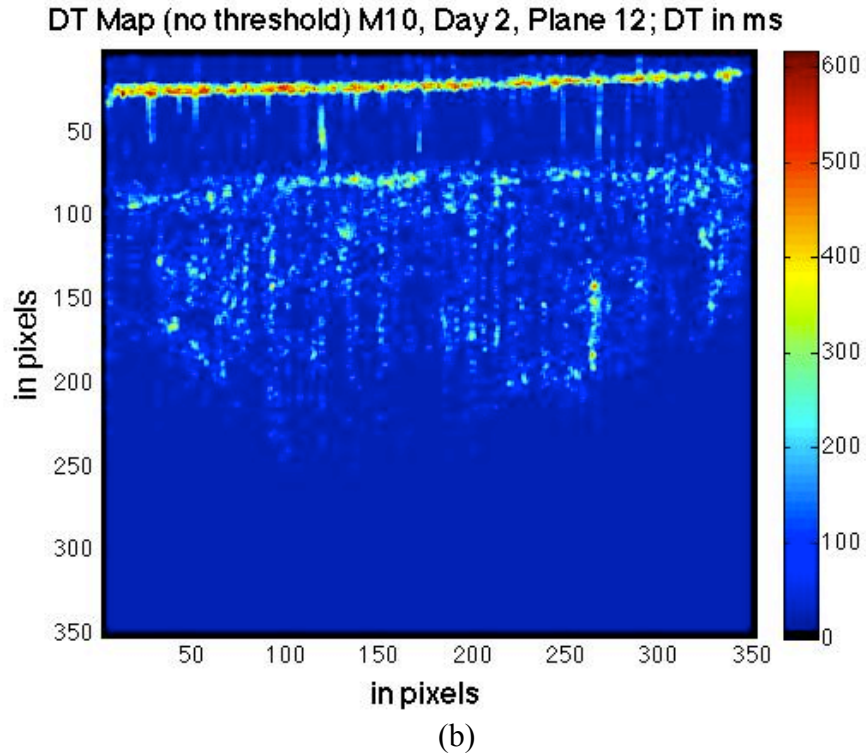
Figure 4-2: DT map of the mouse tumour produced from OCT b-mode images using a decorrelation-based algorithm for (a) Mouse 6 (Day 1) and (b) Mouse 10 (Day 2). The colour map represents the DT value in ms. The image height and image width are both 3 mm.

Figures 4-2a and 4-2b are examples of decorrelation time (DT) maps produced from the original b-mode images using a decorrelation-based algorithm (described in Section 3.3) for Mouse 6 and 10, respectively. The initial data collected for each cross-sectional imaging plane of the tumour included multiple frames (separated in time by 10 ms) imaged at 100 frames per second. Intensities at a specific pixel location across the acquired frames were calculated by the algorithm. An example of the fluctuations in signal intensity is shown in Figure 4-3a for Mouse 6 (Figure 4-4a for Mouse 10) for frame 101 to 200 of the total 1000 frames of data imaged. The power spectrum of the pixel intensities is shown in Figure 4-3b (Figure 4-4b for Mouse 10). The resulting

37

inverse Fourier transform of the power spectrum of the signal intensities of the same pixel is shown in Figure 4-3c (Figure 4-4c for Mouse 10). The intermediate scattering function (ISF, from the "heterodyne approach") of the same pixel is shown in Figure 4-3d (Figure 4-4d for Mouse 10). Lastly, the curve showing the DT value recorded in the DT map (determined from the heterodyne ISF for each pixel as the time it takes for the signal to fall below the value of 1/e) is displayed in Figure 4-3e (Figure 4-4e for Mouse 10). For Figure 4-3, point (128,154) of plane 7 for Mouse 6 on Day 1 was chosen as a pixel with a DT of 86.67 ms. For Figure 4-4, point (150,150) of plane 12 for Mouse 10 on Day 2 was chosen as a pixel with a DT of 20 ms.

(a)

Power Spectrum of point (128,154) M6, Day 1, Plane 7

(b)

Inverse FFT for point (128,154) M6, Day 1, Plane 7

(c)

39

Heterodyne ISF for point (128,154) M6, Day 1, Plane 7

(d)

To calculate DT for point (128,154) M6, Day 1, Plane 7

(e)

40
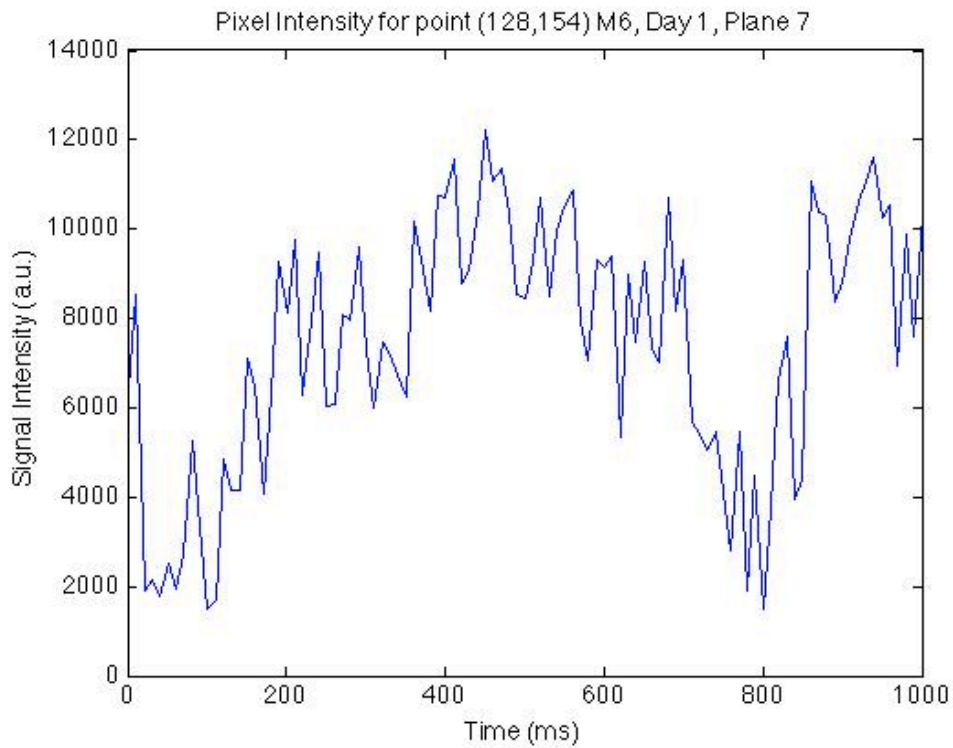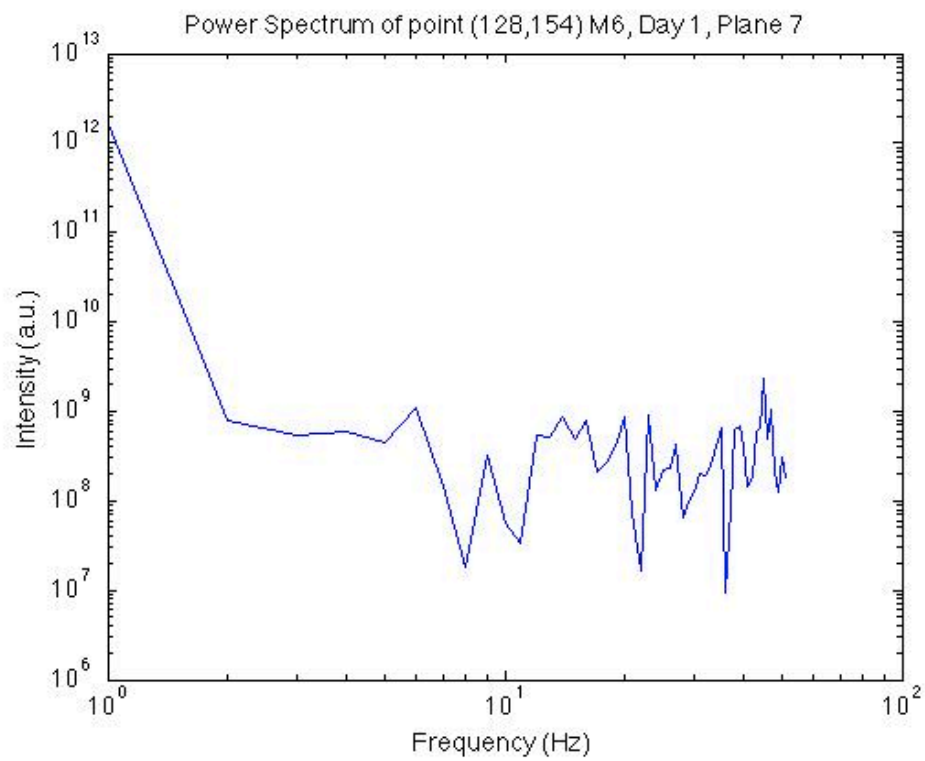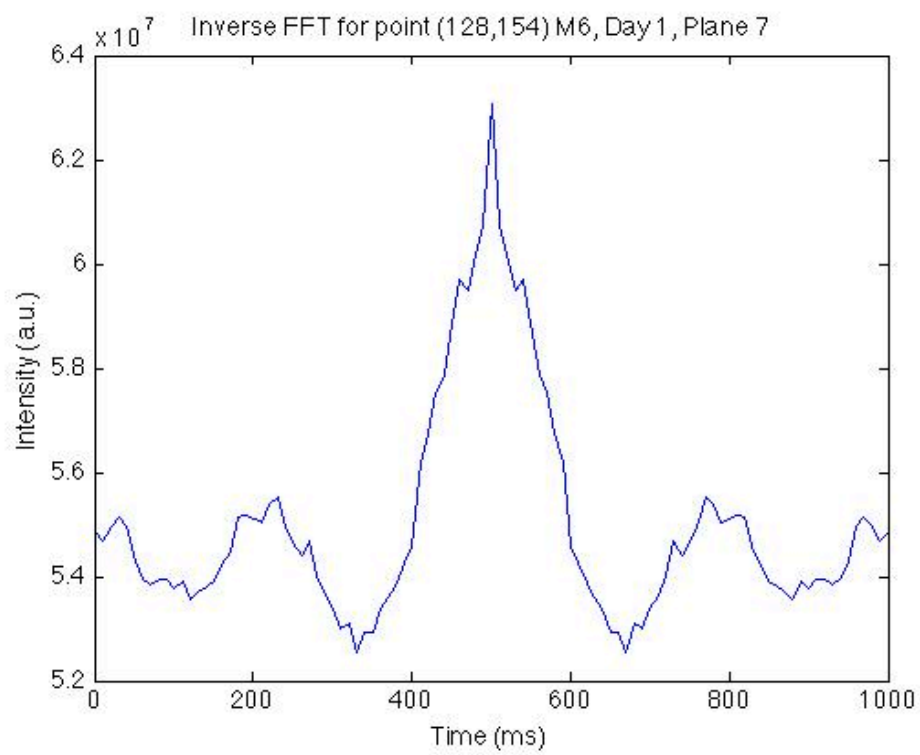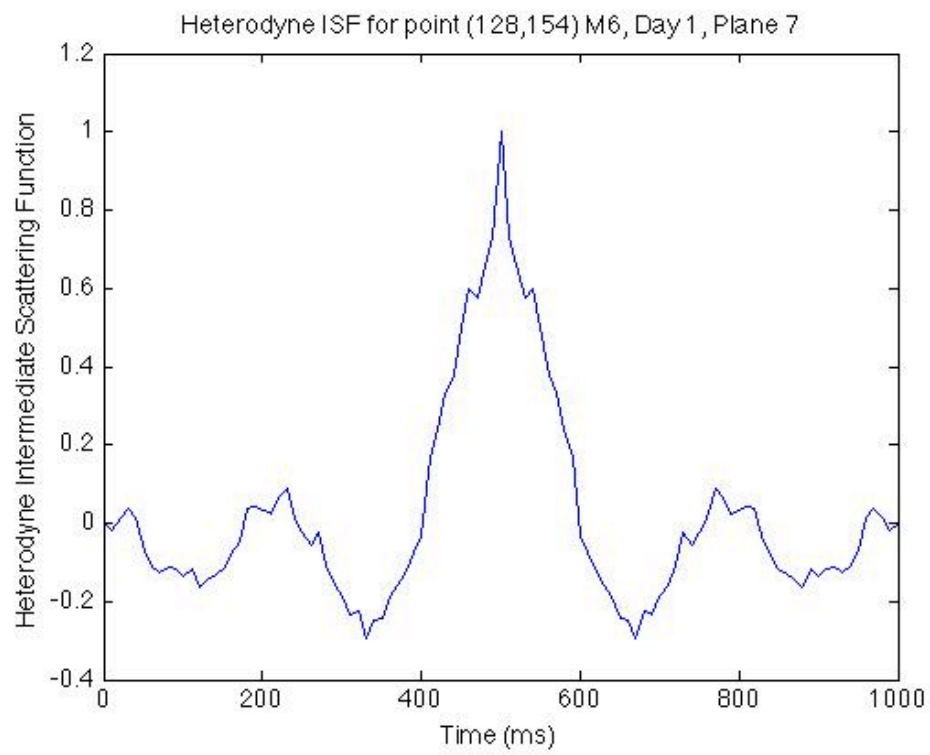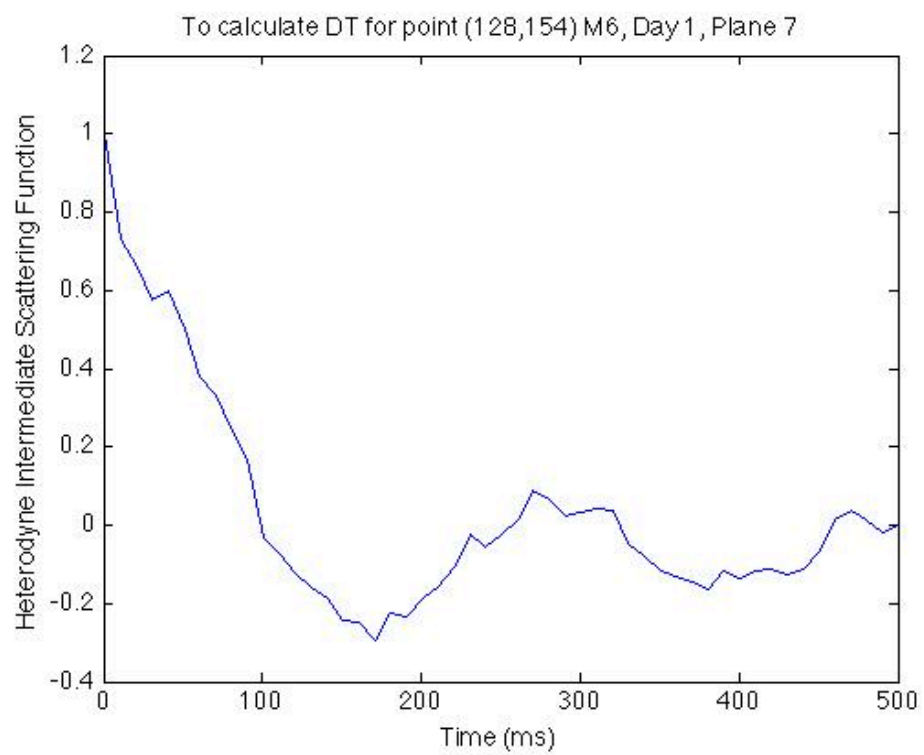
Figure 4-3: (a) The fluctuations in signal intensity for point (128, 154) across multiple OCT timeframes for Mouse 6 (Day 1); (b) The power spectrum of the pixel intensities in (a); (c) The inverse Fourier transform of the power spectrum in (b); (d) The heterodyne intermediate scattering function produced using the Joosten algorithm [45]; (e) The resulting curve used to choose the DT value (the decorrelation time is the time chosen when the heterodyne ISF drops below the value of 1/e).

(a)

(b)

(c)

Heterodyne ISF for point (150,150) M10, Day 2, Plane 12

(d)

To calculate DT for point (150,150) M10, Day 2, Plane 12

(e)

43
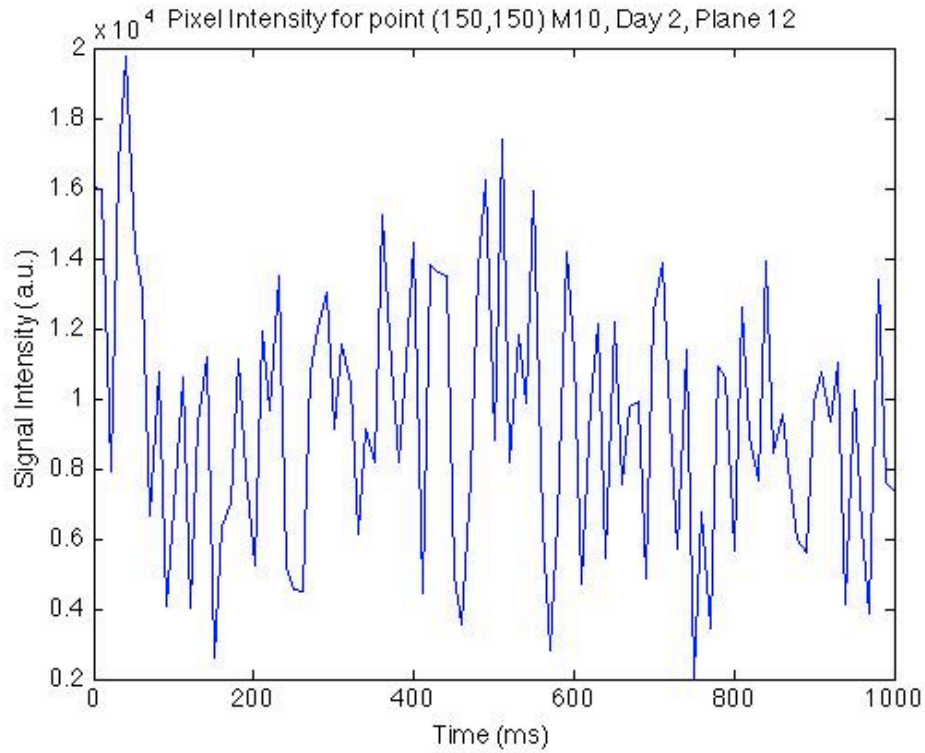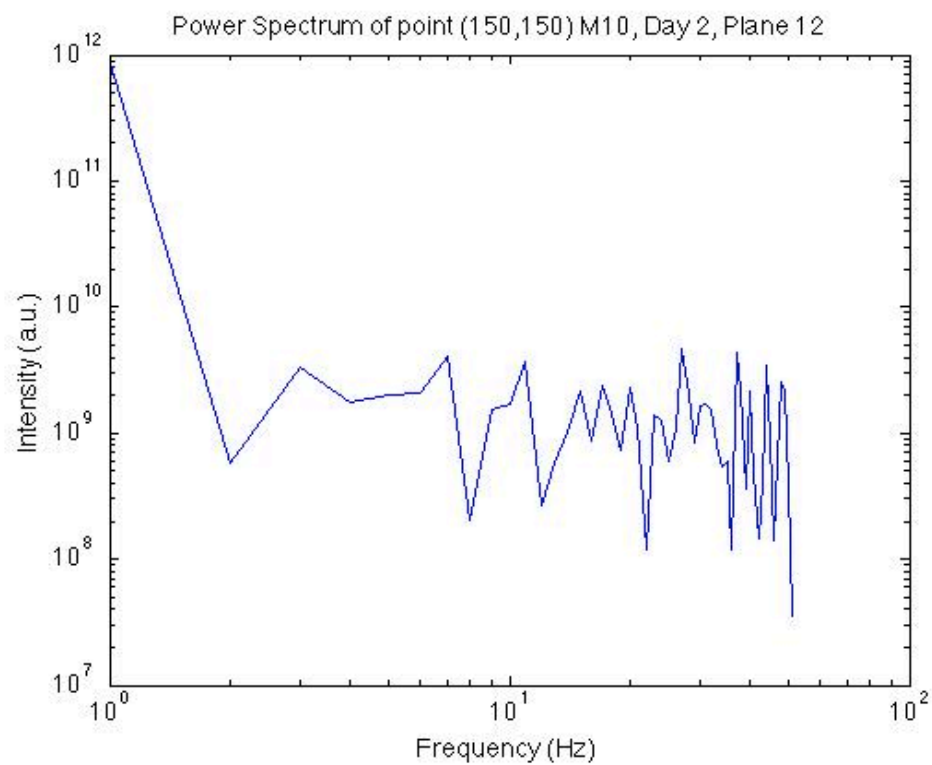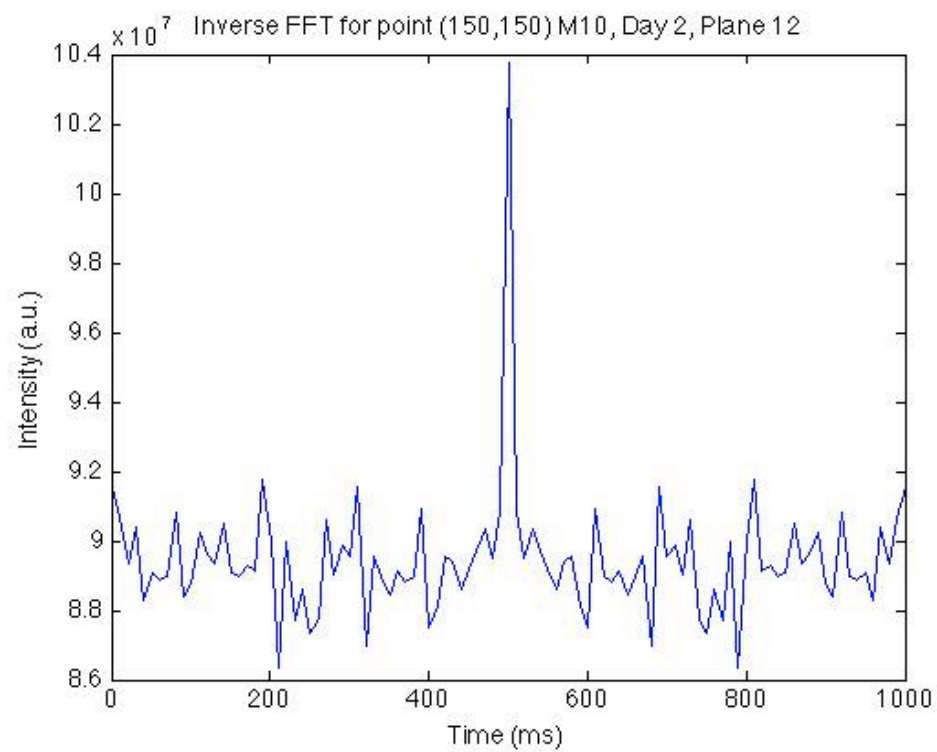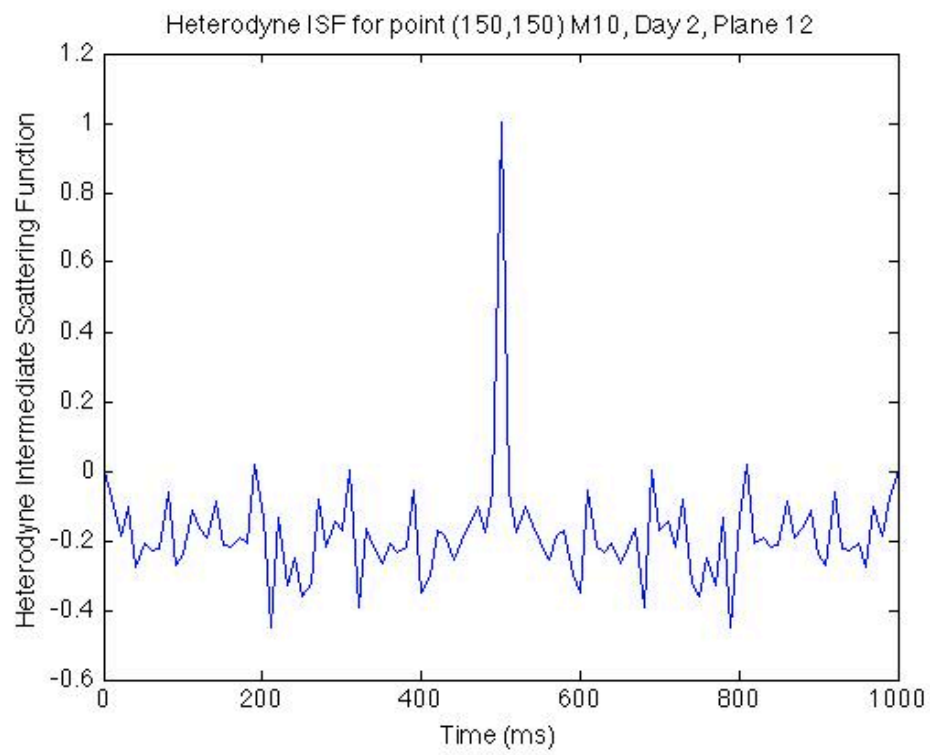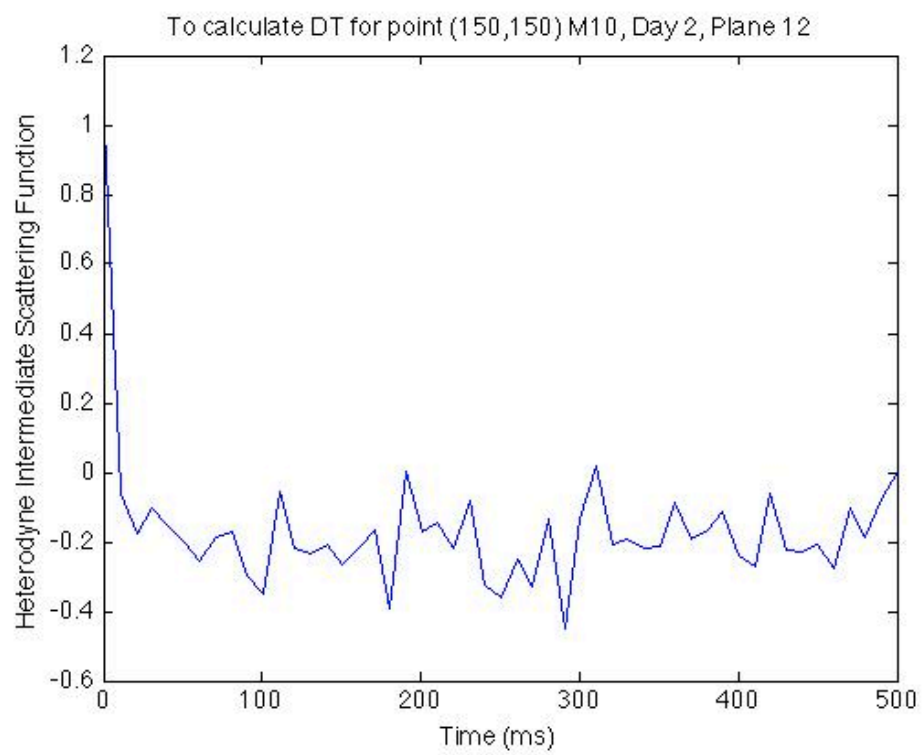
Figure 4-4: (a) The fluctuations in signal intensity for point (150, 150) across multiple OCT timeframes for Mouse 10; (b) The power spectrum of the pixel intensities in (a); (c) The inverse Fourier transform of the power spectrum in (b); (d) The heterodyne intermediate scattering function produced using the Joosten algorithm [45]; (e) The resulting curve used to choose the DT value (the decorrelation time is the time chosen when the heterodyne ISF drops below the value of 1/e).

Figure 4-3 and 4-4 show the fluctuations in signal intensity for a pixel corresponding to frame 101 to 200 of the specific imaging plane. Only 100 frames were chosen to perform the decorrelation algorithm quickly. The same algorithm can be repeated for other sections of the 1000 frames to compare the DT of the same pixel over time. Table 4-1 shows the DT measured for Mouse 2 (control) and Mouse 6 (treated) on Day 1 for 10 sections of the 1000 frames of data. Two pixels were chosen, where one was at a location suspected for longer DT and the other at a location suspected for shorter DT.

Table 4-1: Decorrelation times taken at a long DT pixel and short DT pixel for Mouse 2 and Mouse 6 over ten 100-frame sections.

Mouse 2 (control)			Mouse 6 (cisplatin treated)		
Frames	Long DT at Point (143, 240) in ms	Short DT at Point (143, 230) in ms	Frames	Long DT at Point (128, 154) in ms	Short DT at Point (150, 150) in ms
1-100	177.8	20	1-100	60	20
101-200	175.6	20	101-200	86.67	20
201-300	166.7	20	201-300	66.67	20
301-400	155.6	20	301-400	51.11	20
401-500	128.9	20	401-500	64.44	20
501-600	140	20	501-600	26.67	20
601-700	91.11	20	601-700	60	20
701-800	140	20	701-800	64.44	20
801-900	135.6	20	801-900	24.44	20
901-1000	148.9	22.22	901-1000	53.33	20
Mean	146.0	20.2	Mean	55.78	20
Std. Dev.	25.61	0.70	Std. Dev.	18.61	0

The data in Table 4-1 shows that the DT at a pixel location indicative of long or short DT remains long or short throughout the whole 1000 frames. There are slight changes for

pixels with longer DT, but pixels with shorter DT remained the same for most of the pixels. This short DT of 20 ms was at the lowest possible DT value measured with the system. This pattern was observed for other pixel locations in all the mice in this study.

4.1.3 Histology Images
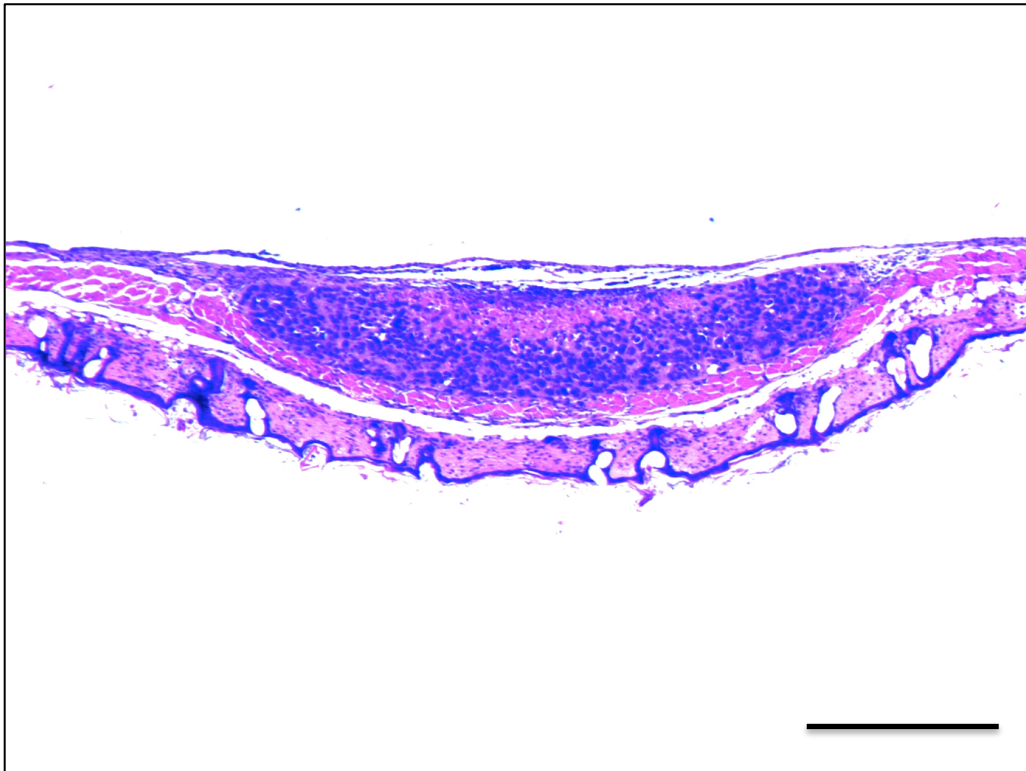
(a)
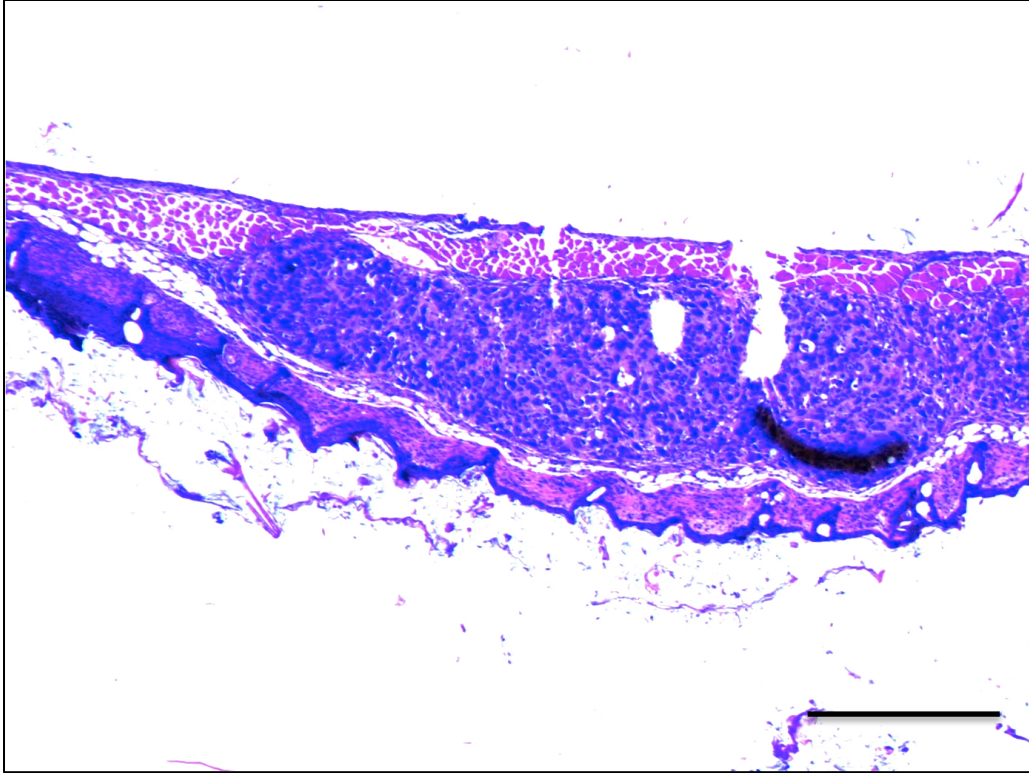
(b)

Figure 4-5: An example hematoxylin and eosin staining of the tumour imaged with 4x microscope objective for (a) Mouse 6 and (b) Mouse 10. The scale bar is 500 μm.

Figures 4-5a and 4-5b show examples of H&E stained images of a tumour tissue sample for Mouse 6 and 10, respectively. The tumour cells were implanted into the fascia of the subcutaneous tissue on the inside of the mouse dorsal skin. The glass window for the window chamber was placed on top of the subcutaneous tissue, thus resulting in a flat top surface for the tumour tissue sample. The H&E staining showed that the tissue sample contained tumour cells apart from the skin cell morphology. Further histology analysis is described later in this chapter.

4.2 Flow Segmentation

The previous *in vivo* feasibility study by Farhat et al. included observations of areas with short DT, with the recognition that these areas are possible blood vessel locations [12]. Since the motion due to cell death is of interest in this thesis, the pixels for the locations of blood vessels should not be taken into account in the analysis. The analysis presented in this thesis will segment the locations of vessels assuming that areas of short DT correspond to potential locations of blood vessels. In order to measure an average DT value of a specific region of interest (ROI) that includes tumour tissue only (and not blood vessels), it was necessary to segment out pixels containing blood vessels as indicated by short DT values and/or the presence of shadows. The term "average DT" refers to the average of all the DT values within a selected ROI. A thresholding method was applied to the DT map in order to remove what we postulate are vessel flow contributions in the average DT calculations.

To obtain a suitable threshold value for flow segmentation, the DT value of tumour cells must be known. Previous *in vitro* studies have shown that the DT value for cells in cell aggregates emulating tumours range from 100 to 300 ms (Figure 2-7) [11]. In addition, speckle variance uses techniques similar to the ones used in this study to produce images of the vasculature and it is known that blood vessels cast a shadow in speckle variance measurements of the vasculature. This shadowing effect has been attributed to multiple scattering effects [49]. Therefore, there is strong evidence that short DT regions correspond to motion due to the presence of the flowing blood in blood vessels.

(a)

(b)
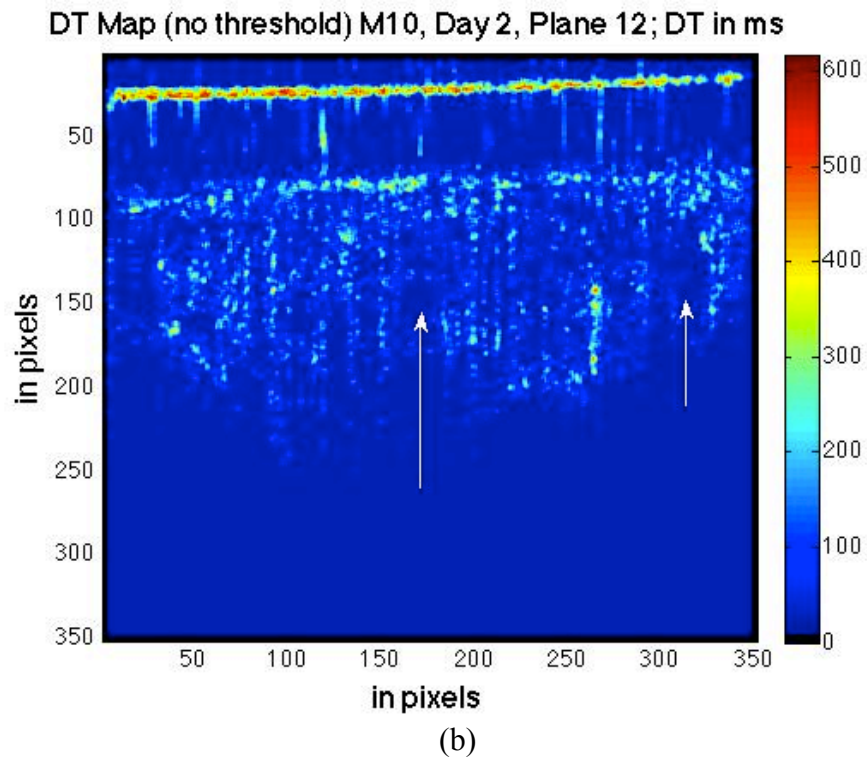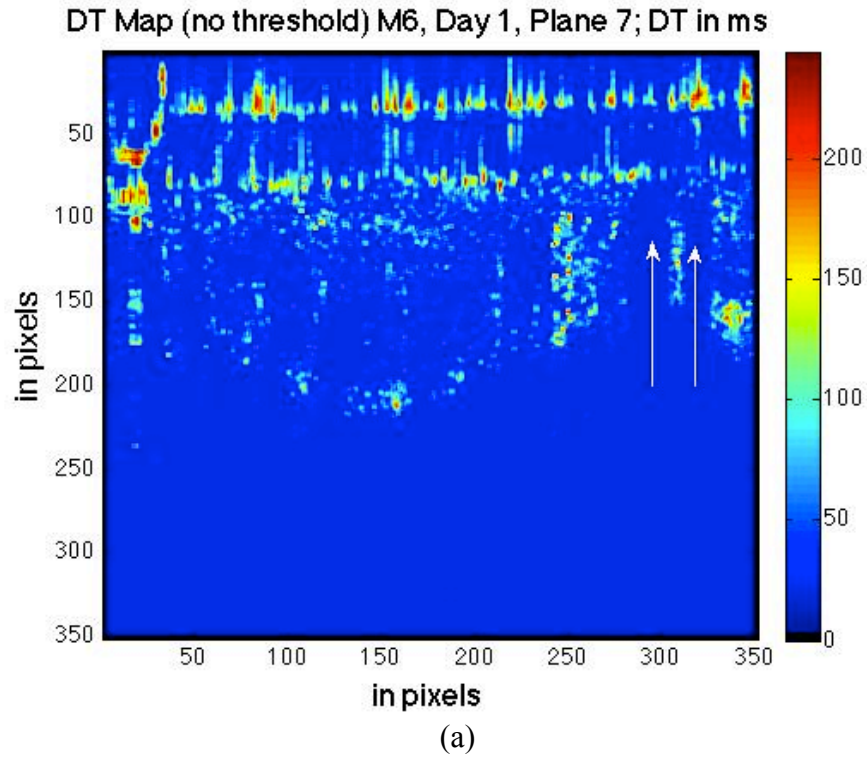
Figure 4-6: DT map (without threshold) of tumour of (a) Plane 7 of Mouse 6 on Day 1 and (b) Plane 12 of Mouse 10 on Day 2. The white arrows point out suspected blood

vessel locations and their shadowing effect. The image height and image width are both 3 mm.

Three approaches were used to determine the most suitable threshold DT value to exclude pixels corresponding to the location of blood vessels from the analysis of tissue response. The first method involved comparing the actual DT pixel values in the pre-threshold DT maps with existing data from previous studies. Figures 4-6a and 4-6b show the pre-threshold DT maps of imaging plane 7 for Mouse 6 on Day 1 and imaging plane 12 for Mouse 10 on Day 2, respectively. For both DT maps, the tumour growth was observed near the centre of the DT map. The longest and shortest DT values measured were 617 and 20 ms, respectively. Areas of short DT were observed to the right of the tumour for Mouse 6 and are indicated by the white arrows. Similarly, white arrows at the centre and right side of the tumour indicate short DT regions for Mouse 10. Some of these areas of short DT have a symmetrical shape and cast a streaking or shadowing effect (more pronounced in Figure 4-6a than Figure 4-6b) indicating the vessel locations. In Figure 4-6, the specific DT values at the shadowed areas ranged from 20 to 30 milliseconds. This observation is consistent with the observation of the short DT times measured *in vitro*; motion caused by flow will have much shorter DT than of cells *in vitro* [11]. The other approaches will be described in the two following sections regarding the quantitative analysis of average DT variations between possible threshold values (Section 4.2.1) and the qualitative analysis of the DT map background (Section 4.2.2), respectively.

4.2.1 Quantitative Analysis of Thresholding

49

A quantitative assessment to establish the most suitable value for thresholding all DT maps was performed. A threshold value (e.g. DT = 20 ms) and a ROI (e.g. a region in the DT map of size 50 by 30 pixels) were selected for the first assessment. The pixels in the ROI with DT values less than this threshold value were assigned a value of zero so that the pixels could be excluded from further analysis. A pixel count was taken for all nonzero pixels within the ROI. The average of all the remaining nonzero DT values was then calculated. These steps were repeated for other threshold values close to these values (e.g. DT = 30, 40, 50, and 60 ms).
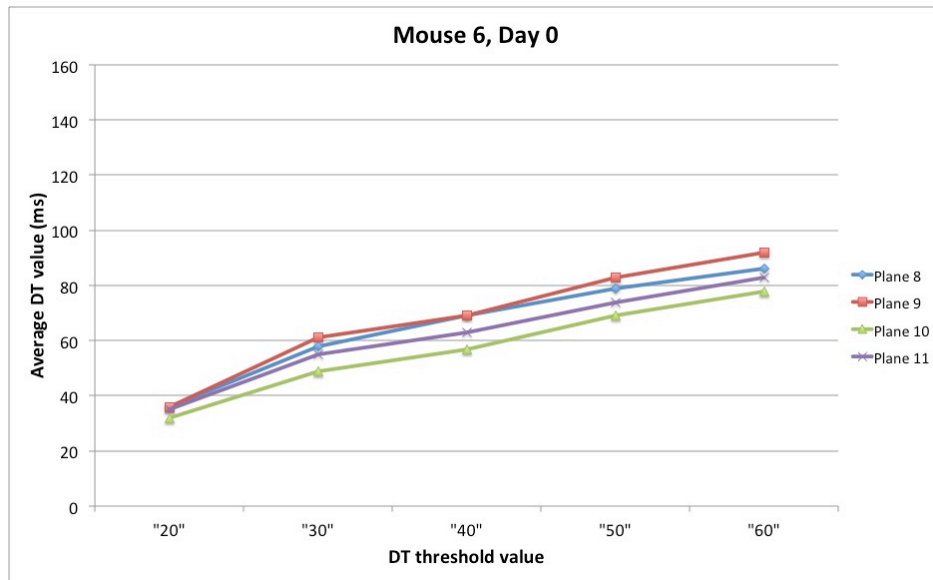
(a)
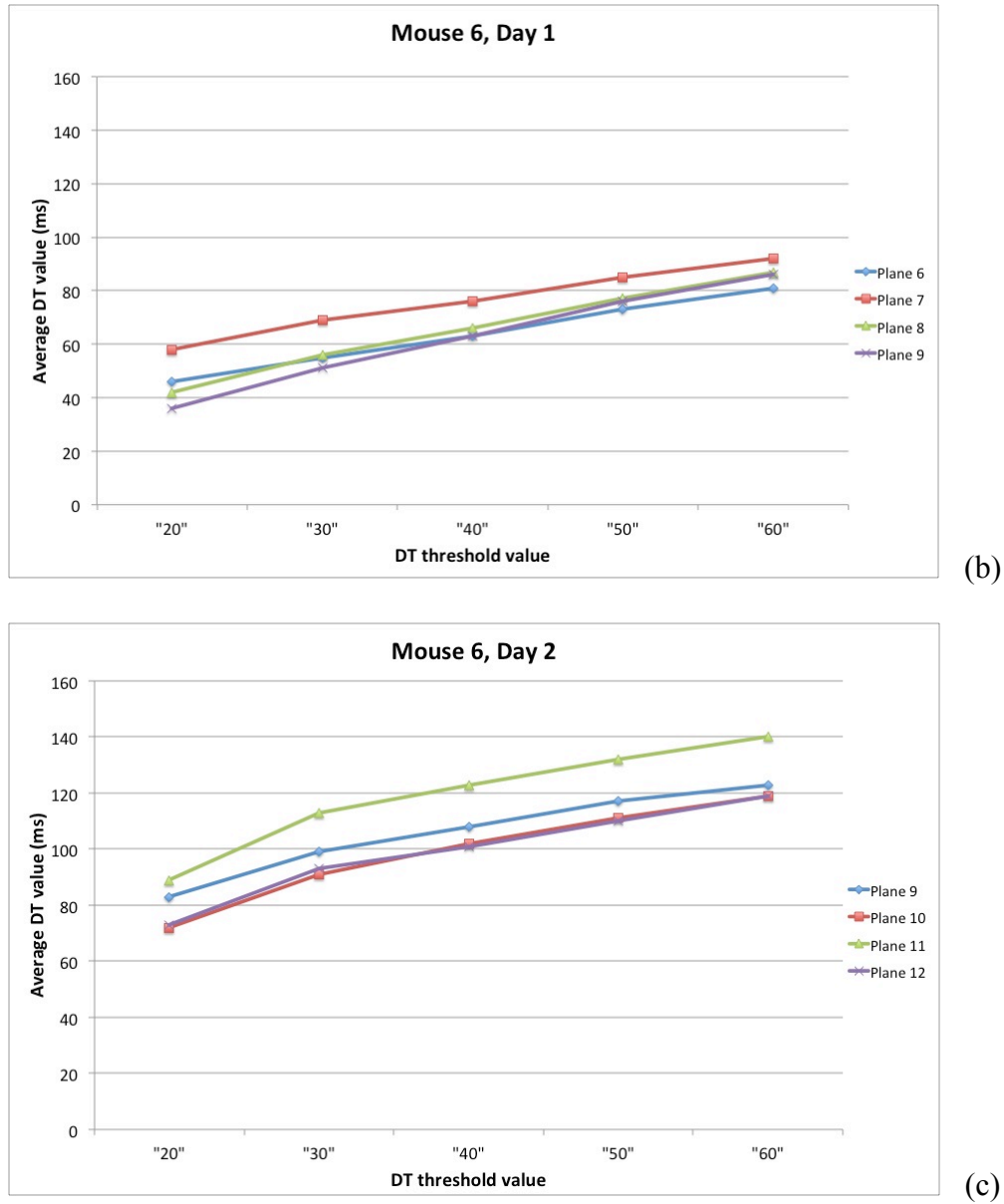
Figure 4-7: Average DT values of different thresholds (20, 30, 40, 50, and 60 ms) for Mouse 6 for (a) Day 0; (b) Day 1; and (c) Day 2.

A ROI of size 50 by 30 pixels was chosen at the centre of the tumour in order to observe the effects of thresholding of vessels within the tumour on the ROI average DT values. Figure 4-7 shows the average tumour DT values as a function of the respective DT thresholds applied. Figure 4-7a shows the average DT values of Mouse 6 on Day 0 for planes 8 to 11, using threshold values of 20, 30, 40, 50, and 60 ms to generate the DT

maps of those imaging planes. This ROI of size 50 by 30 pixels was selected at pixels at the centre of the tumour with a diameter of 1-2 mm. The pixel length and width were both 8.6 μm and were consistent throughout the thesis.

Table 4-2: An excerpt of the chart data corresponding to Figure 4-7 for Mouse 6 from Day 0 to Day 2. Difference refers to the increase in average DT compared to the next longest DT threshold. The maximum pixel count based on the ROI chosen was 1500. See Appendix E for the full summary chart.

	Day 0					Day 1			
Plane	Thres	Avg DT	Diff	PixelCount	Plane	Thres	Avg DT	Diff	PixelCount
8	20	36	22	1500 (100%)	6	20	46	9	1500 (100%)
	30	58	11	582 (38.8%)		30	55	8	1065 (71.0%)
	40	69	10	401 (26.7%)		40	63	10	769 (53.6%)
	50	79	7	290 (19.3%)		50	73	8	504 (33.6%)
	60	86		223 (14.9%)		60	81		350 (23.3%)
9	20	36	25	1500 (100%)	7	20	58	11	1500 (100%)
	30	61	8	555 (37.0%)		30	69	7	1125 (75.0%)
	40	69	14	428 (28.5%)		40	76	9	939 (62.6%)
	50	83	9	280 (18.7%)		50	85	7	741 (49.4%)
	60	92		211 (14.1%)		60	92		596 (39.7%)

Table 4-2 contains a summary of the raw data used to plot the graphs in Figure 4-7. It was observed for all imaging planes that 1500 nonzero pixels (which was the maximum number of pixels within the ROI of 50 x 30 pixels) were counted when threshold of 20 ms was applied, thus indicating that all the pixels in the ROI had DT greater than 20 ms. Therefore, the threshold of 20 ms was not suitable in segmenting out any pixels, including short DT pixels suspected as vessel locations.

The graphs in Figure 4-7 illustrate an increase of average DT with the use of a longer DT threshold value. Figures 4-7b and 4-7c plot the same data for a selection of imaging planes for Mouse 6 for Day 1 and Day 2, respectively. For many of the imaging planes, the most significant change in the average DT values between thresholds within each imaging plane was from changing the threshold from 20 to 30 ms. This observation

was made by noting the different slopes of the line graphs between points, as well as by the pixel count for the ROI at each threshold, as indicated in Table 4-2. The differences between the average DT values of adjacent thresholds were also calculated to show the increase of average DT from threshold to threshold. The results from observing these differences showed the greatest average DT increase between 20 to 30 ms for most of the imaging planes, compared to the average DT increases from thresholds 30 to 40 ms, 40 to 50 ms, and 50 to 60 ms. Appendix E has the full summary chart.

(a)

(b)

53
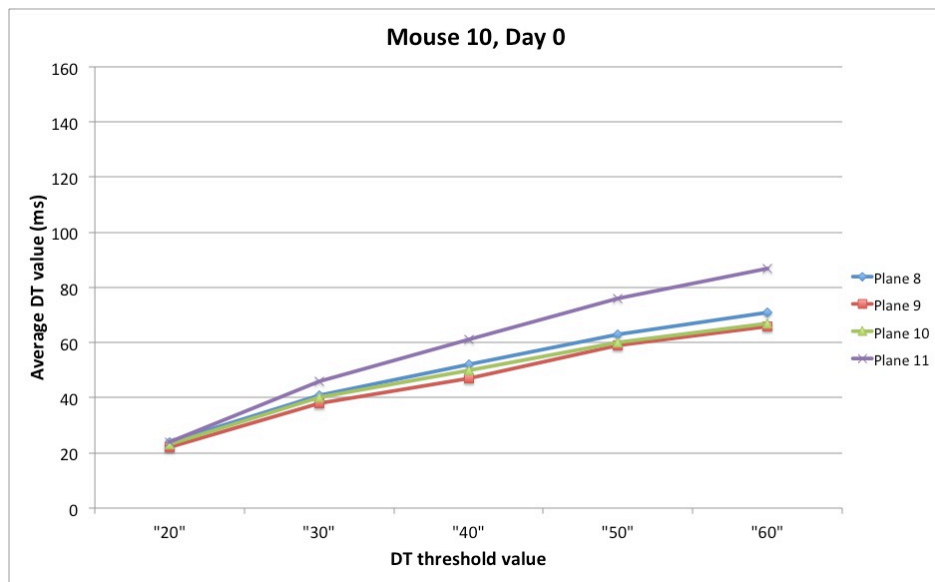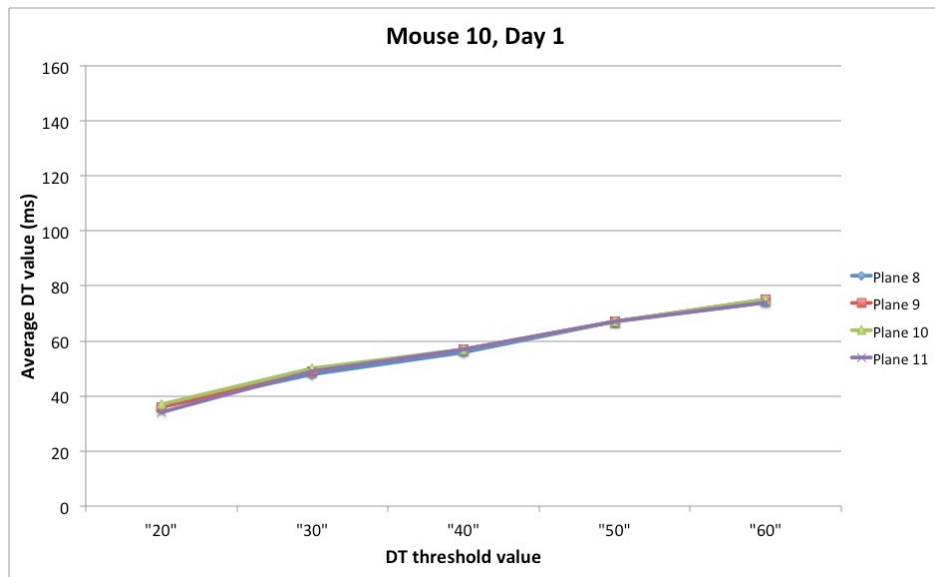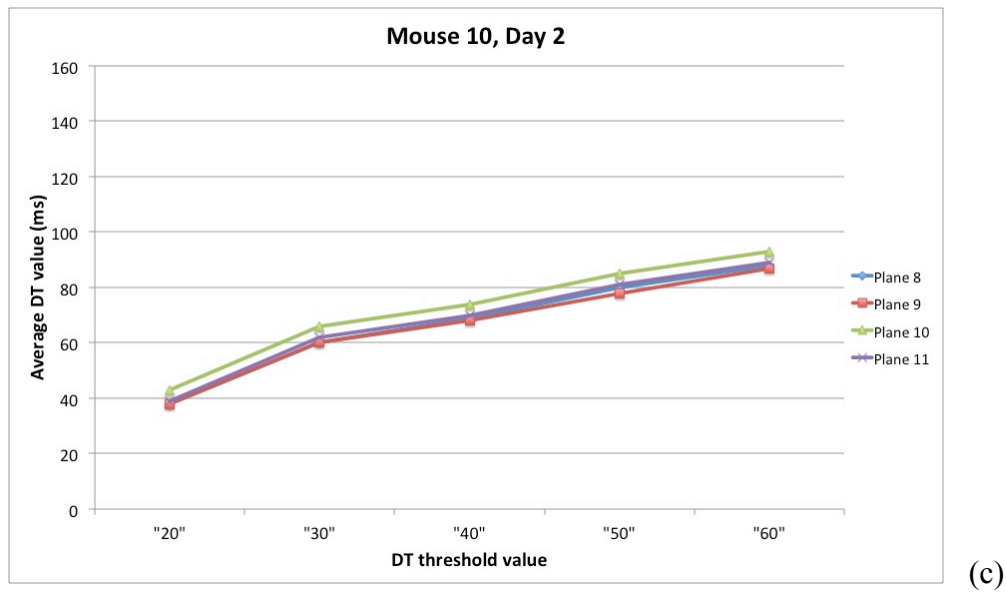
Figure 4-8: Average DT values of different thresholds (20, 30, 40, 50, and 60 ms) for Mouse 10 for (a) Day 0; (b) Day 1; and (c) Day 2.

This process of thresholding was repeated for all the mice in the study to examine the effect of picking different thresholds on the average DT values. The line graphs for Day 0 to Day 2 for Mouse 10 are shown in Figures 4-8a to 8c. A larger ROI of 9000 pixels (which was the maximum number of pixels within the ROI of 150 x 60 pixels) was chosen to cover a larger tumour region for Mouse 10 than Mouse 6. The same pattern observed for Mouse 6 in Figures 4-7a to 4-7c was seen in Mouse 10, including the increase of average DT for longer DT threshold values, with the greatest variation between thresholds of 20 and 30 ms.

Table 4-3: An excerpt of the chart data corresponding to Figure 4-8 for Mouse 10 from Day 0 to Day 2. Difference refers to the increase in average DT compared to the next longest DT threshold. The maximum pixel count based on the ROI chosen was 9000. See Appendix E for the full summary chart.

	Day 0					Day 1			
Plane	Thres	Avg DT	Diff	PixelCount	Plane	Thres	Avg DT	Diff	PixelCount
10	20	23	17	9000 (100%)	10	20	37	13	9000 (100%)
	30	40	10	852 (9.47%)		30	50	7	4709 (52.3%)
	40	50	10	308 (3.42%)		40	57	10	3165 (35.2%)
	50	60	7	116 (1.23%)		50	67	8	1804 (20.0%)
	60	67		54 (0.60%)		60	75		1095 (12.2%)
11	20	24	22	9000 (100%)	11	20	34	15	9000 (100%)
	30	46	15	1003 (11.14%)		30	49	8	4066 (45.2%)
	40	61	15	442 (4.91%)		40	57	10	2636 (29.3%)
	50	76	11	238 (2.64%)		50	67	7	1528 (17.0%)
	60	87		161 (1.79%)		60	74		976 (10.8%)

Table 4-3 shows the summary chart of all the average DT values for all thresholds used for Mouse 10, as well as the respective pixel counts of the ROI used. See Appendix E for the full summary chart. The differences between the average DT of neighbouring thresholds were also recorded to indicate the extent of the average DT increase from threshold to threshold. Similar to the results for Mouse 6, the average DT variations between thresholds of 20 to 30 ms was the greatest for most of the imaging planes. Based on this analysis, the DT threshold value of 30 ms was chosen for segmentation.

4.2.2 Qualitative Analysis of Thresholding

DT Map (threshold of 20 ms) M6, Day 1, Plane 7; DT in ms

(a)
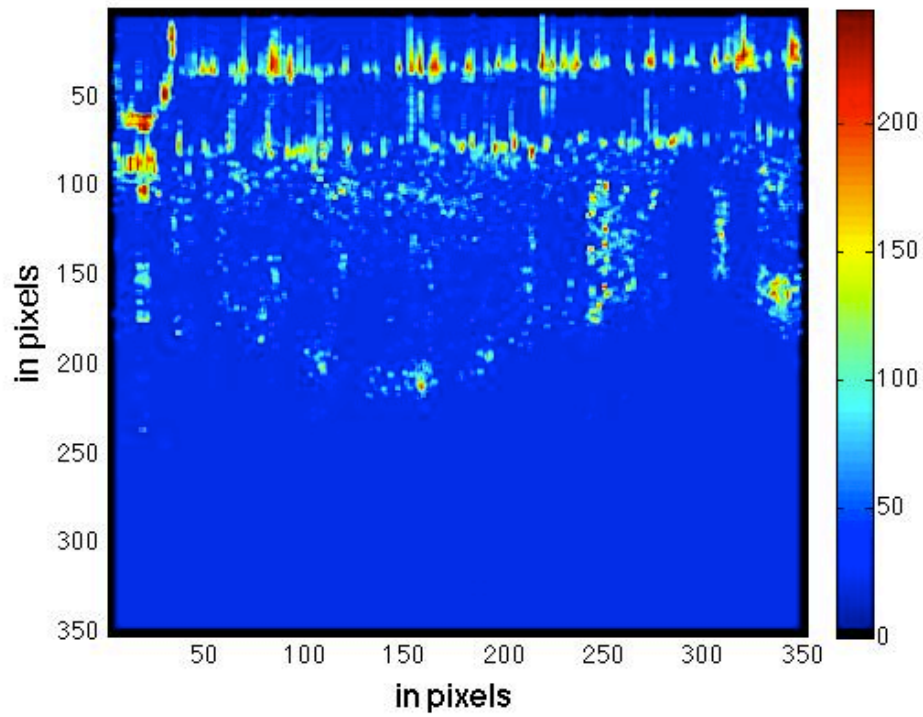
DT Map (threshold of 30 ms) M6, Day 1, Plane 7; DT in ms

(b)
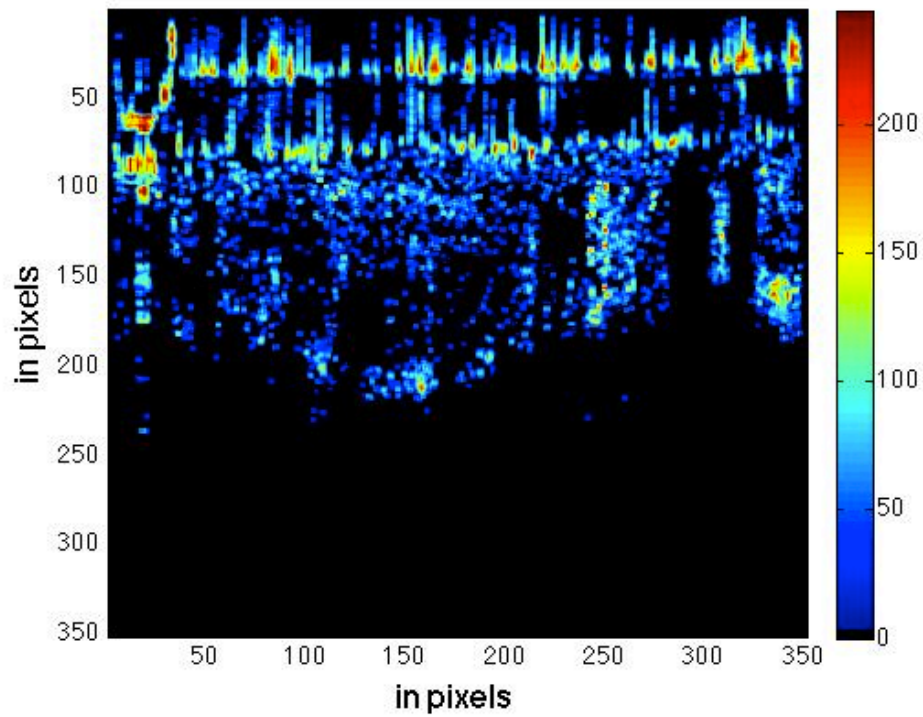
DT Map (threshold of 40 ms) M6, Day 1, Plane 7; DT in ms

in pixels

in pixels

(c)
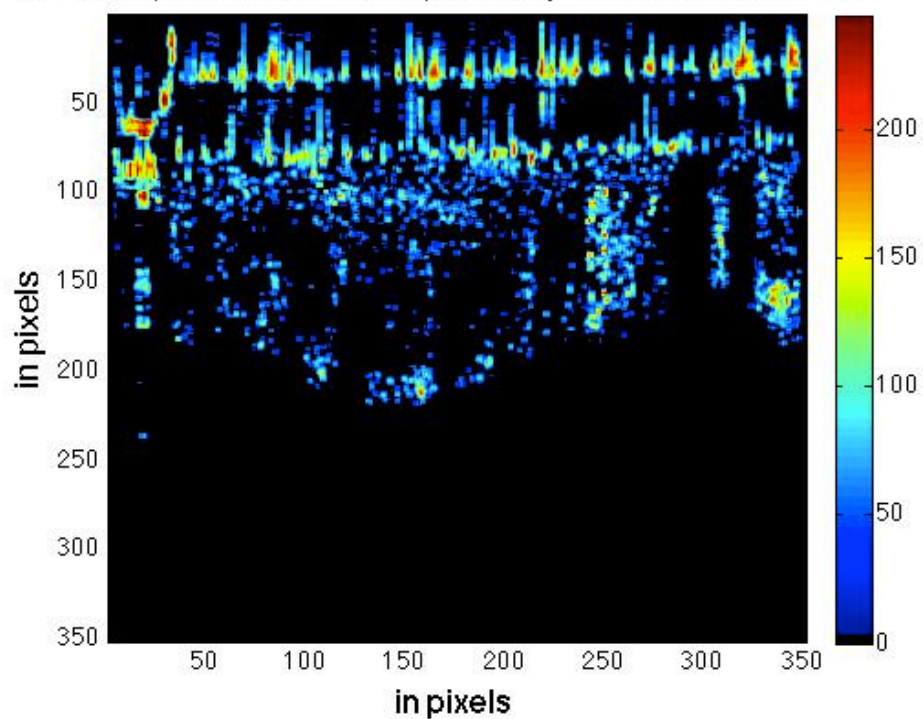
DT Map (threshold of 50 ms) M6, Day 1, Plane 7; DT in ms

in pixels

in pixels

(d)

DT Map (threshold of 60 ms) M6, Day 1, Plane 7; DT in ms

(e)
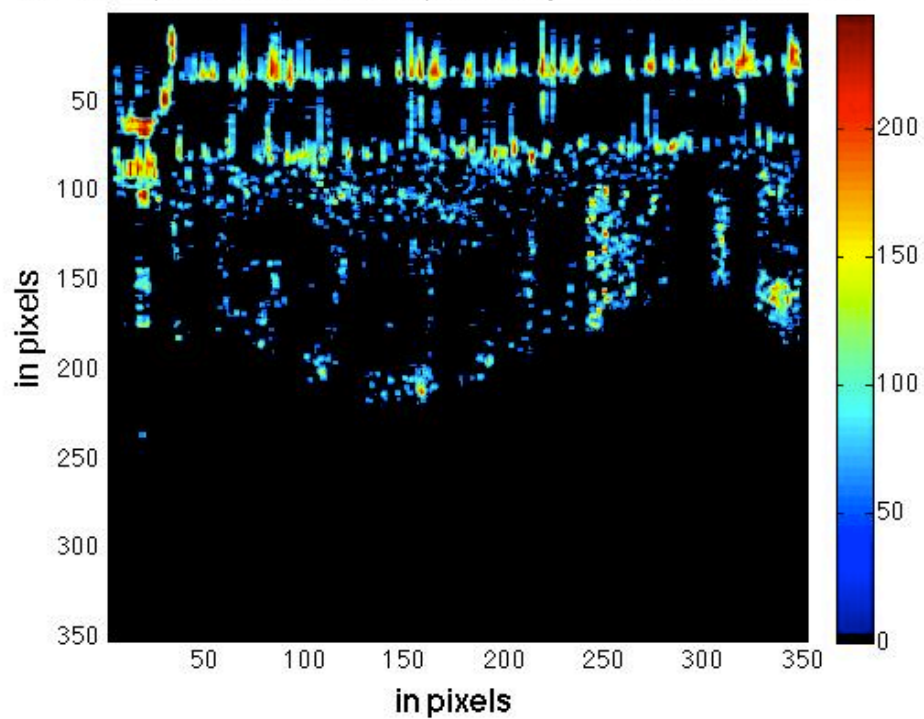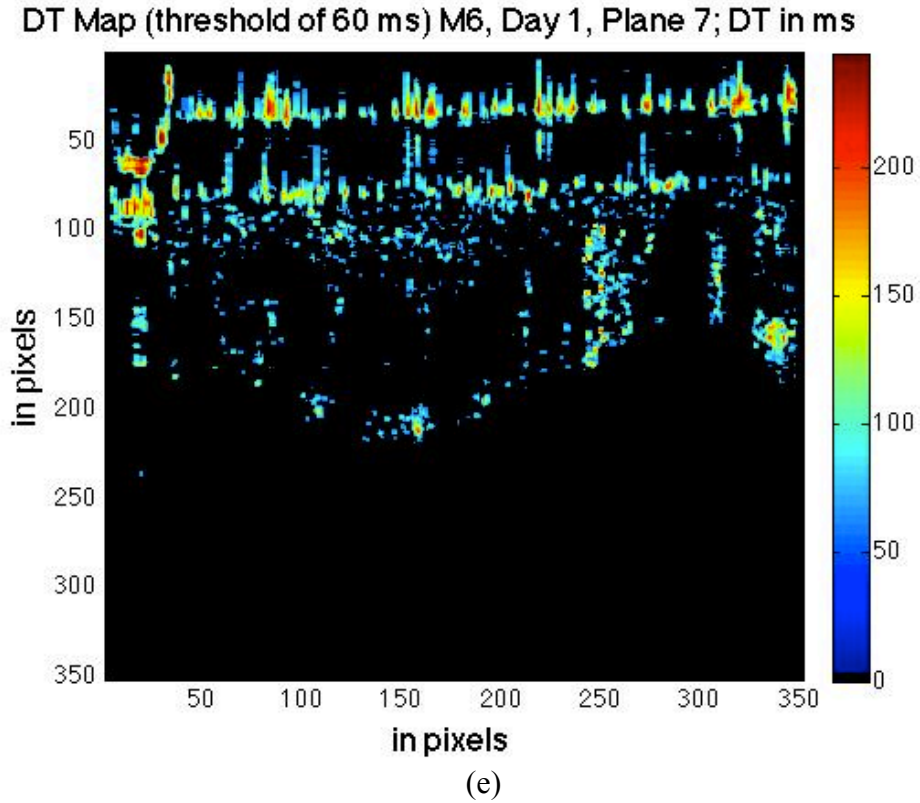
Figure 4-9: (a) DT maps for Mouse 6, Day 1, Plane 7 with a threshold of 20 ms; (b) threshold of 30 ms; (c) threshold of 40 ms; (d) threshold of 50 ms; (e) threshold of 60 ms. The image height and image width are both 3 mm for all images.

The third approach used to determine the best suitable threshold value involved the qualitative assessment of the background in the DT maps. The thresholding algorithm used in the previous analysis involved zeroing all pixels in the selected ROI that were below the selected threshold value. Figures 4-9a to 4-9e illustrate the DT maps with threshold values of 20, 30, 40, 50, and 60 ms for Mouse 6. The ROI for the thresholding algorithm for these DT maps was the entire image (350 by 350 pixels).

DT Map (threshold of 20 ms) M10, Day 2, Plane 12; DT in ms

(a)
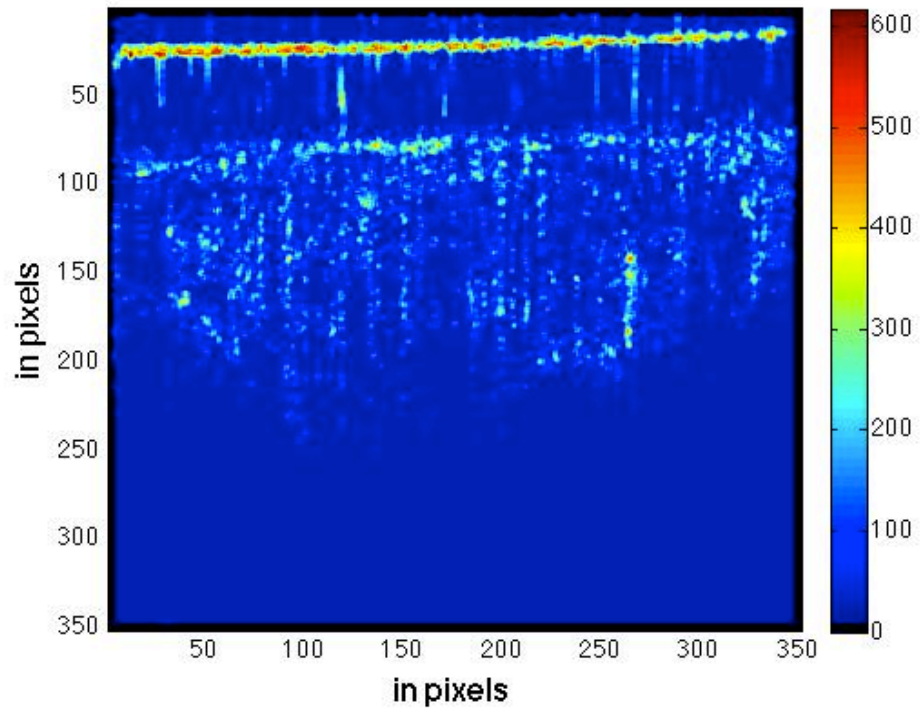
DT Map (threshold of 30 ms) M10, Day 2, Plane 12; DT in ms

(b)
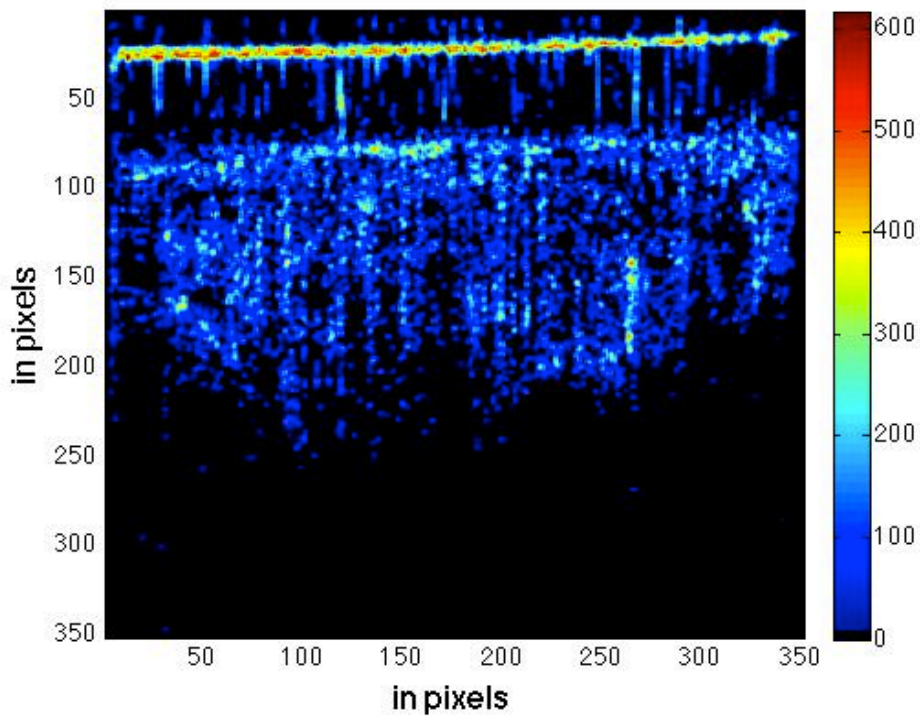
DT Map (threshold of 40 ms) M10, Day 2, Plane 12; DT in ms

(c)
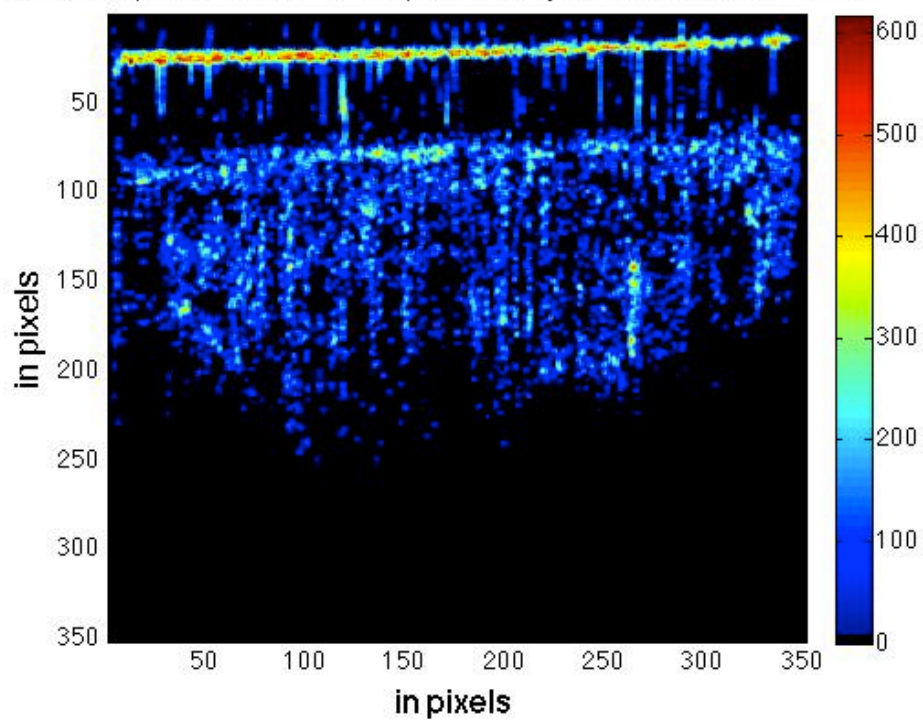
DT Map (threshold of 50 ms) M10, Day 2, Plane 12; DT in ms

(d)

DT Map (threshold of 60 ms) M10, Day 2, Plane 12; DT in ms

(e)
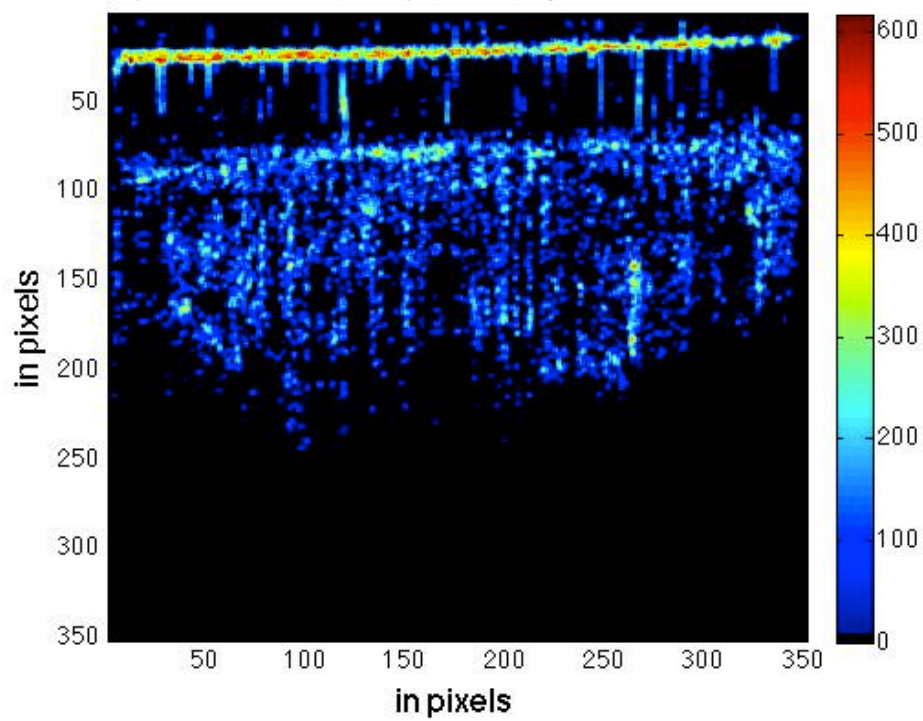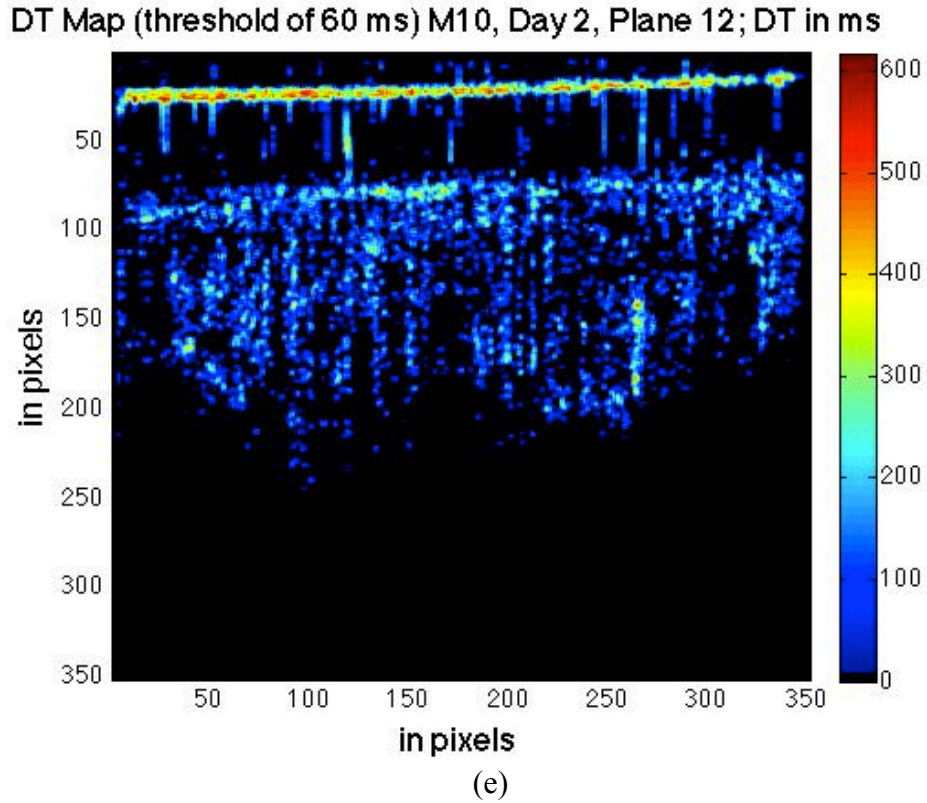
Figure 4-10: (a) DT maps for Mouse 10, Day 2, Plane 12 with a threshold of 20 ms; (b) threshold of 30 ms; (c) threshold of 40 ms; (d) threshold of 50 ms; (e) threshold of 60 ms. The image height and image width are both 3 mm for all images.

With the modified colour map setting, any black pixels observed indicated zeroed pixels for the specific threshold value applied. A distinct colour change in the DT map background was observed for Figure 4-9a (threshold of 20 ms) and Figure 4-9b (threshold of 30 ms). The colour change between Figures 4-9b to 4-9e was less apparent. The pixels that changed to black correlated to areas of blood vessels, whereas the pixels that did not change to black correlated to non-vessel locations of DT that was longer than the threshold value. This result showed that a threshold of 30 ms was capable of segmenting out vessel pixels, while preserving non-vessel pixels of longer DT. The same thresholding algorithm was also applied for Mouse 10 and similar DT map results are shown in Figure 4-10. In both cases, using the threshold of 30 ms provided images for

61

which the dark areas were well-defined and predominantly circular areas, as would be expected in the presence of blood vessels. It is not yet known what these pixels represent, but they could represent pixels for which the signal originates predominantly from non-cellular regions (such as the tumour interstitium, lymphatics, etc.) [50]. The elimination of blood vessels with a threshold of 30 ms provides the initial segmentation of pixels due to blood flow, while retaining pixels associated with locations within the tumour interstitium.

The previous *in vitro* study presented tumour cells to have DT values greater than 100 ms [11]. Speckle variance experiments revealed the possibility of blood vessel locations at shadowed areas. By utilizing the previous knowledge, the observations of 1) the actual DT values at pixels with the shadowing effect, 2) average DT variations, and 3) DT map background changes have confirmed the threshold of 30 ms as the best candidate for segmentation. All subsequent results presented in this thesis with thresholding will have a threshold value of 30 ms.

4.3 Decorrelation Time Analysis

Decorrelation time analysis refers to the assessment of average DT values over selected ROIs to determine any suitable trends of DT change as a function of time. The DT analysis involved comparing the average DT values of adjacent imaging planes for different ROIs (as an indication of inter-tumour variability), as well as comparing the average DT values for control and treated mice for different ROIs (as an indicator of tumour response).

DT Map of "tumour" ROI M6, Day 1, Plane 7; DT in ms

(a)
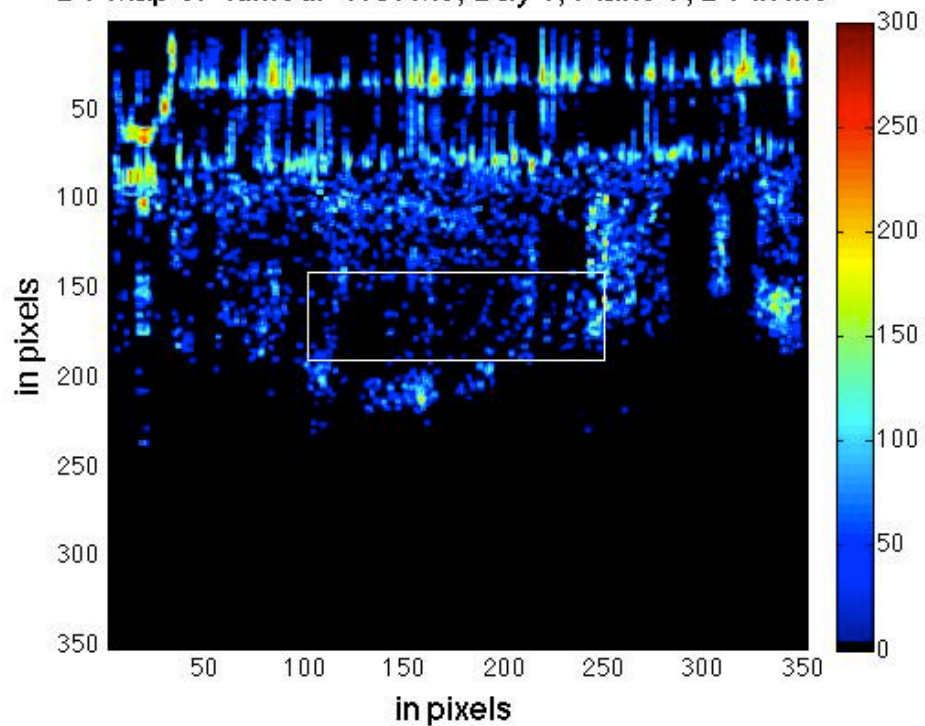
DT Map of "skin" ROI M6, Day 1, Plane 7; DT in ms
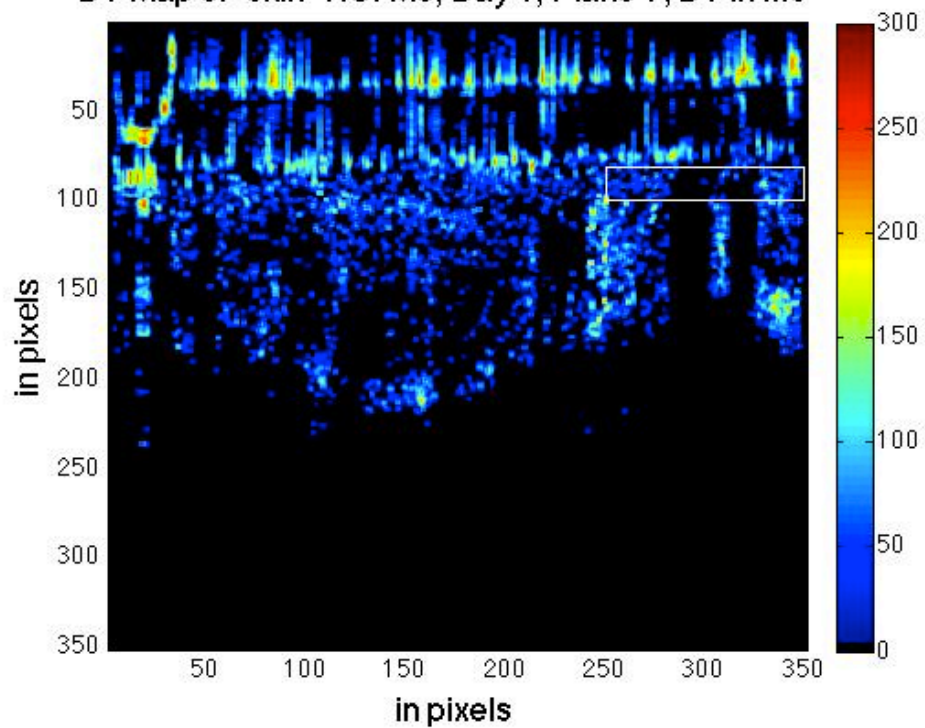
(b)
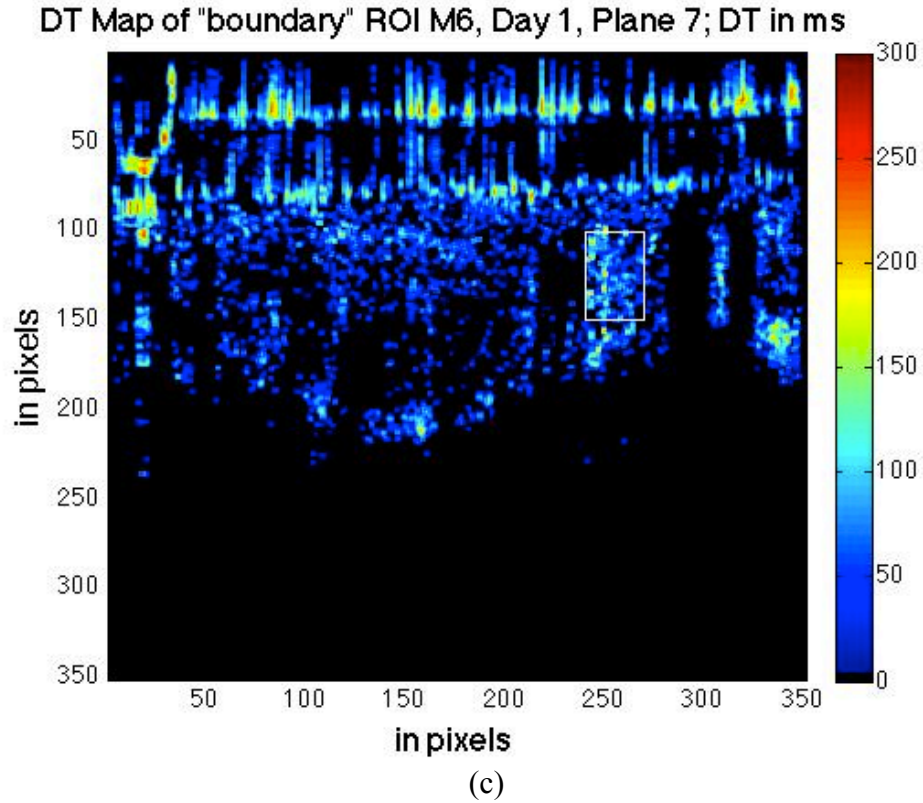
Figure 4-11: DT maps (with threshold of 30 ms) for Mouse 6, Plane 7 on Day 1 with white boxes indicating (a) "tumour" ROI; (b) "skin" ROI; and (c) "boundary" ROI. The image height and image width are both 3 mm for all images.

4.3.1 Decorrelation Time Averages Across Imaging Planes

Due to the proximity of the imaging planes (each plane was separated by 25 μm), it was of interest to map out average DT values for ROIs of adjacent imaging planes to observe the average DT changes throughout the tumour. The average DT values were measured for each of the 26 imaging planes for Mouse 6 for Day 0 to Day 2 with thresholding. Three ROIs were chosen for Mouse 6, and they were labeled as "tumour" (a 60 by 150 pixel ROI near the centre of the tumour), "skin" (a 20 by 100 pixel ROI outside the tumour, near the glass coverslip of the window chamber), and "boundary" (a 50 by 30 pixel ROI at the tumour boundary). Figures 4-11a to 4-11c show the three ROI

locations for plane 7 of Mouse 6 on Day 1. These steps were repeated for plane 12 of

Mouse 10 on Day 2 and are shown in Figures 4-12a to 4-12c.

(a)
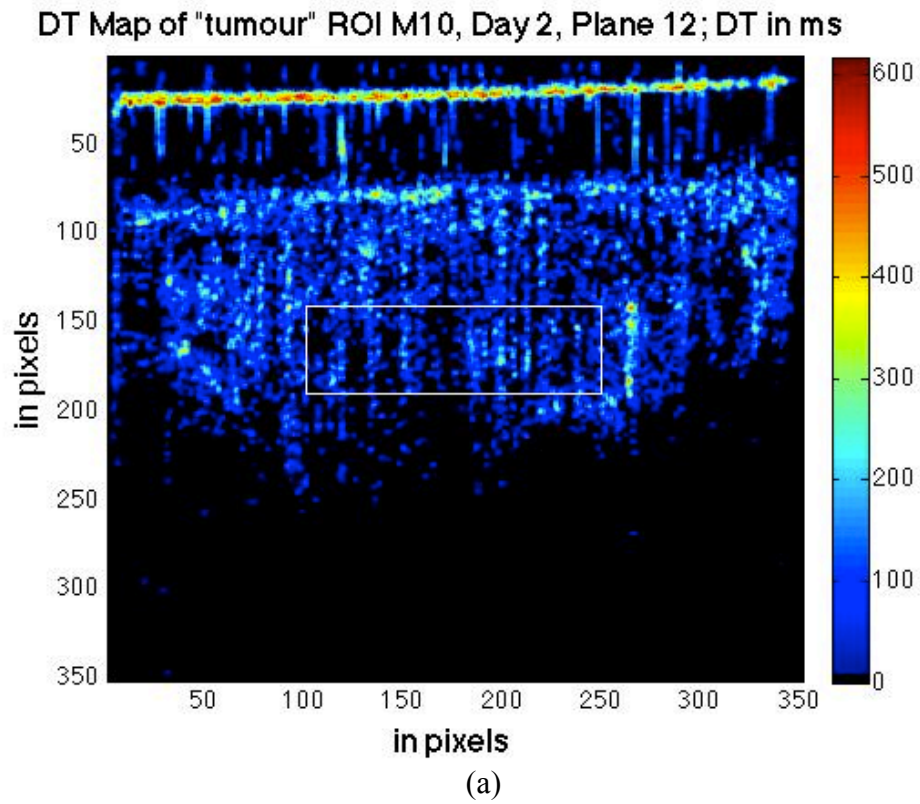
DT Map of "skin" ROI M10, Day 2, Plane 12; DT in ms

in pixels

in pixels
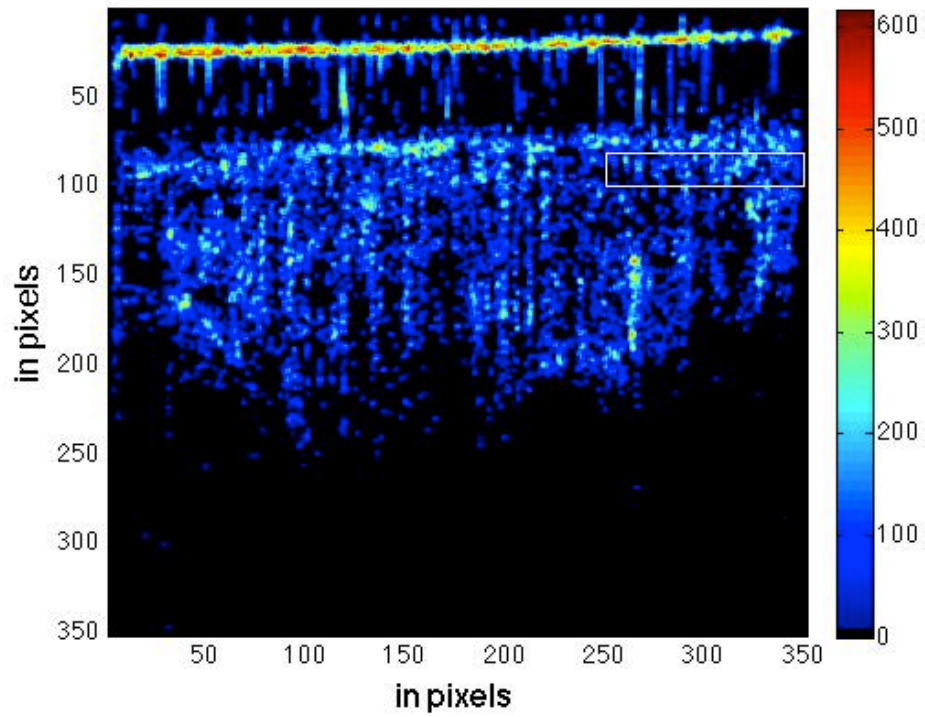
(b)

DT Map of "boundary" ROI M10, Day 2, Plane 12; DT in ms

in pixels

in pixels
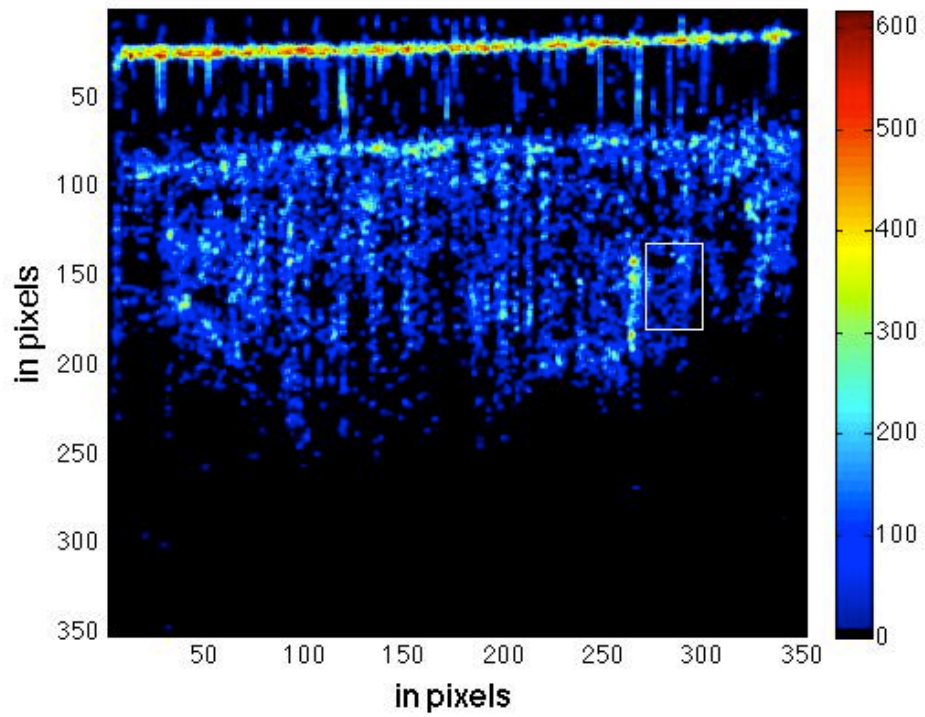
(c)

Figure 4-12: DT maps (with threshold of 30 ms) for Mouse 10, Plane 12 on Day 2 with white boxes indicating (a) "tumour" ROI; (b) "skin" ROI; and (c) "boundary" ROI. The image height and image width are both 3 mm for all images.
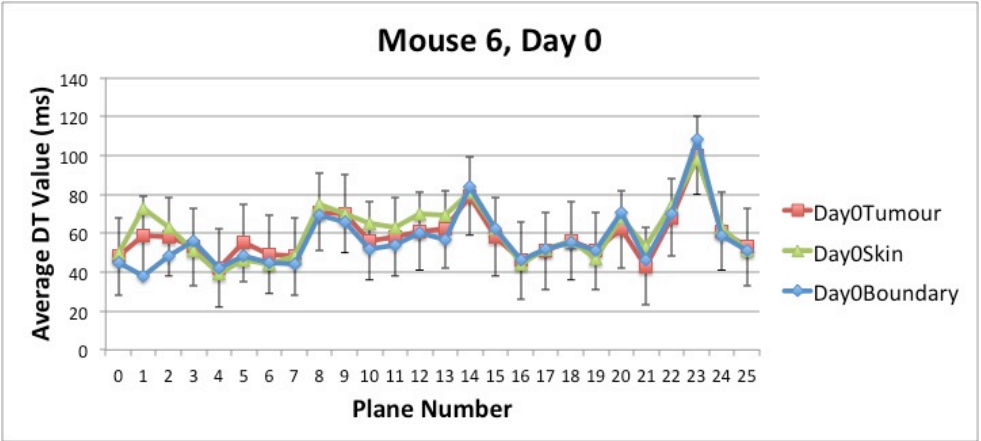
(a)
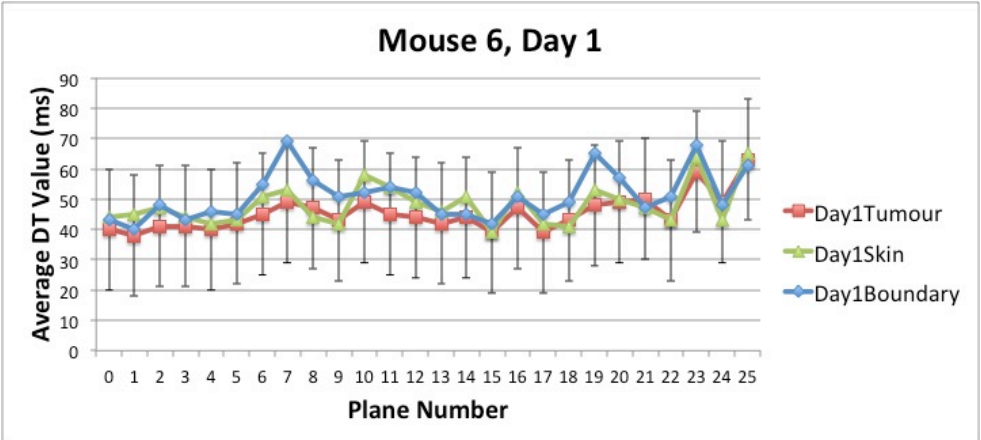
(b)
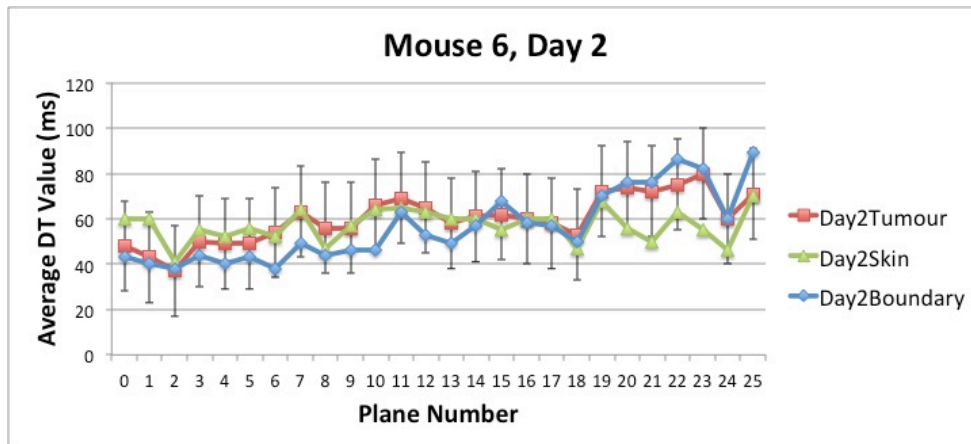
(c)

Figure 4-13: Average DT values of 3 ROIs ("tumour", "skin", and "boundary") across 26 imaging planes for Mouse 6 on (a) Day 0; (b) Day 1; and (c) Day 2. The error bars represent the standard deviation of the "tumour" data set. The standard deviation for the "skin" and "boundary" data sets were similar to the standard deviation for the "tumour" data set, but these error bars are not shown to prevent overlapping error bars.

The resulting average DT values were plotted in Figures 4-13a to 4-13c for Mouse 6 from Day 0 to Day 2. The average DT values showed fluctuations as the ROIs were mapped through the 26 imaging planes (625 μm total distance from plane 0 to 26), indicating that there were changes in the average DT through the different imaging planes. The average DT values for all three ROIs ranged from just under 40 ms to over 100 ms on Day 0, 70 ms on Day 1, and 90 ms on Day 2, as shown in Figures 4-13a to 4-13c. The overlapping of the three lines indicates the similarity of the average DT values for the three ROIs chosen. The data presented showed that the selection of ROIs of different sizes (e.g. when comparing the 9000-pixel "tumour" ROI and the 1500-pixel "boundary" ROI) for the same tumour sample did not show distinct differences between the "tumour" and "boundary" ROIs when mapping the average DT changes across the 625 μm total distance. Another notable observation was the sudden increase or decrease in the DT when compared to the adjacent imaging planes. An example was plane 23 for

68

Day 0 (Figure 4-13a) and Day 1 (Figure 4-13b), where a peak associated with an area of long DT was measured. This location could have been an area not as metabolically active, resulting in less motion and longer DT values.
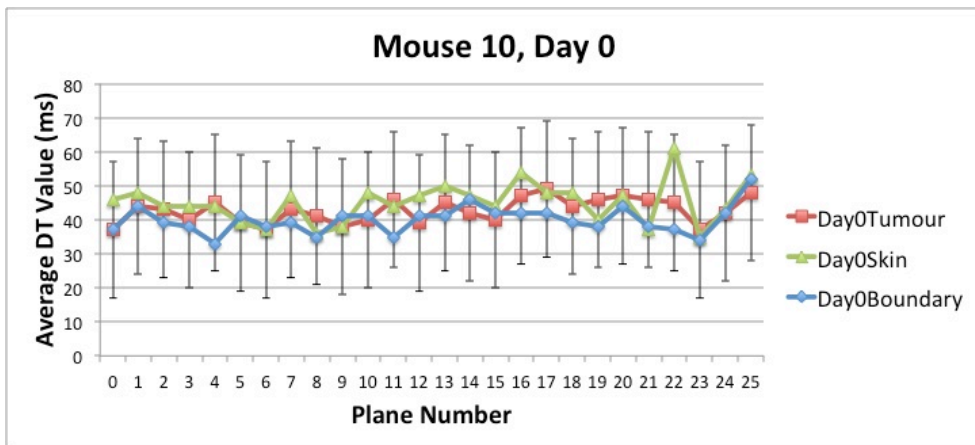
(a)
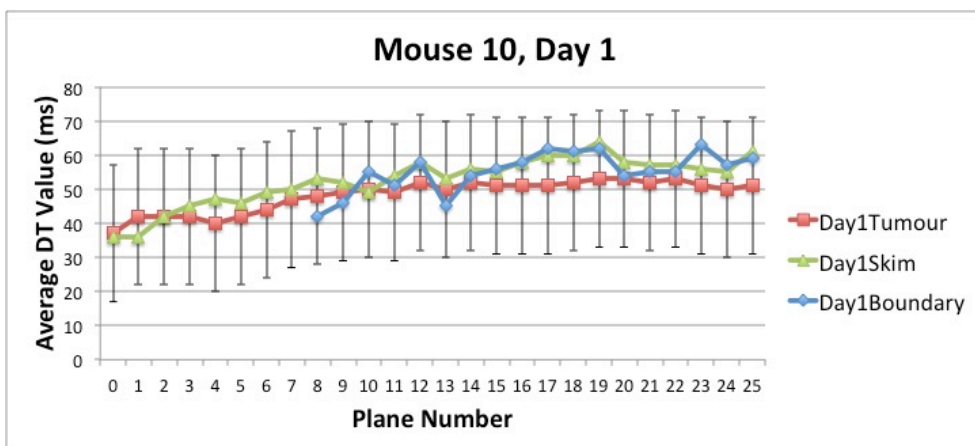
(b)
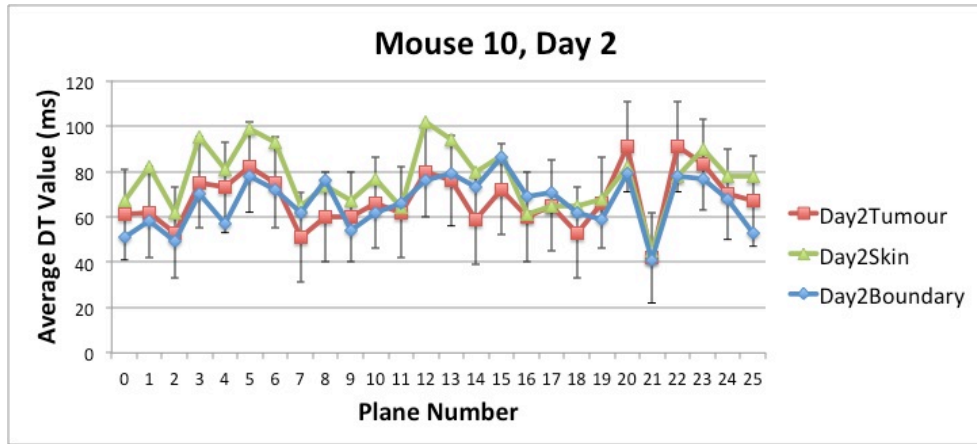
(c)

Figure 4-14: Average DT values of 3 ROIs ("tumour", "skin", and "boundary") across 26 imaging planes for Mouse 10 on (a) Day 0; (b) Day 1; and (c) Day 2. The error bars represent the standard deviation of the "tumour" data set. The standard deviation for the "skin" and "boundary" data sets were similar to the standard deviation for the "tumour" data set, but these error bars are not shown to prevent overlapping error bars.

Figures 4-14a to 4-14c show the average DT values for ROIs for Mouse 10 for Day 0 to Day 2. The data in these three graphs showed similar trends to the data of Mouse 6 in Figures 4-13a to 4-13c, with the range of average DT values from under 40 ms to over 60 ms for Day 0 and Day 1, and over 100 ms for Day 2. Note that in Figure 4-14b for Mouse 10, Day 1, there was no data for the first 8 imaging planes of the boundary ROI. This was due to areas of short DT that were segmented out by the thresholding step, resulting in average DT values of zero. Possible reasons for these areas included a dense network of blood vessels or motion associated with significant tumour cell death. A sudden valley was also detected in plane 21 on Day 2, potentially indicating an area in the tumour having a stronger effect from the cisplatin drug causing motion and shorter DT values.

Similar results were obtained for all other cisplatin-treated mice in this study. The control mice also contained fluctuations in the line graphs. Because no cisplatin was

administered to the control mice, the cause for the increase or decrease of the DT could have been from tumour heterogeneity itself. Areas of a dense network of blood vessels could also have been present in the ROIs chosen, thus yielding results where the DT averaging covered a smaller pixel count. A dense network of blood vessels can cause greater variability due to the smaller number of pixels that contribute to the averaging for the DT measurements. Also, due to the possibility that the imaging voxel (8.6 μm for each side) may contain a mixture of regions with cells and blood vessels, some contributions to the DT from blood vessels may not be segmented, thus resulting in contributions from signals from blood vessels being analyzed. This is possible throughout the whole tumour, but it is more probable in areas with a dense vascular network such as the tumour periphery and skin.

4.3.2 Decorrelation Time Averages for Control and Treated Mice

Table 4-4: The four categories (C1, C2, C3, C4) indicating the ROI selection with or without threshold. The ROI sizes are: large (100 by 200 pixels = 860 μm by 1720 μm) and small (10 by 40 pixels = 86 μm by 344 μm).

	Large ROI	Small ROI
With Threshold	**Category 1 (C1)**	**Category 2 (C2)**
Without Threshold	**Category 3 (C3)**	**Category 4 (C4)**

The average DT was measured to compare control versus treated mice, while varying the ROI size and the application of the thresholding to determine how this would affect the interpretation of the data and conclusions. Four different categories were established to compare the two factors of ROI size and thresholding (outlined in Table 4-4). For all four categories, control (Mouse 1 and 2) and cisplatin-treated (Mouse 5, 6, and

71

10) mice were analyzed. The imaging planes for all four categories are shown in Figures 4-15a to 4-15d for Mouse 6 and Figures 4-16a to 4-16d for Mouse 10. These five mice were chosen since a well-defined tumour could be identified by the supporting H&E histology.

(a)

DT Map of "C2" M6, Day 1, Plane 11; DT in ms

(b)

DT Map of "C3" M6, Day 1, Plane 11; DT in ms

(c)

73
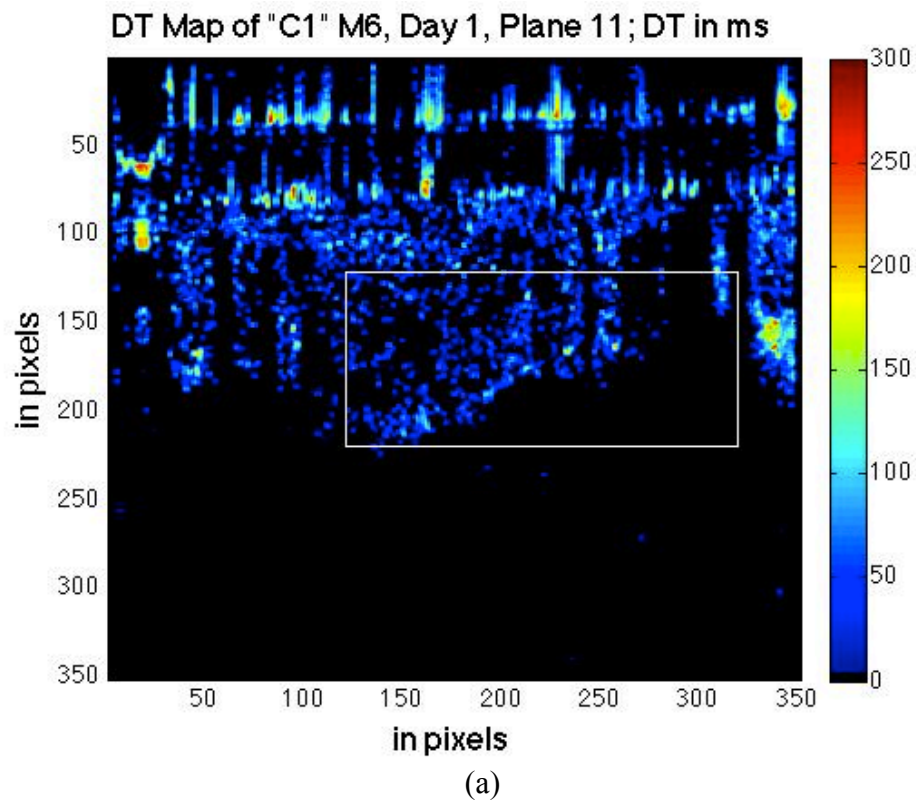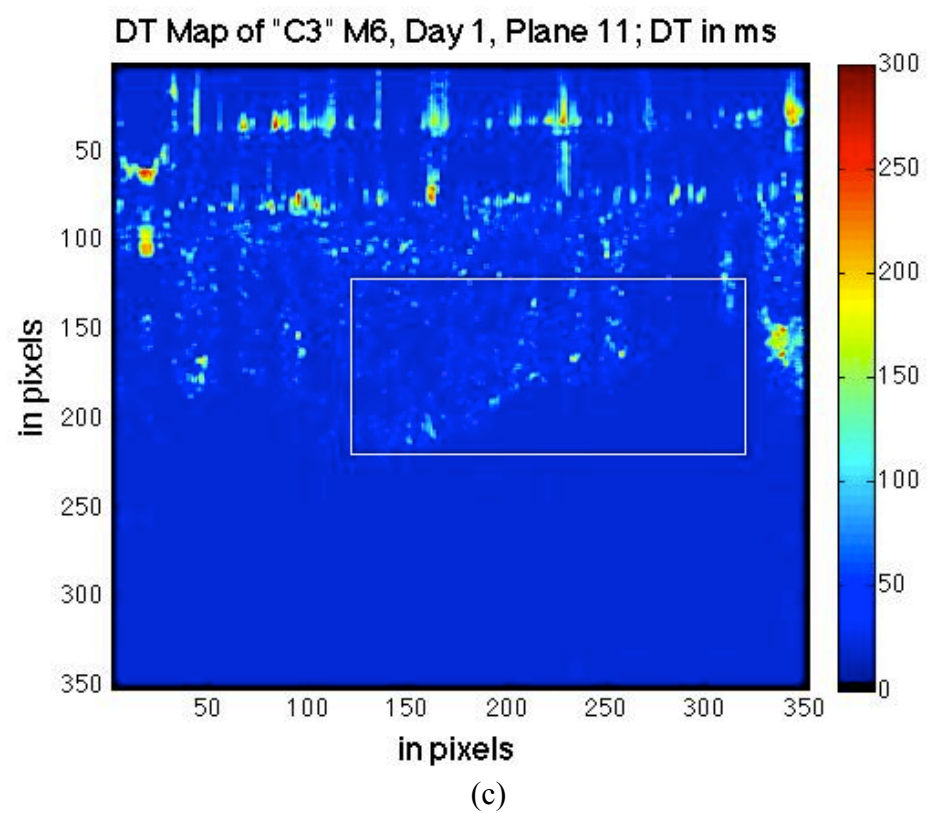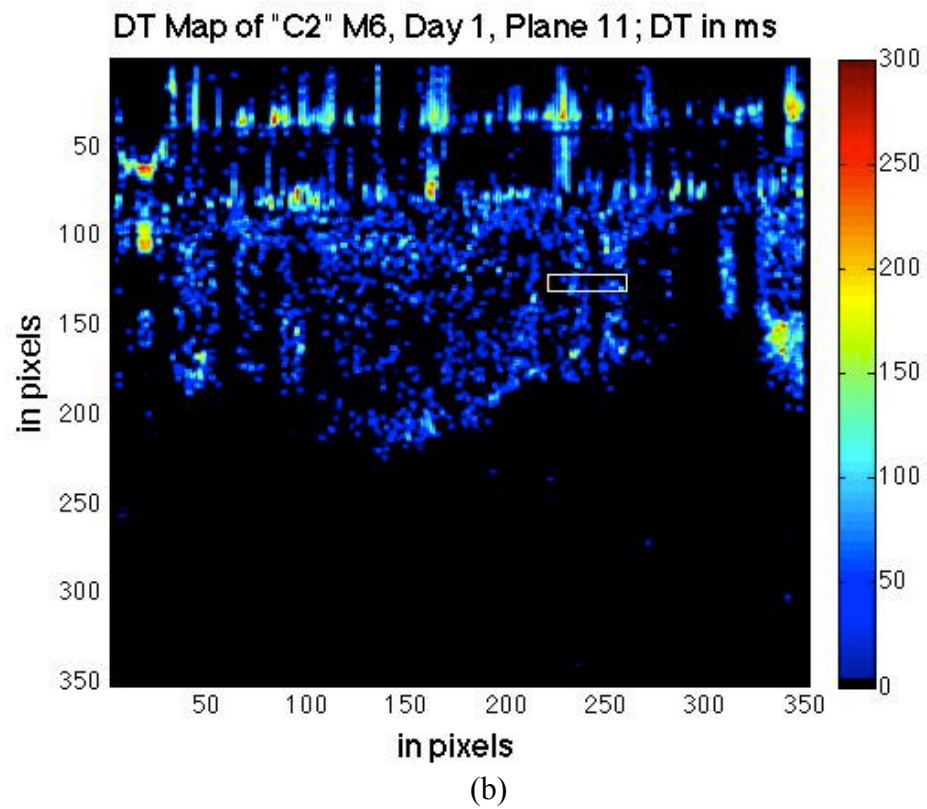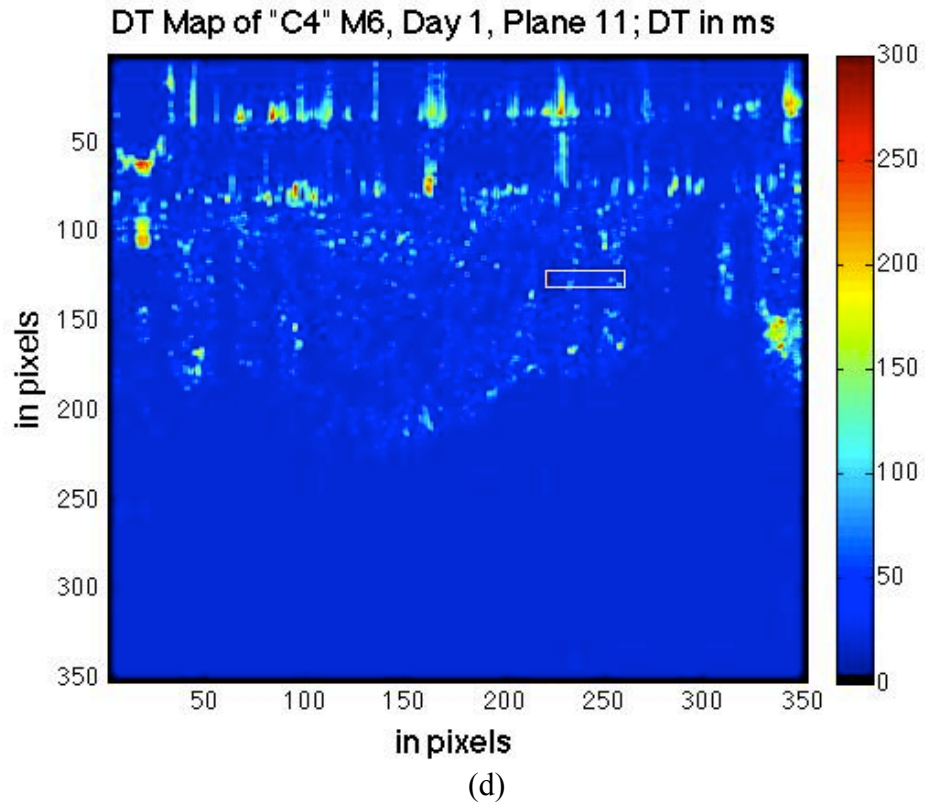
Figure 4-15: DT maps for Mouse 6, Plane 11, on Day 1 correspond to the four categories outlined in Table 4-4: (a) C1; (b) C2; (c) C3; and (d) C4. The image height and image width are both 3 mm for all images.

DT Map of "C1" M10, Day 1, Plane 23 ; DT in ms

(a)

DT Map of "C2" M10, Day 1, Plane 23 ; DT in ms

(b)

DT Map of "C3" M10, Day 1, Plane 23; DT in ms

(c)

DT Map of "C4" M10, Day 1, Plane 23; DT in ms

(d)
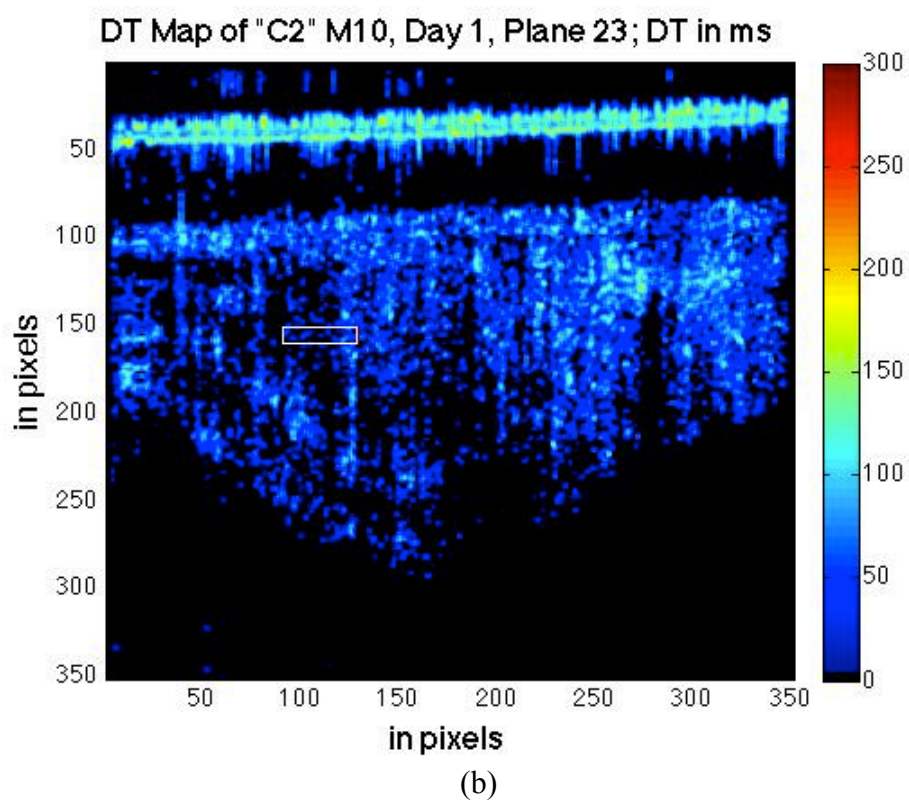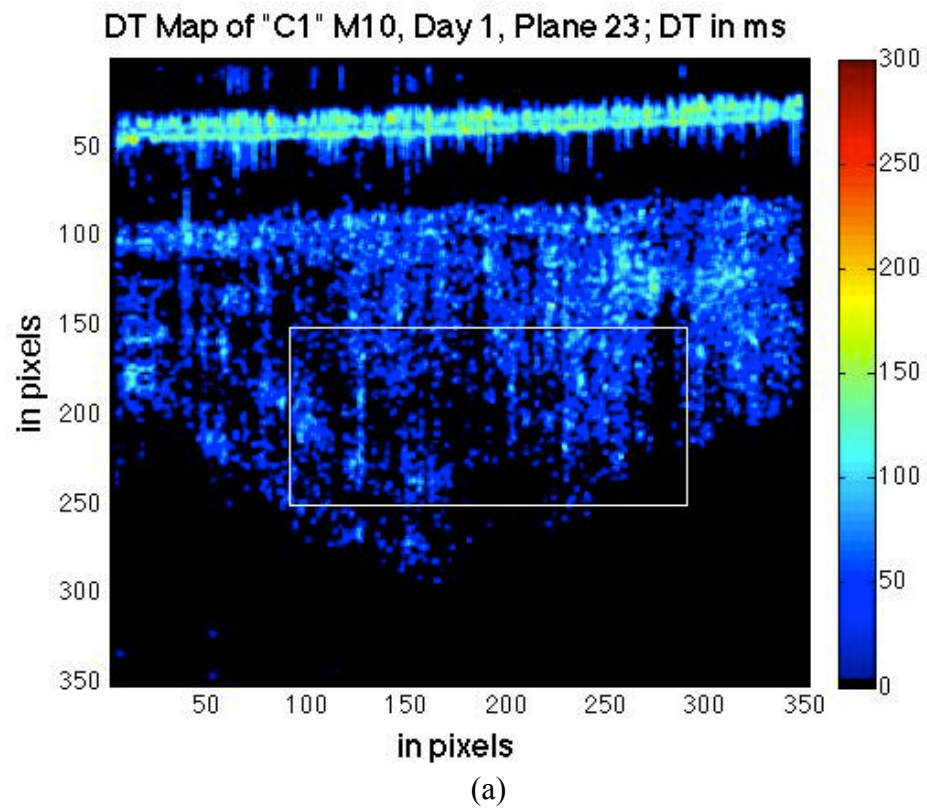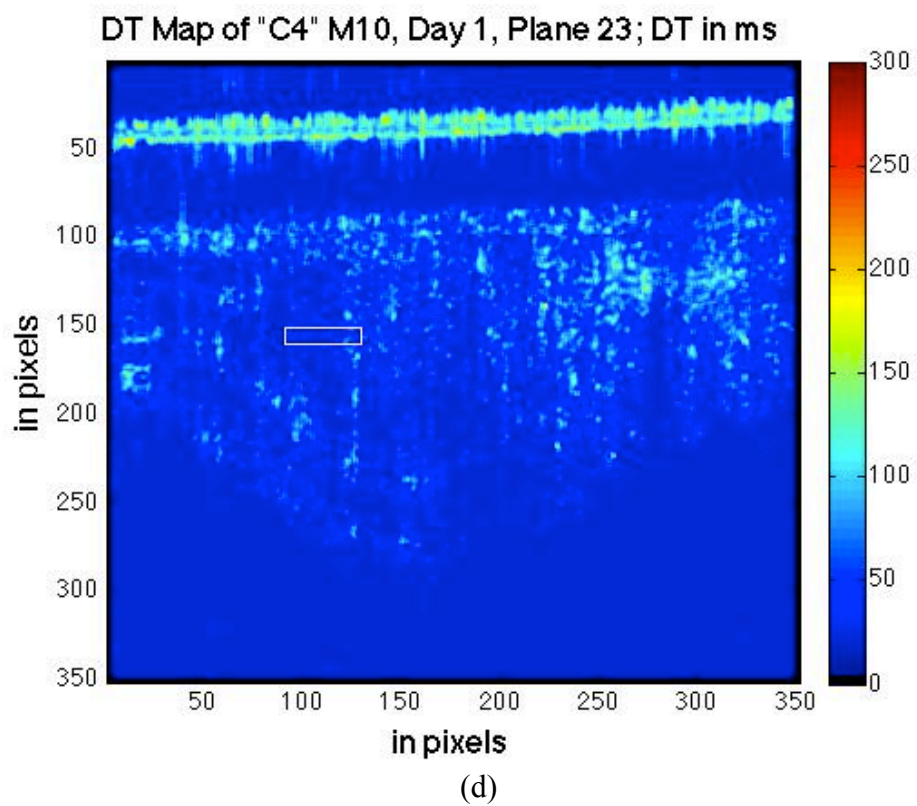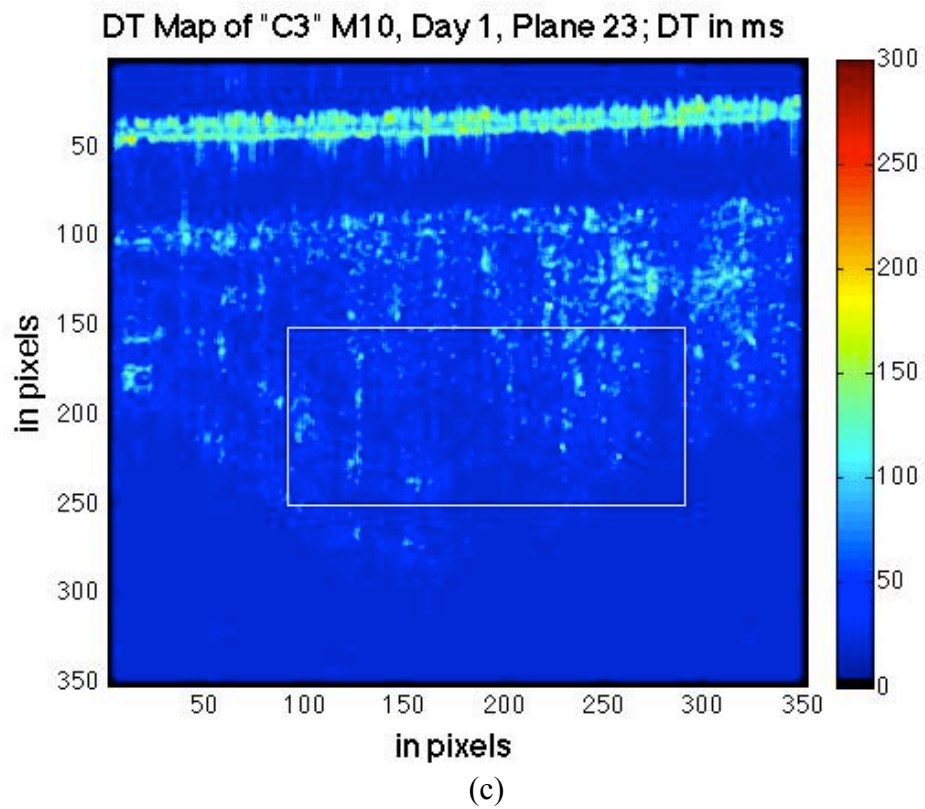
Figure 4-16: DT maps for Mouse 10, Plane 23, on Day 1 correspond to the four categories outlined in Table 4-4: (a) C1; (b) C2; (c) C3; and (d) C4. The image height and image width are both 3 mm for all images.

For all five mice, the average DT was determined for the indicated ROI and plotted for all three days (where data is available for at least two days). The control and cisplatin-injected mice were plotted separately to view the differences in average DT over the treatment days. The error bars for each data point was determined by the standard deviation of the DT values for all the nonzero pixels in the selected ROI. The plots for all four categories are shown in Figures 4-17a to 4-17d.

(a)

(b)

(c)

(d)
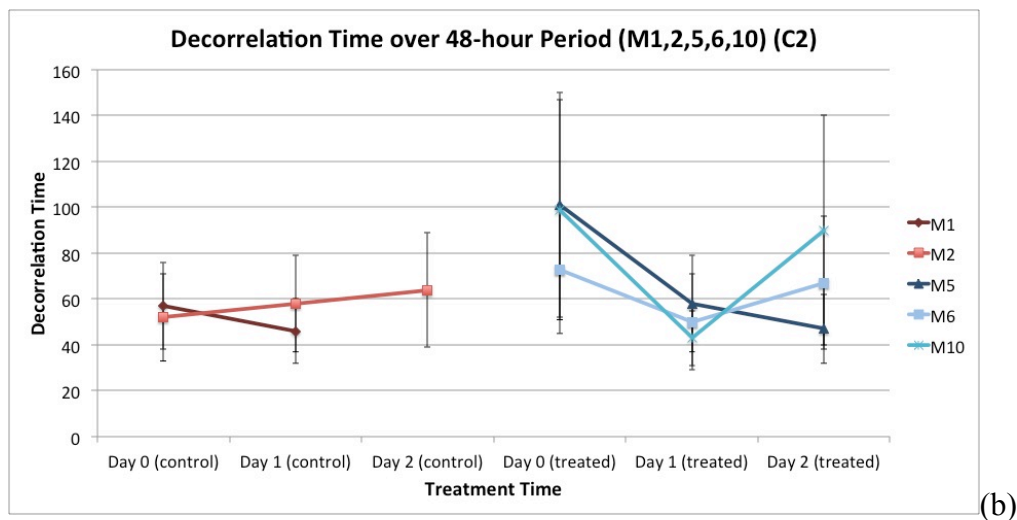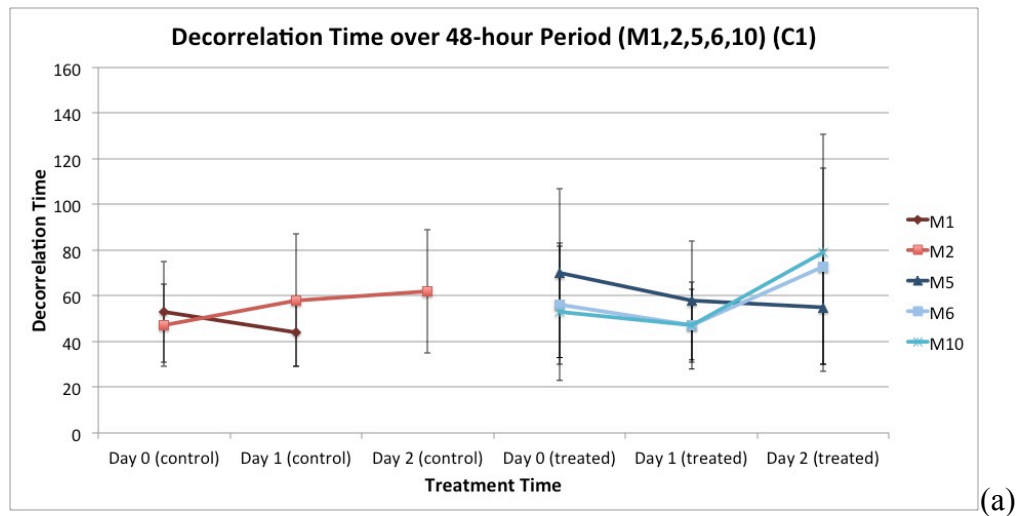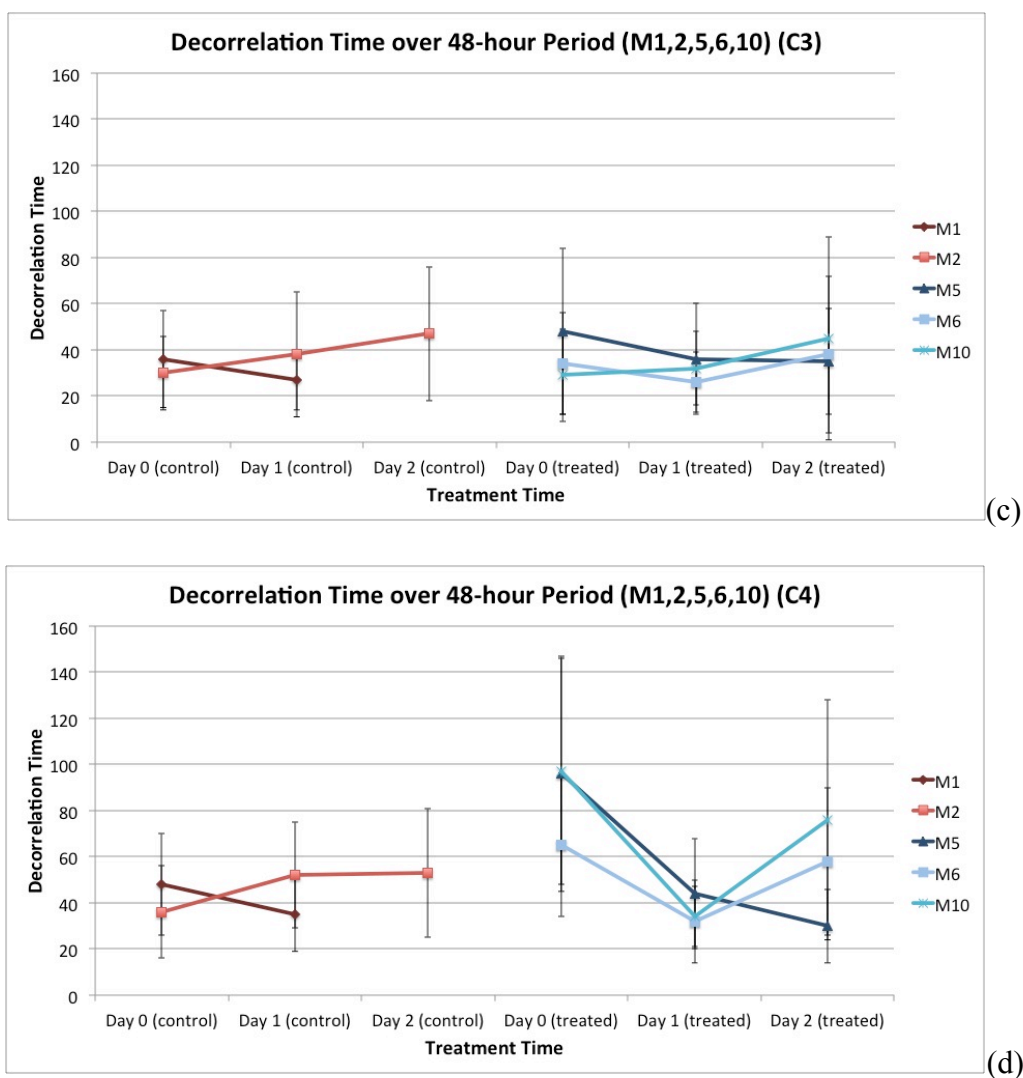
Figure 4-17: Average DT plots (in ms) for five mice over the 48-hour treatment period. Mouse 1 and 2 were control mice and are on the left columns labeled in red and brown. Mouse 5, 6, and 10 were cisplatin-injected mice and are on the right columns labeled in blue colours. Error bars refer to the standard deviation for the averaging of each ROI. The plots correspond to: (a) C1; (b) C2; (c) C3; and (d) C4.

The resulting data from the four plots of average DT over the 48 hours of treatment time for both control and cisplatin-treated mice showed trends of DT changes due to cisplatin effects.

Firstly, comparing categories C1 and C2, it was observed that the selection of the ROI size could potentially affect the average DT for cisplatin-treated mice only. The

graphs for the control mice showed similar average DT throughout the 48 hours irrespective of the window size chosen. The drop in DT from Day 0 to Day 1 for the small ROI in cisplatin-treated mice is consistent with the *in vitro* cell death data [11]. The comparison of the C3 and C4 graphs showed the same graph shapes as comparing C1 and C2 graphs, even though there was no thresholding applied for categories C3 and C4.

The comparison between categories C1 and C3 was to investigate the effect of thresholding when analyzing a large ROI. The similarities in the graphs for the large ROI showed that the thresholding process did not significantly affect the changes in the average DT, but there was a vertical shift (of approximately 20 ms) in the data when the thresholding was not applied. Because only nonzero values were used in the averaging within the ROI, the averaging in category C1 had a lower pixel count than category C3. The averaging in category C3 included the short DT values that were not segmented, resulting in shorter average DT values. This was also observed when comparing categories C2 and C4. The graph trends were the same and the vertical shift was also observed. The average DT values and pixel counts for the data in categories C1, C2, C3, and C4 are shown in Table D-3 in Appendix E.

The data presented in the graphs in Figures 4-17a to 4-17d showed the effect of applying the threshold of 30 ms to segment out pixels of short DT. This data also more clearly illustrates the initial DT drop for Day 1 for cisplatin-treated mice one day after exposure.

Statistical analysis was performed on the data presented in Figure 4-17 to verify the results presented. Table 4-5 presents an excerpt of the results from the Student's t-test performed to compare the means of the average DT values recorded for the control and

cisplatin mice. The control mean was found by averaging the average DT values for control mice #1 and 2. The cisplatin mean was found by averaging the average DT values for cisplatin mice #5, 6 and 10. The assumptions for the Student's t-test were that the populations of the random errors had a normal (Gaussian) distribution, and there was no significant difference between the standard deviations of both population samples. Appendix E has the full summary chart.

Table 4-5: An excerpt of the Student's t-test to compare the means of the average DT values (in ms) recorded for the control and cisplatin mice in Figure 4-17. See Appendix E for the full summary chart.

C2 (n = 400 for all mice); Student's t-test			
	Day 0	Day 1	Day 2
Control mean	54.5	52	64
Cisplatin mean	86	46.5	78.5
Control Std. Dev.	19	17.85	25
Cisplatin Std. Dev.	42.77	18.49	34.48
Pooled Std. Dev.	36.61	18.28	34.48
t-exp	0.9426	0.3296	0.3642
t-th	3.182	3.182	4.303
Decision	Retain H_0	Retain H_0	Retain H_0

The null hypothesis (H_0) is the control and cisplatin means are the same. All of the experimental t-values (t-exp) were less than the theoretical t-values (t-th) at 95% confidence level, resulting in insufficient data to reject the null hypothesis. Therefore, the statistical analysis showed that the control DT mean and cisplatin DT mean were the same, and any differences would be random errors and not systemic errors.

4.4 Histology Analysis

<center>(a)   (b)</center>
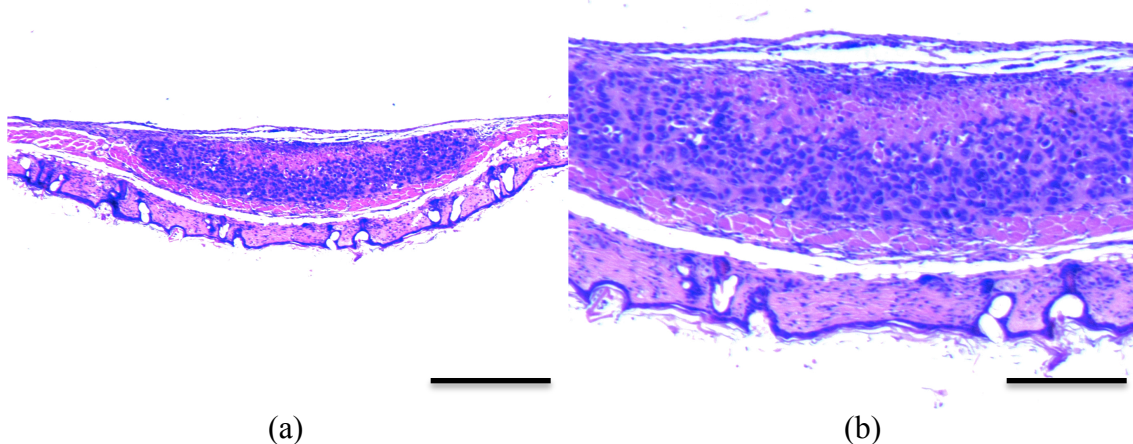
Figure 4-18: H&E staining for Mouse 6 at microscope objective magnifications of (a) 4x (Scale bar = 500 μm) and (b) 10x (Scale bar = 200 μm).

Hematoxylin and eosin (H&E) staining was performed by the Pathology Research Program at the University Health Network for all ten mice in this study to observe the morphology of the dorsal skin tumour tissue in the window chamber model. The sectioning presented tumour growth for mice #1, 2, 3, 5, 6, and 10. Tumour regions were not found in the slides for mice #4, 7, 8, and 9, and thus were not used in the DT analysis of control and cisplatin-injected mice. Figures 4-18 and 4-19 show the histology sections for Mouse 6 and 10, respectively, utilizing objective magnifications of 4x and 10x. Similar morphology was observed in the slides for mice #1, 2, 3 and 5.

(a)   (b)
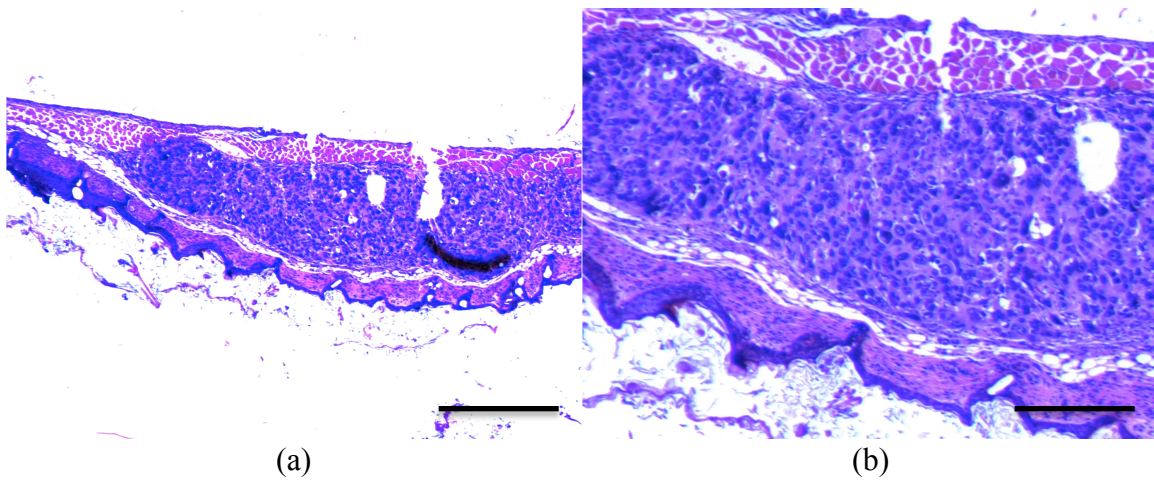
Figure 4-19: H&E staining for Mouse 10 at microscope objective magnifications of (a) 4x (Scale bar = 500 μm) and (b) 10x (Scale bar = 200 μm).

Chapter 5: Discussion

The results from the experiments demonstrated that DLS-OCT could be used to measure the decorrelation time in an *in vivo* mouse tumour model. The OCT b-mode images, decorrelation time maps, and the histology images acquired in this thesis provided an initial assessment for the type of information that is available in the analysis of tumour growth using motion as a source of contrast in OCT. A segmentation technique was developed to separate tissue regions from vessels regions within a ROI, based on the DT values. The decorrelation time analysis of the changes in average DT for control and cisplatin-treated mice across the different imaging planes also provided an insight into the variations within a tumour and how these values change longitudinally for monitoring tumour growth in an *in vivo* setting. The histology results provided another means to observe the location of the tumours in the dorsal skin tumour tissue. The data collected in this thesis illustrate the potential for *in vivo* research of observing fluctuations in scatterers using decorrelation time analysis to study tumour response. A discussion of the results from this thesis follows in this chapter and will provide the foundation for future work in Chapter 6.

5.1 Flow Segmentation

A threshold was placed for all DT maps to segment out any short DT contributions. The previous *in vivo* data had indicated motion due to blood flow as a cause for patches of short DT. Therefore, it was important in this thesis to provide the correct threshold to segment out pixels of short DT before completing any further DT

analysis. The threshold found most effective for all mice in this study was at DT = 30 ms. This threshold provided the most distinct visual qualitative change in the DT maps, while preserving the apparent structure of blood vessels. The threshold of 30 ms seemed to have removed a large portion of short DT pixels that we hypothesize were from blood vessels (Tables 4-2 and 4-3). The increase in the average DT value between the thresholds of 20 to 30 ms was also the greatest in comparison to 30 to 40 ms, 40 to 50 ms, and 50 to 60 ms. The removal of DT contributions at vessel locations allowed for greater accuracy in monitoring the response of tumour cells to treatment via the amount of motion.

The longest and shortest DT values measured were 617 and 20 ms, respectively, as indicated in Section 4.2 and Figure 4-6b. DT measurements have a lower limit of 20 ms in our experimental system due to the Nyquist frequency. The images in this experiment were scanned at a frame rate of 100 frames per second, or 1 frame per 10 milliseconds, resulting in 10 ms being the shortest possible DT measured. However, due to the Nyquist frequency being half of the sampling frequency of 100 Hz, the actual shortest recorded DT was 20 ms. The longest recorded DT value was 617 ms, which was located at a pixel corresponding to the glass coverslip of the window chamber. This result was reasonable, as a fixed piece of glass should have minimal motion recorded. However, it does not guarantee 617 ms is the upper limit of DT as there are many different causes of motion, such as breathing motions and noise inherent to the imaging system. These factors can change the longest DT value recorded, even for something rigid as glass.

5.2 Decorrelation Time Analysis

The DT analysis of different ROIs across adjacent imaging planes yielded the following result: for three ROIs of different sizes and locations, the average DT values across the 625 μm total distance were similar. Figures 4-13 and 4-14 showed the overlapping of the average DT values for all three ROIs ("tumour", "skin", "boundary") across the 26 imaging planes of Mouse 6 and 10. Future work includes analyzing more "tumour", "skin", and "boundary" ROIs to verify the results obtained in this thesis. Another improvement would be to analyze more than 26 imaging planes in order to map a larger distance of average DT to generate a greater scope of the differences in tumour growth along its diameter.

The DT of different ROIs for control and cisplatin-treated mice was also analyzed to study tumour treatment response. In this thesis, ten mice were observed for the changes in average DT over treatment time of 48 hours. For this specific test, the data for five mice were used to illustrate how the average DT changed over treatment time, varying the ROI size as well as the use of the threshold of 30 ms. The comparison of the four categories of data showed that the use of the threshold of 30 ms allowed for the removal of short DT contributions (most likely from vessels), and a vertical shift in the DT graphs was observed because of the change in the pixel values and count when excluding pixels with DT shorter than 30 ms. The shape of the DT graphs did not change when applying the threshold, thus showing that although the threshold did help in providing more representative data related to cellular and extracellular structures, the threshold did not significantly alter the DT contributions from the tissue.

The differences in control and cisplatin-treated mice were also observed in this final assessment. The shapes of the graphs for the control mice for all four categories

were the same, indicating no differences in average DT for ROI size. The average DT values for the control mice were similar throughout the 48 hours between the first and last imaging sessions. Small changes in the DT values can be attributed to metabolic changes of the tumour as it grows. In contrast, the treated tumours showed a difference in the DT values as a function of time. The analysis revealed a drop in the DT from Day 0 to Day 1 for cisplatin-treated mice, which suggests that the tumour is responding to the cisplatin treatment. It is known that apoptotic cells (in this case, due to the cisplatin exposure) undergo cell shrinkage and nuclear fragmentation resulting in increased cellular and intracellular motion. This was a key observation as it corresponded to the previous *in vitro* results of a drop in DT for Day 1. Note that this drop in DT was observed more significantly for the small ROI. Therefore, the specific ROI size chosen could affect the DT results obtained, due to the heterogeneity of the *in vivo* tumour tissue.

The DT analysis of the changes in average DT for different ROIs across different imaging planes yielded results of the similarity of the mix of DT values throughout the same tumour region. The DT analysis of the changes in average DT for control and cisplatin-treated mice provided initial results for monitoring tumour growth in an *in vivo* setting, such as observing the increases and decreases of DT at certain treatment times for specific ROI size, as well as supporting the use of the threshold of 30 ms for segmenting out the DT contributions from blood vessels. This work demonstrated that it was feasible to use DLS-OCT to analyze mouse tumours *in vivo* and obtain results that are similar to previous *in vitro* and *in vivo* studies. It was also shown that DT contributions of vessels could be segmented apart from tissue regions. Further studies and enhancements to this

work are required to draw definite conclusions of the changes in average DT, and will be discussed in the next chapter.

5.3 Image Acquisition

The SS-OCT system used for the DLS-OCT imaging allowed for fast OCT b-mode imaging of the tumour tissue. Because of its 36 kHz scan rate, the duration for obtaining 1000 frames for each imaging plane of tumour data was 10 seconds. Therefore, the total time required for imaging one mouse tumour (26 planes) was under five minutes. The drawbacks to this technique were the storage size for the OCT data within each imaging plane and the sensitivity of the imaging system to breathing movements. The file for each OCT plane of 1000 frames amounted to 968 MB. The total amount of storage space required for the ten mice study was 605 GB. This was significant because an ideal design of the imaging layout was to scan through the whole 1-2 mm diameter of the tumour. Even though only 625 μm of tissue was scanned, it required 605 GB of storage space. Therefore, storage space is an issue that needs to be improved for collecting enough data to map out the whole tumour. The breathing movements of the mouse also affected the data collected with the SS-OCT system. Slight shifts of the tumour tissue were detected in the data; hence, the resulting DT data would have measured not only the tumour motion, but also the breathing motions of the mice.
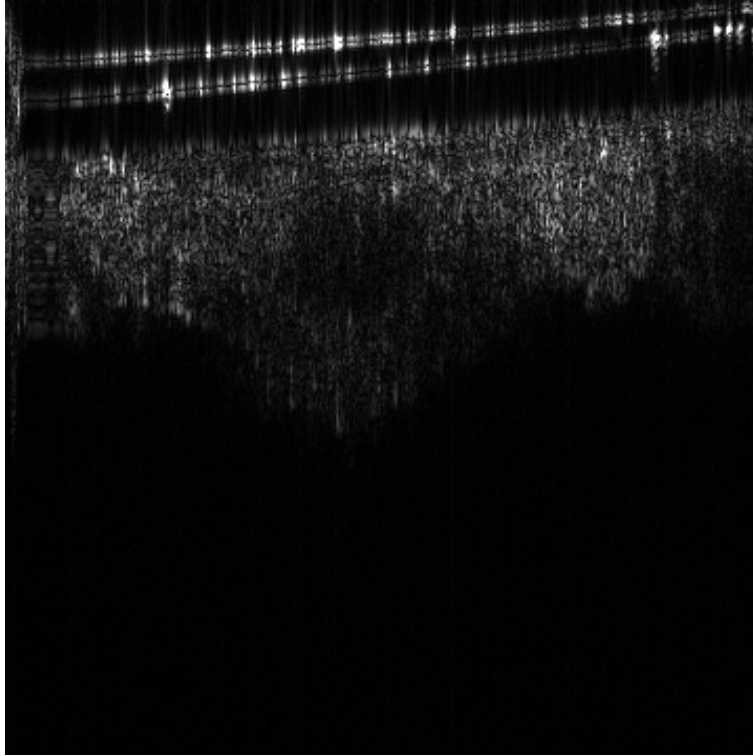
Figure 5-1: Mirroring artifact observed in this cross-sectional b-mode image of the tumour for plane 22 of Mouse 5 on Day 1. The image width and image height are both 3 mm.

Using a fixed stand that holds the tumour tissue (window chamber) in place, or imaging the mouse when the anesthesia effect is at its peak can minimize the breathing motions detected in the OCT images. In addition, a mirroring effect was observed for the OCT b-mode images obtained for Mouse 1 and 5. An example of this is shown in Figure 5-1. This effect may be attributed to a slight misalignment with the returning signal at the circulator. This is a critical issue to the data collection as any artifacts from the OCT b-mode images will be translated to the DT maps. It is of utmost important in the future to check all optical components used in the imaging system before performing the imaging experiment. Lastly, there was noise in the measurements detected that affected the resulting OCT and DT images. Shot noise from the detector, instability of any

mechanical parts of the imaging system, and aberrations in any of the fibres in the optical path will result in noise in all of the OCT images. An ideal estimate of the amount of noise in the OCT and DT images produced is to observe the recorded pixel intensities at a location of something rigid. A suggested location would be the largest recorded DT value of 617 ms corresponding to the glass coverslip of the window chamber. The intensities recorded at the glass coverslip would provide an ideal estimate of motions detected from the noise of the imaging system as the rigid and fixed glass piece would be assumed to have minimal motion.

The histology images acquired included H&E staining to observe the morphology of the cells and to visually differentiate between tumour and non-tumour cells. A suggested improvement to the image acquisition of the H&E slides would be to section the tumour tissue that matches with the specific imaging plane obtained in the OCT b-mode data. This difficulty in this step is to accurately locate the same locations as the OCT images, and then subsequently provide precise micron-thick sections for the H&E slides at those locations. The benefit of having spatially co-registered histology image acquisition is that the structural changes in the tumour as a function of time (tumour growth) or treatment time (tumour response) can be correlated to the changes in cellular structure as assessed by the histology. This may provide insight into the structural changes in tissue that cause the measured changes in the DT.

5.4 Histology Analysis

The H&E staining showed the clear presence of tumours for mice #1, 2, 3, 5, 6, and 10. Although the tumour was evident to the naked eye when performing the mice

imaging due to a small bump where the tumour cells were implanted into the dorsal skin of the mice, this step of histology analysis was important to ensure that the tumours were observed in the DT maps. The H&E slides provided distinction between the morphology of tumour and non-tumour cells. The tumour shape in the histology also allowed for the comparison of the gross tumour shape observed in the DT maps, but the co-registration of the specific location of the histology slide with the exact OCT b-mode imaging plane could not be done. A significant improvement to this experiment would be to have careful histology sectioning to match the OCT b-mode images recorded.

Another addition to the histology data for this experiment would be to perform additional staining besides H&E staining. Terminal deoxynucleotidyl transferase dUTP nick end labeling (TUNEL) is a method that can be applied to detect DNA fragmentation by labeling the terminal end of nucleic acids. This method would provide additional data to support the tumour analysis because TUNEL detects DNA fragmentation that results from apoptotic signaling cascades. Therefore, TUNEL assays can aid the location of cell apoptosis and verify if those locations are where short DT is observed. In addition to TUNEL, platelet endothelial cell adhesion molecule or cluster of differentiation 31 (CD31) staining can also be performed to mark endothelial cells. This staining would allow for the location of blood vessels due to the endothelial lining in the vessels. This would extremely help the assessment of the threshold algorithm as it can verify if the thresholding is performed at the intended locations in the tumour region.

Chapter 6: Conclusions and Future Work

Dynamic light scattering with optical coherence tomography was shown to be a feasible approach for performing speckle decorrelation time analysis in an *in vivo* mouse tumour model. The segmentation of decorrelation time contributions for suspected vessel regions was also performed successfully.

6.1 Realization of Thesis Objectives

There were two key objectives this thesis intended to achieve. The first objective was to perform and measure speckle decorrelation time analysis for control and cisplatin-injected mice over a 48-hour treatment period to observe tumour growth and treatment response kinetics, and then to compare this with histological analysis. Because this thesis involved ten mice in the study, the hope was to demonstrate the feasibility of the DLS-OCT measurements, implement a technique to remove vascular contributions to the tumour tissue DT data, as well as investigate how the DT of tumour tissue changes with treatment time. A technique was developed to segment contributions from blood vessels within tumours based on the DT data. The data presented in this thesis showed that DLS-OCT could be used to measure DT for control and cisplatin-treated mice. This thesis, however, did not present any conclusive average DT trends, but rather, data on the DT changes were obtained with suspected trends that warrant further experiments to support the initial data in order to arrive at conclusions for the changes in average DT. One reason may be the weak response of the tumour to the treatment, as suggested by the analysis of the histology data.

The second objective for this thesis was to determine a threshold value to perform the segmentation of the DT contributions from the microvasculature from the tumour tissue. The previous *in vivo* study measured DT that also included contributions from blood vessels from within a rectangular ROI. In this work, unwanted DT contributions from regions of blood flow were subtracted by finding a valid threshold value in the post-processing step of data analysis. The DT maps for all ten mice were observed and different threshold values were utilized for each DT map to determine the most acceptable threshold value to use. The qualitative results from visualizing the different DT maps with the respective threshold values, and the quantitative results from analyzing the changes in the average DT based on the threshold values both revealed the threshold value of DT = 30 ms was a suitable choice for the thresholding.

6.2 Future Work

The results from this ten-mice study of DLS-OCT to measure the decorrelation time in an *in vivo* mouse tumour model was a first step for a larger study to fully analyze and monitor tumour growth *in vivo*. This experiment can be improved by: a) developing better 3D vessel mapping to unambiguously identify vessel locations, b) imaging a greater portion of the tumour volume (more tumour imaging planes), c) varying the tumour sizes beyond 1-2 mm in diameter to observe different tumour stages and how they respond to the treatment, d) ensuring that the treatment protocol induces strong tumour response, e) increasing the number of mice to be included in the study, and f) use more specific histological stains to identify the viability of tumour and endothelial cells. A repetition of this experiment with the aforementioned enhancements would likely provide

more conclusive results about the potential of DT maps for tumour monitoring and the possibility of this DLS-OCT technique for *in vivo* treatment monitoring in general.

More accurate spatial vessel mapping can greatly enhance the ability to map out a region of vessels using DLS-OCT and speckle variance analysis. Vessel mapping involves the compilation of multiple two-dimensional OCT imaging planes to form a three-dimensional OCT volume structure, and the subsequent application of a specialized speckle variance algorithm to locate and track blood flow within the tumour volume. Having this vessel data, in addition to the algorithm used for forming DT maps, would allow the user to have a 3D OCT volume structure, its respective 3D speckle variance volume, as well as the accompanying 3D DT volume. The benefits of having all three types of data for the same tumour tissue would allow researchers to expand on this work and study the different types of blood flow and tumour growth. This methodology can theoretically be implemented for all types of tumours on any tissue structure to observe the tumour growth pattern and monitor any tumour treatment effects. Importantly, spatial and temporal correlations can be made of blood vessel function (flow) and tumour cell response adjacent to these vessels. Suitable data storage must be designed to support the expansive data for this type of research extension.

In this thesis, the OCT imaging was performed on 26 two-dimensional imaging planes of the size 3 mm in lateral distance and depth. This was effective in measuring a small portion of tumours that were 1-2 mm in diameter, but there are often cases where the desired target is larger than this. This is a small number of planes in order to form the entire tumour volume. Therefore, the increase in the imaging field of view as well as the

number of imaging planes used to form a suitable 3D volume would involve longer data acquisition times and storage space to accommodate for the extra data acquired.

To better sample the different tumour stages and kinetics for the specific cell line, the tumours can be grown to larger sizes. The tumours analyzed in this thesis were all grown for two weeks, which resulted in tumours that were 1-2 mm in diameter. In order to extend to tumour phenotype and study how these tumours respond to treatment, the user can choose to vary the duration of tumour growth before the imaging experiments in order to observe the different tumour stages and how they respond to the treatment.

The treatment duration can also be adjusted in future experiments in order to record more data at different time points during the experiment. For example, the researcher may choose to collect data every 6 hours within the first 48 hours after treatment, as well as collect data after the first 48 hours. The drawback is similarly described above, involving the large amounts of storage space required. Also, if the mice are imaged more frequently, the level of anesthesia must be adequately adjusted to prevent mice mortality from the repeated stress from multiple cycles of anesthesia and imaging.

The ten-mice study was an improvement to the initial three-mice feasibility test, and having ten mice did provide more data to analyze to better establish trends of average DT changes. However, in order to provide more conclusive results, a larger scale experiment with more mice is required to observe the changes in DT over the 48-hour time period.

The histological staining can also be improved by having histological sectioning of the tumour tissue co-registered to match the OCT b-mode planes obtained in the

imaging experiment. This will allow the user to have greater confidence in the correlation between the changes in the DT maps and how these relate to the biological changes suggested in the histology slides (e.g. tumour/endothelial cell death, fibrosis, etc.). Specific stains that can be used are stains to locate areas of DNA fragmentation and cell apoptosis (TUNEL staining) and the presence of blood vessels (CD31 staining).

Technological improvements in the imaging technique can be applied to further enhance the quality of the images acquired and the SNR of the DT measurements. Currently, the DLS-OCT imaging methodology involved the use of a SS-OCT imaging system. Within the field of OCT, there are always improvements that can be made to increase the output power and, therefore, the SNR. Faster OCT imaging instruments will help improve the DT measurements and expand the lower bound of the DT measurements. The continued advancement in OCT systems development will provide the optical means to improve on the data collected in DLS-OCT imaging.

Once the protocol for tumour monitoring is improved and the value of the measurement is rigorously established, the technology can be expanded to study human cancer treatment response to establish the consistency and reliability of the method clinically. A reliable method to monitor tumour response to treatment would have an immediate impact on healthcare: such an approach could be used to switch treatments if the tumour does not respond, saving the healthcare system the cost associated with failed treatments and the patient side-effects of ineffective treatments.

Appendix A: Excerpt of the Animal Protocol for the Mice Experiment

AUP 1280.8

The following are sections pertaining only for this thesis.

Protocol Descriptions/Design

We have recently developed and demonstrated a new functional extension of optical coherence tomography capable of detecting cell death in vitro. Based on these results we are now ready to test this important imaging technique in vivo. The current protocol uses photodynamic therapy to induce tumour cell kill. However, PDT also causes a significant amount of vascular damage, which may cause difficulties for our new imaging technique. Thus we are proposing to use a FaDu (Head and neck, responsive to cisplatin treatment) cell line in conjunction with a single dose of cisplatin to evaluate the efficacy of our new functional imaging technique.

The dorsal skin fold window chamber will be installed in NCRNu (nu/nu animals), providing a free optical path for imaging and treatment. All tumours will be implanted into the fascia of the subcutaneous layer on the skin located opposite the window. The animals will be placed under general anaesthetic (isoflurane) and kept warm on a heated water blanket. To induce the tumours, 100,000 FaDu cells in 100 μl of phosphate buffered saline will be injected between the fascia and the subcutaneous tissue using a 27G needle. Animals will be allowed to recover. They will then be assessed at 1, 6 and 24 h and then on a daily basis to ensure that no adverse effects arise.

Cisplatin treatments will be started when the tumours reach 2-3 mm diameter. Once the tumours have reached this size they will be imaged the 24 hours prior to treatment using SV-OCT and our new functional imaging technique to assess the vascular and cellular state of the tumour. All OCT imaging will be done under our standard protocols using a mixture of xylazine/ketamine (10/80 mg/kg). 24 hours later the cisplatin will be administered via tail vein injection at a dosage of 100 mg/m^2 once again under xylazine/ketamine anesthesia. The mice will then be imaged at one of the following time points after drug administration: 12h, 24h, and 48h. A subgroup of mice (n=5) will be sacrificed at each time point and tumours resected for histochemical analysis and comparison to imaging results. Additionally there will also be a control group of untreated tumour bearing mice that will be sacrificed at the 24-hour time point. Thus, the animal requirements for this amendment are,

Group 1 – Tumour Untreated Control – sacrificed @ 24 hour time point (N=5)

Group 2 – Tumour Treated – sacrificed @ 12 hour time point (N=5)

Group 3 – Tumour Treated – sacrificed @ 24 hour time point (N=5)

Group 4 – Tumour Treated – sacrificed @ 48 hour time point (N=5)

Total N=20

Appendix B: Images of the Mice Experiment
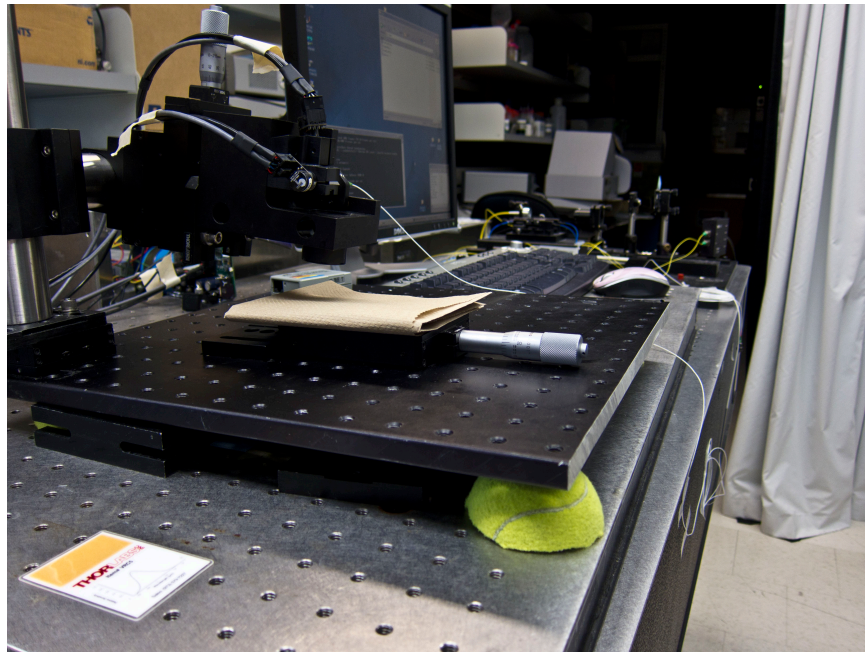
Figure B-1: SS-OCT bench-top setup at Princess Margaret Hospital.
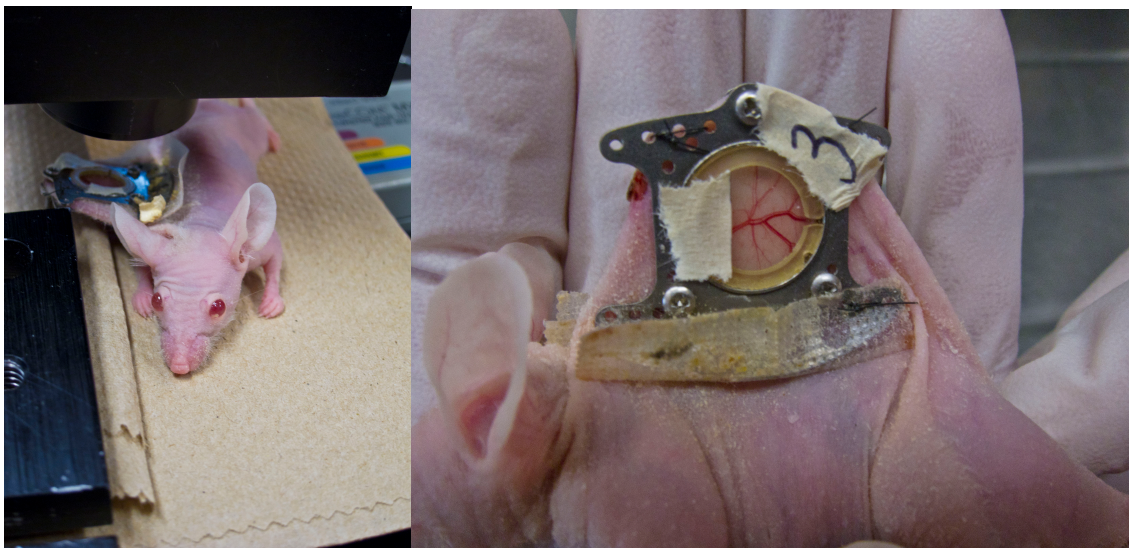
Figure B-2: (left) Dorsal skin window chamber mouse tumour imaging with the SS-OCT system; (right) Dorsal skin window chamber on a mouse.

Appendix C: Sample MATLAB Code for Formulating DT Maps

The following function processes the structural file "S" to produce the decorrelation time maps desired. The specific outputs of this function are the DT map (without averaging), the DT map (with averaging), the power spectrum autocorrelation function, and the heterodyne intermediate scattering function.

```matlab
function [DTmap,DTmapTotal,PSAC,HISFmap]=ProcessDT(S);

clear PSAC
clear Sigtemp
clear PStemp
clear PSACtemp

%%%%%% DEFINE PARAMETERS %%%%%
top=5;
bottom=355;
left=5;
right=355;
startframe=101;
endframe=200;
framerate=50; % (frames/second)
frametime=1/framerate;
winsize=7;

for m=1:(right-left+1)
    for d=1:(bottom-top+1)
    Sigtemp=S(d+top-1,m+left-1,startframe:endframe);
    Sig(d,m,:)=Sigtemp(:);
    PStemp = abs(fft(Sigtemp)).^2;  %<--- Power Spectral Density
    %(Power Spectrum and Autocorrelation function are Fourier transform pairs)
    PSACtemp= 1/length(Sigtemp)*fftshift(real(ifft(PStemp)));
    PSAC(d,m,:)=PSACtemp(:);
```

```matlab
    end
end


numframes=endframe-startframe+1;
numfiles=1;


t=[0:frametime:frametime*(endframe-startframe)/2-1]; % Time array
edge=(winsize-1)/2


DTmap=zeros(bottom-top+1,right-left+1);
%%%  begin sliding window:
for r=(1+edge):(bottom-top-edge+1)
   for c=(1+edge):(right-left-edge+1)


     %  Calculate tSig, eSig and Y for the chosen window
     Sigtemp=Sig(r-edge:r+edge,c-edge:c+edge,:);
     tSig=mean(Sigtemp,3);
     eSig=mean(tSig(:));


     Y=eSig./(tSig(ceil(winsize/2),ceil(winsize/2))); %% Y for middle pixel only


     % Calculate ISF for the middle pixel of this window
     S1=Sig(r,c,:);
     sigmasq=mean(S1.^2)./(mean(S1)).^2-1;
     ISF=1+(1./Y).*(sqrt(PSAC(r,c,:)./(tSig(ceil(winsize/2),ceil(winsize/2)).^2)-sigmasq)-1);


     % Calculate HISF for the middle pixel of this window
     I_ft=eSig*(1-min(ISF(numframes)));
     X=I_ft./tSig(ceil(winsize/2),ceil(winsize/2));
          HISF=1+(1./X).*(sqrt(PSAC(r,c,:)./(tSig(ceil(winsize/2),ceil(winsize/2)).^2)-sigmasq)-1);


     % Calculate decorrelation time for the middle pixel of this window
     DTmap(r,c)=OCT_decorTime(HISF(:),t);
     HISFmap(r,c,:) = HISF(:);


     end
```

```matlab
end


%%%% AVERAGING %%%%%
[l,w]=size(DTmap);
DTmapTotal=zeros(l,w);
for a=2:l-1
    for b=2:w-1
        DTvalues=DTmap(a-1:a+1,b-1:b+1);
        DTvalues=DTvalues(:);
        DTmapTotal(a,b)=mean(DTvalues);
    end
end


end
```

Appendix D: Heterodyne Approach

In order to adequately outline the heterodyne approach described by Joosten et al. [45] and understand ergodicity, it is important to differentiate between time average and ensemble average.
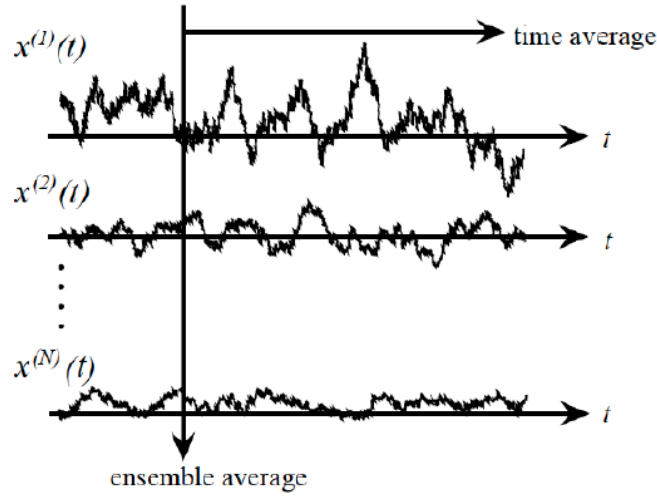
Figure D-1: Time average vs. ensemble average [51].

Time average refers to the average quantity of a single system over a time interval. Ensemble average refers to the averaged quantity of many identical systems at a certain time. Therefore, it is possible to obtain two different types of results for a data set: one statistical analysis for one signal/pixel over a certain period of time (time average), versus one statistical analysis over the entire ensemble of signals/pixels at a certain moment of time (ensemble average).

Ergodicity is a term used to describe whether or not a dynamic system or process has every sample as an equal representative of the whole. In other words, if a system is

ergodic, then every individual signal or sample is also a representative of all of the signals. An ergodic system is when time average and ensemble average give the same result.

The heterodyne approach used in the thesis firstly assumes that the tumour tissues are nonergodic media. This is the right assessment because similar to the gel medium described by Joosten et al. [45], the time-averaged measurements of the tumour tissue will not in general be equivalent to an ensemble-averaged measurement. This is because a tumour tissue will have different cell types and cells in various stages of tumour growth, so taking the signals at one location is not a representative of the whole.

There is a fundamental difference described by Joosten et al. [45] between the nonergodic and heterodyne approaches. Both are used to measure an inhomogeneous system, but the heterodyne approach assumes that the static inhomogeneities do not constitute a relevant part of the system, but the nonergodic situation inherently takes into account all the features of the system without making any assumptions on what is relevant or irrelevant. The heterodyne approach separates the light scattering from the system into contributions from concentration fluctuations of the network and contributions from static macroscopic inhomogeneities. Only the fluctuating signals detected are assumed relevant, whereas the static signals are not considered.

The following steps and equations correspond with the MATLAB code presented in

Appendix C.

The decorrelation time for each pixel of each imaging plane was determined by

calculating the autocorrelation function of the fluctuating signal by taking the inverse

Fourier transform of the power spectrum. (Note: the autocorrelation function and the

signal's power spectrum are Fourier transform pairs.) The autocorrelation function,

$\phi(q, \tau)$, is:

$$\phi(q,\tau) = \overline{I(q,t)I(q,t+\tau)} = \lim_{T\to\infty} \frac{1}{T}\int_{-\frac{T}{2}}^{\frac{T}{2}} I(q,t)I(q,t+\tau)dt \qquad \textbf{Eq.D-1}$$

The time-averaged normalized autocorrelation function, $g_T{}^{(2)}(q,\tau)$, is calculated as:

$$g_T{}^{(2)}(q,\tau) \equiv \frac{\phi(q,\tau)}{\langle I(q,0)\rangle_T{}^2} = \frac{\langle I(q,0)I(q,\tau)\rangle_T}{\langle I(q,0)\rangle_T{}^2} \qquad \textbf{Eq.D-2}$$

The heterodyne approach removes the static scattering contribution of the 7 by 7 pixel

region from the intensity autocorrelation function to produce the heterodyne intermediate

scattering function (ISF).

For a chosen 7 by 7 pixel window, the time-averaged normalized autocorrelation function

in Eq.D-2 is used to calculate the ISF, $f(q,\tau)$:

$$f(q,\tau) \equiv 1 + \frac{1}{Y}\left[\sqrt{g_T{}^{(2)}(q,\tau) - \sigma_I{}^2} - 1\right] \qquad \textbf{Eq.D-3}$$

where Y is the ratio between the ensemble average intensity over the time average

intensity:

$$Y \equiv \frac{\langle I(q) \rangle_E}{\langle I(q) \rangle_T} \tag{Eq.D-4}$$

and $\sigma_I{}^2$ is the mean-square intensity fluctuation:

$$\sigma_I{}^2 \equiv \frac{\langle I^2(q) \rangle_T}{\langle I(q) \rangle_T{}^2} - 1 = g_T{}^{(2)}(q,0) - 1 \tag{Eq.D-5}$$

The heterodyne ISF equation is similar to Eq.D-3, except the ratio X is used instead of Y:

$$f_N(q,\tau) = 1 + \frac{1}{X}\left[\sqrt{g_T{}^{(2)}(q,\tau) - \sigma_I{}^2} - 1\right] \tag{Eq.D-6}$$

where X is the ratio between the time average fluctuating intensity over the time average intensity:

$$X \equiv \frac{\langle I_F(q) \rangle_T}{\langle I(q) \rangle_T} \tag{Eq.D-7}$$

The 1/e value of the heterodyne ISF was then used to calculate the DT that was displayed in the DT map, after which 3 by 3 spatial averaging is applied to produce the final DT map.

Appendix E: Threshold Charts

The following two summary charts correspond to Tables 4-2 and 4-3. The chart data for average DT, difference, and pixel count for each threshold are presented for Mouse 6 and Mouse 10.

Table E-1: A full summary chart of the data corresponding to Table 4-2 for Mouse 6 from Day 0 to Day 2. Difference refers to the increase in average DT compared to the next longest DT threshold.

Day 0					Day 1					Day 2				
Plane	Thres	AvgDT	Diff	PixelCount	Plane	Thres	AvgDT	Diff	PixelCount	Plane	Thres	AvgDT	Diff	PixelCount
8	20	36	22	1500	6	20	46	9	1500	5	20	58	23	1500
	30	58	11	582		30	55	8	1065		30	81	10	915
	40	69	10	401		40	63	10	769		40	91	10	755
	50	79	7	290		50	73	8	504		50	101	9	624
	60	86		223		60	81		350		60	110		527
9	20	36	25	1500	7	20	58	11	1500	6	20	59	22	1500
	30	61	8	555		30	69	7	1125		30	81	10	942
	40	69	14	428		40	76	9	939		40	91	8	775
	50	83	9	280		50	85	7	741		50	99	9	662
	60	92		211		60	92		596		60	108		555
10	20	32	17	1500	8	20	42	14	1500	7	20	83	27	1500
	30	49	8	554		30	56	10	843		30	110	10	1042
	40	57	12	358		40	66	11	577		40	120	9	923
	50	69	9	198		50	77	10	380		50	129	10	819
	60	78		121		60	87		270		60	139		728
11	20	35	20	1500	9	20	36	15	1500	8	20	64	16	1500
	30	55	8	558		30	51	12	706		30	80	9	1068
	40	63	11	402		40	63	13	427		40	89	9	890
	50	74	9	258		50	76	10	244		50	98	7	743
	60	83		176		60	86		171		60	105		646
12	20	42	18	1500						9	20	83	16	1500
	30	60	7	787							30	99	9	1182
	40	67	11	608							40	108	9	1037
	50	78	6	419							50	117	6	910
	60	84		330							60	123		829
13	20	41	16	1500						10	20	72	19	1500
	30	57	7	831							30	91	11	1074
	40	64	8	640							40	102	9	912
	50	72	7	453							50	111	8	783
	60	79		320							60	119		686
14	20	69	15	1500						11	20	89	24	1500
	30	84	10	1124							30	113	10	1100
	40	94	11	930							40	123	9	968
	50	105	8	771							50	132	8	875
	60	113		668							60	140		792
15	20	46	16	1500						12	20	73	20	1500
	30	62	58	906							30	93	8	1085
	40	120	26	758							40	101	9	958
	50	146	18	562							50	110	9	827
	60	164		469							60	119		710

Table E-2: A full summary chart of the data corresponding to Table 4-3 for Mouse 10 from Day 0 to Day 2. Difference refers to the increase in average DT compared to the next longest DT threshold.

		Day 0					Day 1					Day 2		
Plane	Thres	AvgDT	Diff	PixelCount	Plane	Thres	AvgDT	Diff	PixelCount	Plane	Thres	AvgDT	Diff	PixelCount
0	20	23	14	9000	0	20	23	14	9000	0	20	42	19	9000
	30	37	10	725		30	37	9	848		30	61	7	4706
	40	47	14	176		40	46	9	247		40	68	11	3649
	50	61	9	38		50	55	7	50		50	79	8	2523
	60	70		17		60	62		8		60	87		1921
1	20	25	19	9000	1	20	25	17	9000	1	20	44	18	9000
	30	44	11	1353		30	42	8	1728		30	62	11	4769
	40	55	14	647		40	50	11	820		40	73	12	3482
	50	69	11	295		50	61	11	300		50	85	9	2485
	60	80		177		60	72		121		60	94		1901
2	20	25	18	9000	2	20	27	15	9000	2	20	36	17	9000
	30	43	12	1181		30	42	7	2316		30	53	8	3899
	40	55	15	516		40	49	12	1148		40	61	10	2802
	50	70	11	228		50	61	9	377		50	71	8	1734
	60	81		136		60	70		166		60	79		1184
3	20	24	16	9000	3	20	27	15	9000	3	20	53	22	9000
	30	40	10	1240		30	42	9	2418		30	75	9	5270
	40	50	12	467		40	51	10	1139		40	84	10	4284
	50	62	8	171		50	61	9	470		50	94	7	3459
	60	70		83		60	70		221		60	101		2945
4	20	27	18	9000	4	20	26	14	9000	4	20	49	24	9000
	30	45	10	2112		30	40	8	2128		30	73	9	4681
	40	55	13	1109		40	48	11	860		40	82	9	3879
	50	68	12	517		50	59	11	269		50	91	8	3125
	60	80		277		60	70		97		60	99		2558
5	20	24	15	9000	5	20	30	12	9000	5	20	56	26	9000
	30	39	11	1130		30	42	8	3369		30	82	9	5027
	40	50	16	377		40	50	10	11714		40	91	8	4292
	50	66	9	113		50	60	8	689		50	99	7	3627
	60	75		67		60	68		286		60	106		3153
6	20	23	14	9000	6	20	32	12	9000	6	20	52	23	9000
	30	37	10	665		30	44	8	3770		30	75	9	5133
	40	47	10	194		40	52	10	2050		40	84	11	4197
	50	57	7	53		50	62	10	883		50	95	8	3302
	60	64		16		60	72		409		60	103		2736
7	20	25	18	9000	7	20	34	13	9000	7	20	34	17	9000
	30	43	10	1420		30	47	8	4197		30	51	9	3638
	40	53	12	677		40	55	9	2607		40	60	12	2398
	50	65	8	310		50	64	8	1392		50	72	8	1384
	60	73		173		60	72		788		60	80		939
8	20	24	17	9000	8	20	36	12	9000	8	20	38	12	9000
	30	41	11	1012		30	48	8	4741		30	60	9	3703
	40	52	11	387		40	56	11	3041		40	69	11	2797
	50	63	8	170		50	67	7	1649		50	80	8	1937
	60	71		96		60	74		1021		60	88		1451
9	20	22	16	9000	9	20	36	13	9000	9	20	38	12	9000
	30	38	9	563		30	49	8	4433		30	60	8	3901
	40	47	12	174		40	57	10	2928		40	68	10	2971
	50	59	7	50		50	67	8	1684		50	78	9	2076
	60	66		19		60	75		1020		60	87		1526
10	20	23	17	9000	10	20	37	13	9000	10	20	43	23	9000
	30	40	10	852		30	50	7	4709		30	66	8	4441
	40	50	10	308		40	57	10	3165		40	74	11	3510
	50	60	7	116		50	67	8	1804		50	85	8	2573
	60	67		54		60	75		1095		60	93		2042
11	20	24	22	9000	11	20	34	15	9000	11	20	39	23	9000

	30	46	15	1003		30	49	8	4066		30	62	8	3803
	40	61	15	442		40	57	10	2636		40	70	11	2969
	50	76	11	238		50	67	7	1528		50	81	8	2092
	60	87		161		60	74		976		60	89		1584
12	20	23	16	9000	12	20	37	15	9000	12	20	54	26	9000
	30	39	9	780		30	52	8	4363		30	80	8	4976
	40	48	11	302		40	60	10	2928		40	88	11	4242
	50	59	8	94		50	70	7	1818		50	99	8	3398
	60	67		35		60	77		1228		60	107		2899
13	20	24	21	9000	13	20	38	12	9000	13	20	49	27	9000
	30	45	10	1190		30	50	7	4943		30	76	9	4547
	40	55	12	601		40	57	9	3371		40	85	9	3746
	50	67	9	299		50	66	8	1978		50	94	8	3037
	60	76		178		60	74		1214		60	102		2530
14	20	24	18	9000	14	20	38	14	9000	14	20	38	21	9000
	30	42	13	1084		30	52	7	4849		30	59	9	3855
	40	55	11	445		40	59	10	3453		40	68	10	2887
	50	66	8	218		50	69	8	2105		50	78	9	1994
	60	74		125		60	77		1412		60	87		1461
15	20	22	18	9000	15	20	38	13	9000	15	20	51	21	9000
	30	40	11	583		30	51	8	4835		30	72	11	5091
	40	51	12	204		40	59	10	3276		40	83	10	3988
	50	63	10	80		50	69	7	1976		50	93	9	3120
	60	73		39		60	76		1299		60	102		2563
16	20	24	23	9000	16	20	38	13	9000	16	20	39	21	9000
	30	47	13	913		30	51	8	4752		30	60	9	3967
	40	60	12	485		40	59	10	3274		40	69	11	2958
	50	72	8	269		50	69	7	2037		50	80	8	2087
	60	80		190		60	76		1325		60	88		1567
17	20	25	24	9000	17	20	39	12	9000	17	20	46	19	9000
	30	49	11	1158		30	51	7	5212		30	65	8	4938
	40	60	13	656		40	58	9	3701		40	73	11	3879
	50	73	10	367		50	67	7	2326		50	84	9	2843
	60	83		247		60	74		1490		60	93		2176
18	20	26	18	9000	18	20	40	12	9000	18	20	36	17	9000
	30	44	11	1569		30	52	8	5252		30	53	8	4020
	40	55	14	758		40	60	9	3683		40	61	11	2846
	50	69	11	348		50	69	8	2304		50	72	9	1762
	60	80		206		60	77		1521		60	81		1203
19	20	26	20	9000	19	20	41	12	9000	19	20	47	19	9000
	30	46	13	1488		30	53	7	5310		30	66	8	4989
	40	59	16	719		40	60	9	3882		40	74	10	4018
	50	75	14	351		50	69	8	2438		50	84	8	3015
	60	89		213		60	77		1601		60	92		2325
20	20	27	20	9000	20	20	42	11	9000	20	20	66	25	9000
	30	47	12	1846		30	53	7	5695		30	91	9	5823
	40	59	15	967		40	60	9	4149		40	100	9	4996
	50	74	13	493		50	69	7	2692		50	109	6	4329
	60	87		295		60	76		1847		60	115		3874
21	20	26	20	9000	21	20	42	10	9000	21	20	27	15	9000
	30	46	11	1845		30	52	7	5800		30	42	9	2136
	40	57	11	978		40	59	9	4178		40	51	10	1032
	50	68	8	522		50	68	7	2665		50	61	9	426
	60	76		336		60	75		1689		60	69		200
22	20	25	20	9000	22	20	42	11	9000	22	20	67	24	9000
	30	45	11	1445		30	53	6	5729		30	91	8	5870
	40	56	13	712		40	59	10	4210		40	99	10	5115
	50	69	11	359		50	69	7	2578		50	109	9	4331
	60	80		203		60	76		1703		60	118		3714
23	20	22	15	9000	23	20	40	11	9000	23	20	61	22	9000
	30	37	11	460		30	51	7	5311		30	83	9	5689
	40	48	13	115		40	58	9	3686		40	92	9	4807

	50	61	14	34		50	67	8	2210		50	101	8	3995
	60	75		12		60	75		1400		60	109		3416
24	20	25	17	9000	24	20	38	12	9000	24	20	48	22	9000
	30	42	11	1583		30	50	7	5155		30	70	7	4938
	40	53	12	689		40	57	10	3466		40	77	10	4025
	50	65	9	293		50	67	7	1999		50	87	9	3124
	60	74		162		60	74		1243		60	96		2481
25	20	27	21	9000	25	20	40	11	9000	25	20	46	21	9000
	30	48	11	1921		30	51	7	5620		30	67	9	4848
	40	59	16	1064		40	58	9	3892		40	76	9	3866
	50	75	10	535		50	67	8	2327		50	85	9	2967
	60	85		353		60	75		1436		60	94		2316

The following summary chart corresponds to Table 4-4 regarding average DT and pixel count values for categories C1, C2, C3, and C4 for mice #1, 2, 5, 6, and 10.

Table E-3: Actual average DT values and pixel counts for all four categories corresponding to Table 4-4.

	Day 0 Average DT	Day 0 Pixel Count	Day 1 Average DT	Day 1 Pixel Count	Day 2 Average DT	Day 2 Pixel Count
M1; C1	53	8997	44	4987	N/A	N/A
M1; C2	57	299	46	198	N/A	N/A
M1; C3	36	20000	27	19900	N/A	N/A
M1; C4	48	400	35	390	N/A	N/A
M2; C1	47	6641	58	8918	62	12301
M2; C2	52	183	58	335	64	291
M2; C3	30	20000	38	20000	47	20000
M2; C4	36	400	52	400	53	400
M5; C1	70	11180	58	7823	55	7846
M5; C2	101	375	58	246	47	144
M5; C3	48	20000	36	20000	35	20000
M5; C4	96	400	44	400	30	400
M6; C1	56	6964	47	3930	73	6528
M6; C2	73	341	50	146	67	317
M6; C3	34	20000	26	20000	38	20000
M6; C4	65	400	32	400	58	400
M10; C1	53	4669	47	7703	79	8163
M10; C2	99	386	43	206	90	319
M10; C3	29	20000	32	20000	45	20000

| M10; C4 | 97 | 400 | 34 | 400 | 76 | 400 |

The following summary chart corresponds to Table 4-5 regarding the Student's t-test to compare the means of the average DT values of control mice (#1 and 2) and cisplatin mice (#5, 6 and 10) for categories C1, C2, C3, and C4.

For the Student's t-test,

H_0 = the control and cisplatin means are the same (any differences would be random)

H_a = the control and cisplatin means are systematically different

Reject H_0 if the experimental t-value (t-exp) is greater than the theoretical t-value (t-th)

Confidence level = 95% ($\alpha = 0.05$)

The experimental t-values (t-exp) were calculated to be:

$$t_{exp} = \frac{|\overline{X_A} - \overline{X_B}|}{S_{AB}\sqrt{\frac{1}{n_A}+\frac{1}{n_B}}}$$
Eq.E-1

where SAB is the pooled estimate of the standard deviation:

$$S_{AB} = \sqrt{\frac{(n_A-1)s_A{}^2+(n_B-1)s_B{}^2}{n_A+n_B-2}}$$
Eq.E-1

The theoretical t-values (t-th) were found from t-distribution tables.

Table E-4: Student's t-test for comparing the means for control and cisplatin mice for all four categories corresponding to Table 4-5.

	C1 (n = 20000 for all mice)				C2 (n = 400 for all mice)		
	Day 0	Day 1	Day 2		Day 0	Day 1	Day 2
M1, mean	53	44		M1, mean	57	46	
M2, mean	47	58	62	M2, mean	52	58	64
Control mean	50	51	62	Control mean	54.5	52	64
M5, mean	70	58	55	M5, mean	101	58	47
M6, mean	56	47	73	M6, mean	73	50	67
M10, mean	53	47	79	M10, mean	99	43	90
Cisplatin mean	54.5	47	76	Cisplatin mean	86	46.5	78.5
M1, Std. Dev.	22	15		M1, Std. Dev.	19	14	
M2, Std. Dev.	18	29	27	M2, Std. Dev.	19	21	25
Control Std. Dev.	20.10	23.09	27	Control Std. Dev.	19	17.85	25
M5, Std. Dev.	37	26	25	M5, Std. Dev.	49	21	15
M6, Std. Dev.	26	19	43	M6, Std. Dev.	28	21	29
M10, Std. Dev.	30	16	52	M10, Std. Dev.	48	12	50
Cisplatin Std. Dev.	31.33	20.76	41.55	Cisplatin Std. Dev.	42.77	18.49	34.48
Pooled Std. Dev.	28.09	21.56	41.55	Pooled Std. Dev.	36.61	18.28	34.48
t-exp	0.1755	0.2032	0.2918	t-exp	0.9426	0.3296	0.3642
df	3	3	2	df	3	3	2
t-th	3.182	3.182	4.303	t-th	3.182	3.182	4.303
Decision	Retain H_0	Retain H_0	Retain H_0	Decision	Retain H_0	Retain H_0	Retain H_0

C3 (n = 20000 for all mice)				C4 (n = 400 for all mice)			
	Day 0	Day 1	Day 2		Day 0	Day 1	Day 2
M1, mean	36	27		M1, mean	48	35	
M2, mean	30	38	47	M2, mean	36	52	53
Control mean	33	32.5	47	Control mean	42	43.5	53
M5, mean	48	36	35	M5, mean	96	44	30
M6, mean	34	26	38	M6, mean	65	32	58
M10, mean	29	32	45	M10, mean	97	34	76
Cisplatin mean	31.5	29	41.5	Cisplatin mean	81	33	67
M1, Std. Dev.	21	13		M1, Std. Dev.	22	16	
M2, Std. Dev.	16	27	29	M2, Std. Dev.	20	23	28
Control Std. Dev.	18.67	21.19	29	Control Std. Dev.	21.02	19.81	36.44
M5, Std. Dev.	36	24	23	M5, Std. Dev.	51	24	16
M6, Std. Dev.	22	13	34	M6, Std. Dev.	31	18	32
M10, Std. Dev.	20	16	44	M10, Std. Dev.	49	13	52
Cisplatin Std. Dev.	26.96	18.27	34.74	Cisplatin Std. Dev.	44.58	18.88	36.44
Pooled Std. Dev.	24.51	19.29	34.74	Pooled Std. Dev.	38.37	19.19	36.44
t-exp	0.0670	0.1988	0.1371	t-exp	1.1134	0.5992	0.3327
df	3	3	2	df	3	3	2
t-th	3.182	3.182	4.303	t-th	3.182	3.182	4.303
Decision	Retain H_0	Retain H_0	Retain H_0	Decision	Retain H_0	Retain H_0	Retain H_0

Bibliography

[1] W Drexler, "Ultrahigh-resolution optical coherence tomography," *J. Biomed. Opt.*, vol. 9, no. 1, pp. 47-74, 2004.

[2] JG Fujimoto, BE Bouma, GJ Tearney, "Optical Coherence Tomography: Introduction," in *Handbook of Optical Coherence Tomography*, Ed. New York, NY, USA: Marcel Dekker, pp. 1-40, 2002.

[3] B Hermann, M Esmaeelpour, B Považay, B Hofer, F Bounaparte, N Sheen, R North, W Drexler, "Wide field visualization of retinal and choroidal microstructure in vivo frequency domain OCT at 1060 nm with up to 47000 lines/s," *Proc. SPIE Int. Soc. Opt. Eng.*, vol. 7163, pp.71630A, 2009.

[4] A Unterhuber, B Považay, B Hermann, H Sattmann, A Chavez-Pirson, W Drexler, "In vivo retinal optical coherence tomography at 1040 nm - enhanced penetration into the choroid," *Opt. Express*, vol. 13, no. 9, pp. 3252-3258, May 2005.

[5] W Drexler, JG Fujimoto, "State-of-the-art retinal optical coherence tomography," *Prog. Retin. Eye Res.*, vol. 27, pp. 45-88, 2008.

[6] GJ Tearney, ME Brezinski, BE Bouma, SA Boppart, C Pitris, JF Southern, JG Fujimoto, "In Vivo Endoscopic Optical Biopsy with Optical Coherence Tomography," *Science*, vol. 276, no. 5321, pp. 2037-2039, 1997.

[7] BA Standish, KKC Lee, A Mariampillai, NR Munce, MKK Leung, VXD Yang, IA Vitkin, "In vivo endoscopic multi-beam optical coherence tomography," *Phys. Med. Biol.*, vol. 55, pp. 615-622, 2010.

[8] Z Chen, W Jung, Y-C Ahn, A Sepehr, WB Armstrong, M Brenner, DT McCormick, NC Tien, "High speed three-dimensional endoscopic OCT using MEMS technology," *Proc. SPIE Int. Soc. Opt. Eng.*, vol. 6466, pp. 64660H, 2007.

[9] MV Sivak Jr, K Kobayashi, JA Izatt, AM Rollins, R Ung-runyawee, A Chak, RCK Wong, GA Isenberg, J Willis, "High-resolution endoscopic imaging of the GI tract using optical coherence tomography," *Gastrointest. Endosc.*, vol. 51, no. 4, pp. 474-479, 2000.

[10] VXD Yang, S-J Tang, ML Gordon, B Qi, G Gardiner, M Cirocco, P Kortan, GB Haber, G Kandel, IA Vitkin, BC Wilson, NE Marcon, "Endoscopic Doppler optical coherence tomography in the human GI tract: initial experience," *Gastrointest. Endosc.*, vol. 61, no. 7, pp. 879-890, 2005.

[11] G Farhat, A Mariampillai, VXD Yang, GJ Czarnota, MC Kolios, "Detecting apoptosis using dynamic light scattering with optical coherence tomography," *J. Biomed. Opt.*, vol. 16, no. 7, pp. 070505, 2011.

[12] G Farhat, A Mariampillai, KKC Lee, VXD Yang, GJ Czarnota, MC Kolios, "Measuring intracellular motion using dynamic light scattering with optical coherence tomography in a mouse tumor model," *Proc. SPIE Int. Soc. Opt. Eng.*, vol. 8230, pp. 823002, 2012.

[13] TD Pollard, "The cytoskeleton, cellular motility and the reductionist agenda," *Nature*, vol. 422, pp. 741-745, 2003.

[14] D Mizuno, C Tardin, CF Schmidt, FC MacKintosh, "Nonequilibrium Mechanics of Active Cytoskeletal Networks," *Science*, vol. 315, pp. 370-373, 2007.

[15] F Julicher, A Ajdari, J Prost, "Modeling molecular motors," *Rev. Mod. Phys.*, vol. 69, no. 4, pp. 1269-1281, 1997.

[16] CP Brangwynne, GH Koenderink, FC MacKintosh, DA Weitz, "Intracellular transport by active diffusion," *Trends Cell Biol.*, vol. 19, no. 9, pp. 423-427, 2009.

[17] M Suissa, C Place, E Goillot, E Freyssingeas, "Internal dynamics of a living cell nucleus investigated by dynamic light scattering," *Eur. Phys. J. E.*, vol. 26, pp. 435-448, 2008.

[18] C Joo, CL Evans, T Stepinac, T Hasan, JF de Boer, "Diffusive and directional intracellular dynamics measured by field-based dynamic light scattering," *Opt. Express*, vol. 18, no. 3, pp. 2858-2871, 2010.

[19] RB Tishler, FD Carlson, "A Study of the Dynamic Properties of the Human Red Blood Cell Membrane Using Quasi-Elastic Light-Scattering Spectroscopy," *Biophys. J.*, vol. 65, pp. 2586-2600, 1993.

[20] A Palmer, TG Mason, JY Xu, SC Kuo, D Wirtz, "Diffusing Wave Spectroscopy Microrheology of Actin Filament Networks," *Biophys J.*, vol. 76, pp. 1063-1071, 1999.

[21] M Heckmeier, SE Skipetrov, G Maret, R Maynard, "Imaging of dynamic heterogeneities in multiple-scattering media," *J. Opt. Soc. Am. A*, vol. 14, no. 1, pp. 185-191, 1997.

[22] J Lee, W Wu, JY Jiang, B Zhu, DA Boas, "Dynamic light scattering optical coherence tomography," *Opt. Express*, vol. 20, no. 20, pp. 22262-22277, 2012.

[23] JG Fujimoto, "Optical coherence tomography," *Appl. Phys.*, vol. 2, no. 4, pp. 1099-1111, July 2001.

[24] AF Fercher, W Drexler, CK Hitzenberger, T Lasser, "Optical Coherence Tomography - Principles and Applications," *Rep. Prog. Phys.*, vol. 66, pp. 239-303, 2003.

[25] A Mauro, "High Speed Rotary System for Catheter Based 3-D Imaging with Optical Coherence Tomography (OCT)," Biomedical Physics, Ryerson University, Toronto, MSc Thesis 2009.

[26] ME Brezinski, *Optical Coherence Tomography: Principles and Applications,* Academic Press, Burlington, MA, USA, 2006.

[27] AF Fercher, "Optical coherence tomography – development, principles, applications", *Z. Med. Phys.*, vol. 20, pp. 251-276, 2010.

[28] E Ergun, B Hermann, M Wirtitsch, A Unterhuber, TH Ko, H Sattmann, C Scholda, JG Fujimoto, M Stur, W Drexler, "Assessment of Central Visual Function in Stargardt's Disease/Fundus Flavimaculatus with Ultrahigh-Resolution Optical Coherence Tomography," *Invest. Ophthalmol. Vis. Sci.*, vol. 46, no. 1, pp. 310-316, 2005.

[29] W Drexler, H Sattmann, B Hermann, TH Ko, M Stur, A Unterhuber, C Scholda, O Findl, M Wirtitsch, JG Fujimoto, AF Fercher, "Enhanced visualization of macular pathology with the use of ultrahigh-resolution optical coherence tomography," *Arch Ophthalmol.*, vol. 121, no. 5, pp. 695-706, 2003.

[30] MG Wirtitsch, E Ergun, B Hermann, A Unterhuber, M Stur, C Scholda, H Sattmann, TH Ko, JG Fujimoto, W Drexler, "Ultrahigh Resolution Optical Coherence Tomography In Macular Dystrophy," *Am J Ophthalmol*, vol. 140, no. 6, pp. 976-983, 2005.

[31] G Wollstein, LA Paunescu, TH Ko, JG Fujimoto, A Kowalevicz, I Hartl, S Beaton, H Ishikawa, C Mattox, O Singh, J Duker, W Drexler, JS Schuman, "Ultrahigh-Resolution Optical Coherence Tomography in Glaucoma," *Ophthalmology*, vol. 112, no. 2, pp. 229-237, 2005.

[32] W Drexler, "Cellular and Functional Optical Coherence Tomography of the Human Retina – The Cogan Lecture," *Invest. Ophthalmol. Vis. Sci.*, vol. 48, no. 12, pp. 5340-5351, 2007.

[33] AG Podoleanu, JA Rogers, DA Jackson, "Three dimensional OCT images from retina and skin," *Opt. Express*, vol. 7, no. 9, pp. 292-298, 2000.

[34] M Wojtkowski, V Srinivasan, JG Fujimoto, T Ko, JS Schuman, A Kowalczyk, JS Duker, "Three-dimensional Retinal Imaging with High-Speed Ultrahigh-Resolution Optical Coherence Tomography," *Ophthalmology*, vol. 112, no. 10, pp. 1734-1746, 2005.

[35] VJ Srinivasan, DC Adler, Y Chen, I Gorczynska, R Huber, JS Duker, JS Schuman, JG Fujimoto, "Ultrahigh-Speed Optical Coherence Tomography for Three-Dimensional and En Face Imaging of the Retina and Optic Nerve Head," *Invest. Ophthalmol. Vis. Sci.*, vol. 49, no. 11, pp. 5103-5110, 2008.

[36] H Yabushita, BE Bouma, SL Houser, HT Aretz, I-K Jang, KH Schlendorf, CR Kauffman, M Shishkov, D-H Kang, EF Halpern, GJ Tearney, "Characterization of Human Atherosclerosis by Optical Coherence Tomography," *Circulation*, vol. 106, pp. 1640-1645, 2002.

[37] GJ Tearney, H Yabushita, SL Houser, HT Aretz, I-K Jang, KH Schlendorf, CR Kauffman, M Shishkov, EF Halpern, BE Bouma, "Quantification of Macrophage Content in Atherosclerotic Plaques by Optical Coherence Tomography," *Circulation*, vol. 107, pp. 113-119, 2003.

[38] B Scheller, U Speck, B Romeike, A Schmitt, M Sovak, M Bohm, H-P Stoll, "Contrast media as carriers for local drug delivery," *Eur. Heart J.*, vol. 24, pp. 1462-1467, 2003.

[39] M Zimarino, F Prati, E Stabile, J Pizzicannella, T Fouad, A Filippini, R Rabozzi, O Trubiani, G Pizzicannella, R De Caterina, "Optical coherence tomography accurately identifies intermediate atherosclerotic lesions – An in vivo evaluation in the rabbit carotid artery," *Atherosclerosis*, vol. 193, pp. 94-101, 2007.

[40] A Tanaka, T Imanishi, H Kitabata, T Hubo, S Takarada, T Tanimoto, A Kuroi, H Tsujioka, H Ikejima, S Ueno, H Kataiwa, K Okouchi, M Kashiwaghi, H Matsumoto, K Takemoto, N Nakamura, K Hirata, M Mizukoshi, T Akasaka, "Morphology of Exertion-Triggered Plaque Rupture in Patients With Acute Coronary Syndrome – An Optical Coherence Tomography Study," *Circulation*, vol. 111, pp. 2368-2373, 2008.

[41] S Takarada, T Imanishi, T Kubo, T Tanimoto, H Kitabata, N Nakamura, A Tanaka, M Mizukoshi, T Akasaka, "Effect of statin therapy on coronary fibrous-cap thickness in patients with acute coronary syndrome: Assessment by optical coherence tomography study," *Atherosclerosis*, vol. 202, pp. 491-497, 2009.

[42] D Matsumoto, J Shite, T Shinke, H Otake, Y Tanino, D Ogasawara, T Sawada, OL Paredes, K Hirata, M Yokoyama, "Neointimal coverage of sirolimus-eluting stents at 6-month follow-up: evaluated by optical coherence tomography," *Eur. Heart J.*, vol. 28, pp. 961-967, 2007.

[43] GJ Czarnota, MC Kolios, J Abraham, M Portnoy, FP Ottensmeyer, JW Hunt, MD Sherar, "Ultrasound imaging of apoptosis: high-resolution non-invasive monitoring of

programmed cell death in vitro, in situ and in vivo," *Brit. J. Cancer*, vol. 81, no. 3, pp. 520-527, 1999.

[44] JFR Kerr, AH Wyllie, AR Currie, "Apoptosis: A Basic Biological Phenomenon with Wide-ranging Implications in Tissue Kinetics," *Brit. J. Cancer*, vol. 26, no. 4, pp. 239-257, 1972.

[45] JGH Joosten, JL McCarthy, "Dynamic and Static Light Scattering by Aqueous Polyacrylamide Gels," *Macromolecules*, vol. 24, pp. 6690-6699, 1991.

[46] FJ van der Meer, DJ Faber, MC Aalders, AA Poot, I Vermes, TG van Leeuwen, "Apoptosis- and necrosis-induced changes in light attenuation measured by optical coherence tomography," *Laser Med. Sci.*, vol. 25, no. 2, pp. 259-267, 2010.

[47] SH Yun, C Boudoux, GJ Tearney, BE Bouma, "High-speed wavelength-swept semiconductor laser with a polygon-scanner-based wavelength filter," *Opt. Lett.*, vol. 28, no. 20, pp.1981-1983, 2003.

[48] A Mariampillai, BA Standish, EH Moriyama, M Khurana, NR Munce, MKK Leung, J Jiang, A Cable, BC Wilson, IA Vitkin, VXD Yang, "Speckle variance detection of microvasculature using swept-source optical coherence tomography," *Opt. Lett.*, vol. 33, no. 13, pp. 1530-1532, 2008.

[49] A Mariampillai. Development of a High Resolution Microvascular Imaging Toolkit for Optical Coherence Tomography. Ph.D. Thesis. University of Toronto: Canada. 2010.

[50] RK Jain, "Transport of Molecules in the Tumor Interstitium: A Review," *Cancer Res.*, vol. 47, pp. 3039-3051, 1987.

[51] Y Yamamoto, "Fundamentals of Noise processes," *Stanford University*, EEAP248 lecture notes, Chapter 1, 2011.